

RUPRECHT-KARLS-UNIVERSITÄT HEIDELBERG



Guillaume Leibenguth

---

Measurement of the  $W$  boson mass  
with the ALEPH detector

Dissertation

HD-KIP-02-01

KIRCHHOFF-INSTITUT FÜR PHYSIK

---



Dissertation  
submitted to the  
Combined Faculties for Natural Sciences and Mathematics  
of the Ruperto-Carola-University of  
Heidelberg, Germany,  
for the degree of  
Doctor of Natural Sciences

presented by

E.U Diplom-Physiker: Guillaume Leibenguth  
born in: Schiltigheim

Oral examination: 13th February 2002



Measurement of  
the W boson mass  
with the ALEPH  
detector

Referees: Prof. Dr. Eike-Erik Kluge  
Prof. Dr. Otto Nachtmann



## Bestimmung der Masse des W Bosons mit dem ALEPH Detektor

Die Masse des  $W$  Bosons wurde mit Zerfällen in die Kanäle  $e\nu q\bar{q}$  und  $\mu\nu q\bar{q}$  extrahiert. Ereignisse der Datenahmeperiode 1998-2000, entsprechend einer integrierten Luminosität von etwa  $650 \text{ pb}^{-1}$ , wurden mit dem ALEPH Detektor aufgezeichnet. Eine kinematische Anpassung, die die Viererimpuls-Erhaltung benutzt, verbessert die Massenrekonstruktion. Die Masse des  $W$  Bosons ist mit Hilfe der Umgewichtungsmethode gemessen. Statistische und systematische Unsicherheiten sind nahezu gleich groß, deswegen sind letztere besonders detailliert untersucht. Das vorliegende Resultat geht in den Weltmittelwert der  $W$  Boson Masse ein, der in einer elektroschwachen Anpassung benutzt wird, um eine obere Grenze für die Masse des Higgs Bosons abzuleiten.

## Measurement of the W boson mass with the ALEPH detector

The  $W$  boson mass has been extracted using  $W$ -pairs decaying into  $e\nu q\bar{q}$  and  $\mu\nu q\bar{q}$  final states. The events were selected from the data collected with the ALEPH detector during the years 1998, 1999 and 2000, corresponding to a total integrated luminosity of about  $650 \text{ pb}^{-1}$ . A kinematic fit imposing four-momentum conservation is then applied to improve the invariant mass resolution. The  $W$  boson mass is obtained from the invariant mass spectrum by a Monte Carlo reweighting method. Since the statistical and systematical uncertainties are at the same level, the latter are investigated in great detail. The presented  $W$  boson mass is then included in a preliminary world average which is used to extract a upper limit on the Higgs boson mass.

## Mesure de la masse du boson W avec le détecteur ALEPH

Les paires de boson  $W$  décroissantes en  $e\nu q\bar{q}$  ou  $\mu\nu q\bar{q}$  sont utilisées pour mesurer la masse du boson  $W$ . Les évènements semi-leptonique sélectionnés proviennent de données prises à l'aide du détecteur ALEPH entre 1998 et 2000. Un ajustement cinématique appliquant la conservation de l'impulsion améliore la résolution de la masse invariante. La masse du boson  $W$  est extraite de la masse invariante par la méthode de repondération. Comme l'incertitude statistique de la masse est à peu près égale à l'incertitude systématique, une étude poussée de ces dernières est présentée. Le résultat obtenu est combiné avec d'autres mesures de la masse du boson  $W$ , la combinaison entrant dans l'ajustement electro-faible servant à extraire une limite supérieure de la masse du boson de Higgs.



# Contents

<b>1</b>	<b>Introduction</b>	<b>3</b>
1.1	History of the Weak Interaction . . . . .	3
1.2	The LEP Program and the $W$ Mass . . . . .	3
1.3	Outline of the Thesis . . . . .	4
<b>2</b>	<b>Theoretical Background</b>	<b>5</b>
2.1	Gauge Symmetries . . . . .	5
2.1.1	U(1) Local Gauge Invariance and Quantum Electrodynamics . . . . .	5
2.1.2	SU(2) and the Weak Interaction . . . . .	6
2.1.3	Electroweak Interaction . . . . .	7
2.1.4	Spontaneous Symmetry Breaking . . . . .	8
2.2	General Properties of the $W$ Boson . . . . .	10
2.2.1	$W$ Pair Production and $W$ Decay . . . . .	10
2.3	$W$ Pair Cross Section . . . . .	11
2.3.1	The On-shell Model . . . . .	12
2.3.2	$W$ Width . . . . .	13
2.3.3	The Off-shell Model . . . . .	14
<b>3</b>	<b>Description of the Apparatus</b>	<b>17</b>
3.1	The LEP Collider . . . . .	17
3.1.1	Luminosity . . . . .	18
3.1.2	The Measurement of the LEP Energy . . . . .	19
3.2	ALEPH - Apparatus for LEP PHysics . . . . .	20
3.2.1	The Vertex Detector . . . . .	20
3.2.2	Inner Tracking Chamber . . . . .	21
3.2.3	Time Projection Chamber . . . . .	22
3.2.4	Electromagnetic Calorimeter . . . . .	23
3.2.5	Super-conducting Magnet . . . . .	24
3.2.6	Hadron Calorimeter . . . . .	24
3.2.7	Muon Detection Chambers . . . . .	25
3.2.8	Luminosity Monitors . . . . .	25
3.3	Trigger System . . . . .	26
3.3.1	Detector Components used in the Trigger . . . . .	26
3.3.2	Creation of Physics Trigger . . . . .	26
3.4	Data Acquisition . . . . .	27
3.4.1	Event Reconstruction . . . . .	28

<b>4</b>	<b>Monte Carlo Simulation</b>	<b>31</b>
4.1	Generators . . . . .	31
4.1.1	<i>WW</i> Monte Carlo Simulation . . . . .	31
4.1.2	Background . . . . .	33
4.2	External Packages . . . . .	34
4.2.1	Fragmentation . . . . .	34
4.2.2	Final State Radiation . . . . .	35
4.3	Detector Simulation . . . . .	36
4.4	Summary . . . . .	36
<b>5</b>	<b>Event Selection</b>	<b>37</b>
5.1	Preselection . . . . .	37
5.2	Lepton Selection . . . . .	38
5.2.1	Electron . . . . .	38
5.2.2	Muon . . . . .	39
5.2.3	Corrections . . . . .	39
5.3	Jet Reconstruction . . . . .	39
5.3.1	Algorithms . . . . .	39
5.3.2	Jet Energy Corrections . . . . .	40
5.4	Neural Network Selection . . . . .	41
5.5	Summary . . . . .	42
<b>6</b>	<b>Determination of the <i>W</i> Mass</b>	<b>47</b>
6.1	Concept of Constrained Fit . . . . .	47
6.1.1	Momentum Calibration for Detector Acceptance . . . . .	48
6.1.2	Minimisation of the $\chi^2$ . . . . .	48
6.1.3	Stability and Performance of the Kinematic Fit . . . . .	49
6.2	Mass Extraction . . . . .	52
6.2.1	Reweighting Method and Maximum Likelihood Fit . . . . .	53
6.2.2	Multi-dimensional Reweighting . . . . .	54
6.2.3	Choice of Estimators . . . . .	55
6.2.4	Choice of the binning . . . . .	55
6.3	Cross Check of the Method . . . . .	57
6.3.1	Expected Statistical Errors . . . . .	57
6.3.2	Linear Behaviour . . . . .	59
6.4	Data Results . . . . .	59
6.4.1	Mass Window . . . . .	59
<b>7</b>	<b>Systematic Error</b>	<b>63</b>
7.1	Detector related Errors . . . . .	63
7.1.1	Detector Alignment . . . . .	63
7.1.2	Lepton Angle . . . . .	64
7.1.3	Radiation in the Final State . . . . .	64
7.1.4	Jet Corrections . . . . .	65
7.1.5	Jet Angular Bias . . . . .	65
7.1.6	Jet Angular Resolution . . . . .	66
7.1.7	Calorimeter Calibration . . . . .	66
7.1.8	Summary . . . . .	67

---

7.2	Background . . . . .	68
7.3	Beam energy uncertainty . . . . .	68
7.4	Method Related Uncertainty . . . . .	68
7.5	Theoretical Uncertainties . . . . .	70
7.5.1	Fragmentation Process . . . . .	70
7.5.2	Radiative Corrections . . . . .	70
7.6	Summary . . . . .	71
<b>8</b>	<b>Discussion of the Results</b>	<b>73</b>
8.1	W Mass Measurement in the Semi-leptonic Channel . . . . .	73
8.2	Combination of the W Mass Measurement . . . . .	74
8.2.1	In ALEPH . . . . .	74
8.2.2	Combination Of All LEP W Mass Measurements . . . . .	75
8.2.3	World Average of Direct Measurement . . . . .	76
8.3	Relevance of Precision in $W$ Mass Determination on the Standard Model . .	76
<b>A</b>	<b>Constrained Fit</b>	<b>81</b>
A.1	Introduction . . . . .	81
A.2	Without the Unmeasured Parameters . . . . .	83
A.3	General Case . . . . .	83
<b>B</b>	<b>Monte Carlo Statistics</b>	<b>85</b>
	<b>Acknowledgement</b>	<b>93</b>

# List of Figures

2.1	Mexican hat: the Higgs potential $V(\Phi)$ . . . . .	9
2.2	CC03 diagrams . . . . .	11
2.3	Cross section $WW$ as function of the energy of the centre-of-mass . . . . .	12
2.4	The cross-section for $e^+e^- \rightarrow W^+W^-$ in various approximations: (i) Born (on-shell) cross-section, (ii) Born (off-shell) cross-section, (iii) with first order Coulomb correction and (iv) with initial state radiation . . . . .	15
3.1	Schematic view of the LEP ring with the four experiments and the injector chain	17
3.2	The luminosity in 2000 . . . . .	18
3.3	ALEPH-Detector . . . . .	20
3.4	The VDET . . . . .	21
3.5	Overall view of the ITC . . . . .	21
3.6	Overall view of the TPC . . . . .	22
3.7	Overall view of the ECAL . . . . .	23
3.8	Overall view of the HCAL . . . . .	25
4.1	Schematic view of the hadronisation . . . . .	34
4.2	Gluon splitting . . . . .	35
5.1	The jet correction . . . . .	41
5.2	Distribution of the 3 input variables of the neural network (in the $e\nu q\bar{q}$ ) . . .	43
5.3	Distribution of the 3 input variables of the neural network ( $\mu\nu q\bar{q}$ channel) . .	44
5.4	$e\nu q\bar{q}$ and $\mu\nu q\bar{q}$ Neural Network output . . . . .	46
6.1	Effect of the kinematic fit on the measured di-jet mass . . . . .	49
6.2	Two-dimensional mass distribution . . . . .	50
6.3	Correlation between the 1C hadronic and leptonic mass distribution . . . . .	51
6.4	$\chi^2$ Probability of the constrained fit . . . . .	52
6.5	Adaptive binning . . . . .	56
6.6	Pull distribution and expected statistical error . . . . .	58
6.7	Calibration Curve . . . . .	60
6.8	Invariant Mass Distribution . . . . .	61
6.9	Stability of the data fit results . . . . .	62
7.1	Comparison of the different jet correction factors . . . . .	65
7.2	Jet angular bias . . . . .	66
7.3	Dependence of the $W$ mass as a function of the centre-of-mass energy . . . . .	69
8.1	The $W$ mass measured at LEP II . . . . .	75
8.2	The preliminary world average $W$ mass . . . . .	77

---

8.3	Preliminary comparison between the indirect and direct measurement of the top mass and the W mass . . . . .	78
8.4	The Blue band plot . . . . .	79



# Chapter 1

## Introduction

### 1.1 History of the Weak Interaction

In nuclear  $\beta$  decays, one observes that the energy and momentum of the measurable decay products is not conserved. This fact caused Pauli to postulate in 1930 the existence of a new particle, the neutrino, which carried off the missing energy and momentum. The weak interaction was introduced by Fermi (1934) [1] to provide a model for  $\beta$  decay, in analogy to the electromagnetic process of virtual emission and absorption of a single photon. The coupling constants for muon ( $\mu$ ) decay and muon-capture were found to be of the same order of magnitude as for beta-decay. Subsequently a universal Fermi interaction was hypothesised in 1948, which suggested that the couplings in each of those three processes should be of the same type and strength [2]. In 1957, a number of experiments established the parity non-conservation in weak decays [3] showing the vector and axial-vector (V-A) coupling of the weak interaction [4]. This motivated the need to confirm the beta decay of the pion, subsequently established in 1958 [5]. The unification of the electromagnetic and weak interactions was achieved by Weinberg [6], Salam [7] and Glashow [8]. The Eightfold way [9], the quark idea [10], the deep inelastic scattering of electrons on protons [11] and asymptotic freedom helped to construct the theory of strong interaction between quarks (Quantum Chromodynamics, QCD) [12]). The combination of the electroweak theory and QCD forms the Standard Model. The last force, gravity, is not included in the Standard Model. The interactions in the Standard Model are mediated by bosons. The photon ( $\gamma$ ) is the mediator of the electromagnetic interaction; the two charged  $W^+$ ,  $W^-$  bosons and the neutral  $Z^0$  boson are the mediators of the weak interaction. The eight gluons are the mediators of the strong interaction. The fermions are grouped in three families and constitute matter. One of the Standard Model's biggest successes was the observation of the  $W^\pm$  by the UA1 [13] and UA2 [14] collaborations in 1983. But the Standard Model leaves many questions unanswered. One important problem is that the Higgs mechanism, which is supposed to give mass to all leptons, quarks and weak bosons, has not been verified. The Large Electron-Positron Collider (LEP) was especially built to study the electroweak interaction. With a purely leptonic initial state, many of the parameters of the Standard Model have been tested with great precision.

### 1.2 The LEP Program and the $W$ Mass

During the first phase of LEP (called LEP I) between 1989 and 1995, the LEP machine was operated at beam energies around half the  $Z^0$  mass.  $Z^0$  events are classified in two

groups, hadronic and leptonic decays, where the  $Z^0$  decays into a quark pair or a lepton pair respectively. During the second phase of LEP (called LEP II) between 1996 and 2000, the LEP machine was operated at centre-of-mass (CM) energies at and above the  $W$ -pair threshold, which allows a precise determination of the  $W$  mass. The search for a direct signature of the Higgs boson required the CM energies to be pushed to the highest possible limits.

The  $Z^0$  mass was measured with great precision at LEP I by measuring cross sections around the  $Z^0$  peak. Using the LEP I and SLD data, the top mass ( $M_{top}$ ), the Higgs mass ( $M_h$ ) and the  $W$  mass were all indirectly measured or constrained. The error obtained on the  $W$  mass is  $33 \text{ MeV}/c^2$ . The top mass is directly measured from top production at the Tevatron in perfect agreement with the indirect measurement. Therefore, a direct measurement of the  $W$  mass, when compared with the indirect measurement, can be seen as a further test of the Standard Model at the level of loop corrections. To make such a test meaningful, the error on the direct measurement should be comparable to that of the indirect measurement. Finally, the new data on the  $W$  mass can be used as independent new data, and the Higgs mass can be further constrained.

Many methods have been developed to measure the  $W$  mass experimentally. One method involves the measurement of the  $W$ -pair production cross section which rises rapidly near threshold (see Section 2.3). However, the delivered luminosity is too small to reach the goal outlined in the previous paragraph. Another method consists of measuring the lepton end-point energy. The statistical sensitivity of the method is too small [18]. Another method is the direct reconstruction of the  $W$  decay products which is used here. Each  $W$  boson can decay either hadronically or leptonically. The decay channel studied in this thesis is the semi-leptonic one, where one  $W$  decays in hadrons and the other one in leptons.

### 1.3 Outline of the Thesis

This thesis is organised as follows. Chapter 2 is dedicated to the principle properties of the  $W$  bosons, which are needed for the analysis. In chapter 3, the experimental set-up is described. Since the expected error of the  $W$  mass for LEP II is  $50 \text{ MeV}/c^2$ , the precision of the Monte Carlo simulation becomes extremely important. Chapter 4 gives a short introduction of all Monte Carlo simulations used in this thesis. The selection of events is studied in chapter 5. Chapter 6 gives an introduction of the direct reconstruction. Chapter 7 deals with all the systematic uncertainties of the measurement. Finally, the result is combined with previous ALEPH measurements [19] and with all measurements of the  $W$  boson mass. An upper limit on the Higgs mass is derived from this measurement.

# Chapter 2

## Theoretical Background

“One of the most profound insights in theoretical physics is that the interactions are dictated by symmetry principles” [20]. The connection between symmetries and conservation laws is best discussed in the framework of a Lagrangian field theory. In the first section of this chapter, this concept will be used to form the electroweak interaction theory. The Higgs mechanism, which gives mass to the particles, will be introduced. The second section of the chapter is dedicated to the general properties of the  $W$  bosons and the third section introduces the cross section of the  $e^+e^- \rightarrow W^+W^-$  process.

### 2.1 Gauge Symmetries

Invariance under translation, time displacement and rotation leads to the conservation of momentum, energy and angular momentum respectively.

The Lagrangian of the Dirac equation:

$$(i\gamma^\mu\partial_\mu - m)\psi = 0, \quad (2.1)$$

which is satisfied by free fermions with mass  $m$ , is:

$$\mathcal{L} = i\bar{\psi}\gamma^\mu\partial_\mu\psi - m\bar{\psi}\psi. \quad (2.2)$$

If the fermion fields  $\psi$  undergo a transformation  $\psi \rightarrow \psi'(x) = e^{i\alpha}\psi(x)$ , the Lagrangian is invariant under this phase transformation. This invariance can easily be verified by noting:

$$\partial_\mu\psi \rightarrow e^{i\alpha}\partial_\mu\psi(x), \quad (2.3)$$

$$\bar{\psi} \rightarrow e^{-i\alpha}\bar{\psi}. \quad (2.4)$$

The phase  $\alpha$  is a real constant, which can be chosen arbitrarily. Therefore, the value is specified for all space-time. This type of gauge invariance is called *global*. A more general case would be if  $\alpha$  could differ from point to point in space-time,  $\alpha = \alpha(x)$ .

#### 2.1.1 U(1) Local Gauge Invariance and Quantum Electrodynamics

The equation (2.3) could be generalised to the transformation

$$\psi(x) \rightarrow \psi'(x) = e^{i\alpha(x)}\psi(x), \quad (2.5)$$

where  $\alpha(x)$  depends on space and time in a completely arbitrary way. This is called a *local* (U(1)) gauge invariance. The free Dirac Lagrangian

$$\mathcal{L} = i\bar{\psi}\gamma^\mu\partial_\mu\psi - m\bar{\psi}\psi, \quad (2.6)$$

is not invariant under this transformation (the derivative of  $\psi$  does not follow equation 2.5). To impose the invariance of the Lagrangian under local phase transformation, it is then necessary to introduce a vector field (also called a gauge field)  $A_\mu$  with transformation properties such that the change induced by  $\partial_\mu$  is cancelled. This could be done if  $\partial_\mu$  is replaced by the *covariant derivative*  $D_\mu$ :

$$\partial_\mu \rightarrow D_\mu = \partial_\mu - ieA_\mu, \quad (2.7)$$

where  $A_\mu$  transforms as

$$A_\mu \rightarrow A_\mu + \frac{1}{e}\partial_\mu\alpha. \quad (2.8)$$

Hence, the requirement of a local gauge theory leads to the fact that the Dirac particle (charge -e) is no longer free. Invariance of the Lagrangian (2.6) is obtained by replacing  $\partial_\mu$  by  $D_\mu$ :

$$\mathcal{L} = i\bar{\psi}\gamma^\mu D_\mu\psi - m\bar{\psi}\psi = \bar{\psi}(i\gamma^\mu\partial_\mu - m)\psi + e\bar{\psi}\gamma^\mu\psi A_\mu. \quad (2.9)$$

In order to give a physical meaning to this new field, the kinetic properties of this field should be added to the Lagrangian. In addition, this kinetic energy term must be invariant under equation (2.8), so this term is the gauge invariant field strength tensor:

$$F_{\mu\nu} = \partial_\mu A_\nu - \partial_\nu A_\mu. \quad (2.10)$$

This implies that the corresponding gauge particle, the photon, must be massless. We are led to the Lagrangian of QED:

$$\mathcal{L} = \bar{\psi}(i\gamma^\mu\partial_\mu - m)\psi + e\bar{\psi}\gamma^\mu\psi A_\mu - \frac{1}{4}F_{\mu\nu}F^{\mu\nu}. \quad (2.11)$$

### 2.1.2 SU(2) and the Weak Interaction

In the previous section only the QED Lagrangian was considered. The photon was introduced as a gauge particle. However, we would like to apply the gauge theory to the *weak process* as a generalisation and we want to keep the gauge invariance. The SU(2) group is chosen to describe the weak interaction. There is no real reason to choose this group based on fundamental principles, but this model or group has been extremely successful in describing the data. The generalisation of local gauge invariance to a group SU(N) is:

$$\psi(x) \rightarrow \psi'(x) = e^{i\sum_{j=1}^N\theta_j(x)T_j}\psi, \quad (2.12)$$

for N greater than one, where the  $\theta_j(x)$  are arbitrary real functions and  $T_j$  are the generators of SU(N). Two fundamental notions are extracted from this generalisation:

- The group has now N dimensions,
- The SU(N) groups are not Abelian <sup>1</sup> groups.

---

<sup>1</sup>The definition of an Abelian group is that the members commute with respect to multiplication.

The fermions exist in nature in two different configurations, concerning the spin and velocity vectors. These two vectors can be parallel or anti-parallel and are called left-handed (anti-parallel) or right-handed (parallel). We know, from past experiments, that the weak interaction treats fermions differently according to the chirality<sup>2</sup>. The helicity is defined as the projection of the spin onto the direction of motion. The behaviour of the weak force is not the same for right- and left-handed particles, i.e the left-handed fermions are doublets of SU(2) and right-handed fermions are singlets. However, the electromagnetic force affects both right-handed and left-handed particles. We aim then to build a group composed of U(1) and SU(2). This theory is the so-called electroweak interaction.

### 2.1.3 Electroweak Interaction

In order to achieve this “unification”, the transformation of the field (2.5) of U(1) is rewritten as:

$$\psi \rightarrow e^{i\beta(x)Y} \psi, \quad (2.13)$$

where  $Y$  is the generator (also named the weak hypercharge) of the group. This transformation is valid for left- and right-handed fermions. For SU(2)×U(1), it is natural to apply the following separation:

$$\psi_L \rightarrow e^{i\alpha^j(x)\tau_j + i\beta(x)Y} \psi_L, \quad (2.14)$$

$$\psi_R \rightarrow e^{i\beta(x)Y} \psi_R, \quad (2.15)$$

where the index L (R) stands for left-handedness (right-) and  $\tau_j$  are the three generators of SU(2) (also named weak isopin). Furthermore, one would like to introduce the charge operator  $Q$ , since the conservation of charge is a fact in nature. One needs to find a relation between the weak operator (invariant under this gauge) and the electric charge to include the conservation of charge in our description. This relation, known as the Gell-Mann-Nishijima [20] relation, is relatively simple:

$$Q = T_3 + \frac{Y}{2}, \quad (2.16)$$

where  $T_3$  is the third component of the weak isopin. Using this relation, all weak quantum numbers (Table 2.1) are determined.

To generalise the QED Lagrangian (2.11), we are forced to introduce four gauge vector fields, three vectors  $W_\mu^j$  with  $j=1,2,3$  associated with SU(2) and one vector  $B_\mu$  with U(1). The covariant derivative is then:

$$\partial_\mu \rightarrow D_\mu = \partial_\mu + ig\tau_j W_\mu^j + ig' \frac{Y}{2} B_\mu, \quad (2.17)$$

where  $g$  and  $g'$  are the couplings between the fermions and the SU(2)×U(1) vector fields. The electroweak Lagrangian is then:

$$\begin{aligned} \mathcal{L} = & \bar{\psi}_L \gamma^\mu \left( i\partial_\mu - g\tau_j W_\mu^j - g' \frac{Y}{2} B_\mu \right) \psi_L + \bar{\psi}_R \gamma^\mu \left( i\partial_\mu - g' \frac{Y}{2} B_\mu \right) \psi_R \\ & - \frac{1}{4} W_{\mu\nu}^j W_j^{\mu\nu} - \frac{1}{4} B_{\mu\nu} B^{\mu\nu} \end{aligned} \quad (2.18)$$

---

<sup>2</sup>The chirality is the symmetry which belongs to the description of left (right) handed fermions.

First generation	Second generation	Third generation	Isospin $\{3^{rd}\}$	Y	Q
$\begin{pmatrix} \nu_e \\ e \end{pmatrix}_L$	$\begin{pmatrix} \nu_\mu \\ \mu \end{pmatrix}_L$	$\begin{pmatrix} \nu_\tau \\ \tau \end{pmatrix}_L$	$\frac{1}{2} \begin{Bmatrix} \frac{1}{2} \\ -\frac{1}{2} \end{Bmatrix}$	-1	$\begin{Bmatrix} 0 \\ -1 \end{Bmatrix}$
$e_R$	$\mu_R$	$\tau_R$	0	-2	-1
$\begin{pmatrix} u \\ d \end{pmatrix}_L$	$\begin{pmatrix} c \\ s \end{pmatrix}_L$	$\begin{pmatrix} t \\ b \end{pmatrix}_L$	$\frac{1}{2} \begin{Bmatrix} \frac{1}{2} \\ -\frac{1}{2} \end{Bmatrix}$	$\frac{1}{3}$	$\begin{Bmatrix} \frac{2}{3} \\ -\frac{1}{3} \end{Bmatrix}$
$u_R$	$c_R$	$t_R$	0	$\frac{4}{3}$	$\frac{2}{3}$
$d_R$	$s_R$	$b_R$	0	$\frac{4}{3}$	$-\frac{1}{3}$

Table 2.1: *Electroweak quantum numbers of all fermions.*

where  $B_{\mu\nu}$  and  $W_{\mu\nu}$  are the field strength tensors. This theory should reproduce all the current knowledge of the weak and electromagnetic interactions. The gauge particles do not correspond to the particles which “transmit” the weak interaction, the  $Z^0$  and  $W^\pm$  gauge bosons. The observed bosons can be related to W and B by:

$$A_\mu = B_\mu \cos \theta_W + W_\mu^3 \sin \theta_W, \quad (2.19)$$

$$Z_\mu = -B_\mu \sin \theta_W + W_\mu^3 \cos \theta_W, \quad (2.20)$$

$$W_\mu^\pm = \frac{1}{\sqrt{2}} (W_\mu^1 \mp iW_\mu^2), \quad (2.21)$$

where  $\theta_W$  is the weak mixing angle (also called Weinberg angle). At this level of the theory, the gauge bosons  $A_\mu$ ,  $Z_\mu$ ,  $W_\mu^\pm$  which are introduced by this rotation are still massless.

#### 2.1.4 Spontaneous Symmetry Breaking

The  $W$  and  $Z^0$  bosons have masses close to  $80 \text{ GeV}/c^2$  and  $90 \text{ GeV}/c^2$  respectively. However, this means that the Lagrangian is no longer invariant under gauge transformations, as massive particles break gauge symmetry. A way to solve this problem is given by the Higgs mechanism. This mechanism consists of the introduction of a new doublet of complex scalar (Higgs) fields with a weak hypercharge  $Y=1$  defined as:

$$\Phi = \begin{pmatrix} \phi^+ \\ \phi^0 \end{pmatrix}. \quad (2.22)$$

The associated Lagrangian of this field is the electroweak Lagrangian (equation (2.18)) where we add the Higgs field potential:

$$\mathcal{L}_H = (D_\mu \Phi)^\dagger (D_\mu \Phi) - V(\Phi), \quad (2.23)$$

where the potential  $V(\Phi)$  is:

$$V(\Phi) = \mu^2 \Phi^\dagger \Phi + \lambda (\Phi^\dagger \Phi)^2. \quad (2.24)$$

The  $\lambda$  parameter must be larger than 0, to ensure no divergence. Figure 2.1 shows two cases of the Higgs potential, for  $\mu^2$  positive and negative. Considering the case  $\mu^2 < 0$ , with a

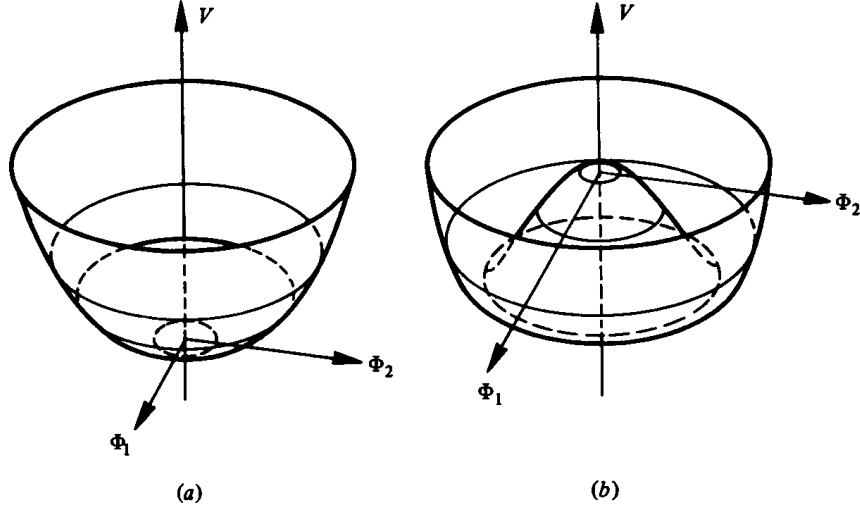


Figure 2.1: *The Higgs potential  $V(\Phi)$  with:*  
a) *unique ground state corresponding to  $\mu^2 > 0$  and*  
b) *degenerate ground state corresponding to  $\mu^2 < 0$  (Mexican hat).*

degenerate ground state, the minimum of the potential is obtained when:

$$\Phi^\dagger \Phi = \frac{-\mu^2}{2\lambda} = \frac{v^2}{2}. \quad (2.25)$$

Using perturbative theory, it is possible to expand  $\Phi$  around its minimum:

$$\langle \Phi \rangle = \langle 0 | \Phi | 0 \rangle = \begin{pmatrix} 0 \\ v/\sqrt{2} \end{pmatrix}. \quad (2.26)$$

Any choice of a vacuum expectation value,  $\phi(x)$ , of  $\Phi$ , will break the  $SU(2) \times U(1)$  symmetry. However, the photon is massless, so one does not want to break the  $U(1)$  symmetry. Choosing a neutral field  $\phi^0$  prevents  $U(1)$  to be broken. The gauge boson masses are then derived by replacing the vacuum expectation value for  $\phi(x)$  in the kinetic term of the Lagrangian  $\mathcal{L}_H$ :

$$\begin{aligned} (D_\mu \Phi)^\dagger (D^\mu \Phi) &= \left| \left( ig\tau_j W_\mu^j + i\frac{g'}{2} Y B_\mu \right) \phi \right|^2 \\ &= \frac{1}{8} \left| \begin{pmatrix} gW_\mu^3 + g'B_\mu & g(W_\mu^1 - iW_\mu^2) \\ g(W_\mu^1 + iW_\mu^2) & -gW_\mu^3 + g'B_\mu \end{pmatrix} \begin{pmatrix} 0 \\ v \end{pmatrix} \right|^2 \\ &= \frac{1}{8} v^2 g^2 \left[ (W_\mu^1)^2 + (W_\mu^2)^2 \right] + \frac{1}{8} v^2 (g'B_\mu - gW_\mu^3) (g'B_\mu - gW_\mu^3). \end{aligned} \quad (2.27)$$

Noting that  $W^+W^- = 1/2 \left( (W^1)^2 + (W^2)^2 \right)$  and diagonalising<sup>3</sup> the remaining term, one can extract the following equations, corresponding to the mass of the  $Z^0$  and  $W^\pm$  bosons:

$$M_{Z^0} = \frac{1}{2}v\sqrt{g^2 + (g')^2}, \quad (2.28)$$

and

$$M_W = \frac{1}{2}vg. \quad (2.29)$$

In addition, the ratio of the two boson masses can be written as:

$$\frac{M_W}{M_{Z^0}} = \cos(\theta_W) = \frac{g}{\sqrt{g^2 + (g')^2}}. \quad (2.30)$$

## 2.2 General Properties of the $W$ Boson

The  $W$  mass,  $M_W$ , has been measured at CERN [15] and the Tevatron  $p\bar{p}$  colliders at Fermilab ([16] and [17]). Before LEP II, the ‘world average’ value was [18]:

$$M_W = 80.26 \pm 0.16 \text{ GeV}/c^2. \quad (2.31)$$

The goal of LEP II is to perform a direct measurement of the  $W$  mass with a precision of 30-50 MeV/ $c^2$ . At LEP I, the  $W$  mass was derived from the Fermi Constant,  $G_F$  (or  $G_\mu$ , historically), which is measured in muon decays:

$$G_F = \frac{\alpha (M_Z^2) \pi}{\sqrt{2}M_W^2 (1 - M_W^2/M_Z^2)} \frac{1}{1 - \Delta r} \quad (2.32)$$

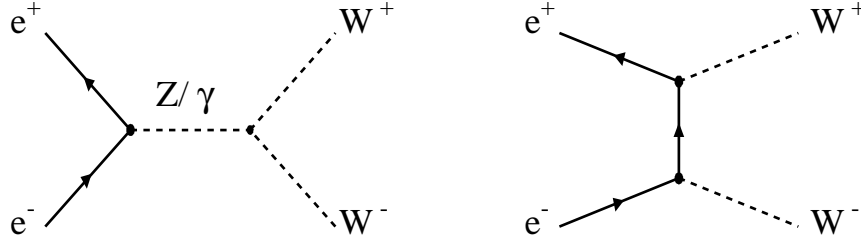
where  $\alpha (M_Z^2)$  is the electromagnetic coupling constant at  $Q^2 = M_Z^2$  and  $\Delta r$  are loop corrections (i.e.  $\Delta r = 0$  in the lowest-order) which depend on  $m_t$  (mass of the top quark) and  $M_H$  (mass of the Higgs boson). At LEP II, the  $W$  mass can be measured directly. Since the  $G_F$ ,  $\alpha$  and  $M_Z$  are measured to high precision [21], this formula can be used to test the Standard Model.

### 2.2.1 $W$ Pair Production and $W$ Decay

The  $W$  bosons at LEP II are primarily produced in pairs. At tree-level, the production of a  $W$  pair is described by the annihilation diagram  $e^+e^-$  through a  $Z^0$  or a  $\gamma$  (s-channel), or through the exchange of a neutrino (t-channel). These s- and t-channel Feynman diagrams are shown in Figure 2.2. These three processes are called the CC03 diagrams (CC for Charged Current). Since the  $W$  boson decays into a fermion and anti-fermion (Table 2.2), the ‘detectable’ final states are composed of four fermions at the ‘parton’ level (Table 2.2) [20]. At LEP II, there are many processes with four final state fermions. In this work, the ones which come from a  $W$  pair will be called **signal** and the rest of the four fermion processes will be called **background** (for example  $e^+e^- \rightarrow e^+e^-e^+e^-$  has 144 Feynman diagrams).

In the purely hadronic process,  $WW \rightarrow q\bar{q}q\bar{q}$ , both  $W$  bosons decay hadronically, there is also the possibility of colour reconnection (colour exchange between decay products of different  $W$  boson) or Bose-Einstein effects between pions from jets of different  $W$  bosons

<sup>3</sup>One of the eigenvalues is zero by construction.

Figure 2.2:  $CC03$  diagrams.

decay	Branching Ratio (in %)
$W \rightarrow e\nu$	$10.54 \pm 0.17$
$W \rightarrow \mu\nu$	$10.54 \pm 0.16$
$W \rightarrow \tau\nu$	$11.09 \pm 0.22$
$W \rightarrow l\nu$	$10.69 \pm 0.09$
$W \rightarrow \text{hadrons}$	$67.92 \pm 0.27$

Table 2.2: LEP [22] measured branching ratios of the  $W$  boson. The first three values do not use the lepton universality assumption. The two last values assume the lepton universality and  $l$  stands for a lepton, either an electron, a muon or a tau.

after the quark fragmentation. In the purely leptonic channel and in the process  $WW \rightarrow q\bar{q}\tau\nu$ , there are multiple neutrinos in the final state. As the neutrino escapes undetected, events with more than one neutrino are not constrained enough for accurate mass reconstruction. Consequently, in this thesis only the semi-leptonic channel, with a muon or an electron (the branching fractions are given in Table 2.3), will be considered.

process	Branching Fraction (in %)
$W^+W^- \rightarrow q\bar{q}q\bar{q}$	46.1
$W^+W^- \rightarrow l\nu(e, \mu, \tau)q\bar{q}$	43.5
$W^+W^- \rightarrow l\nu(e, \mu)q\bar{q}$	29.0
$W^+W^- \rightarrow l\nu l\nu$	10.3

Table 2.3: Decay channel of a  $W$  pair. The branching fractions are obtained using the value of Table 2.2.

## 2.3 $W$ Pair Cross Section

In this section, we describe the theoretical cross section for the process  $e^+e^- \rightarrow W^+W^-$ . The lowest-order cross section determines most of the features of the  $W$  pair production. In addition, we introduce here the on-shell model which neglects the width of the  $W$  boson. We will later introduce the  $W$  width and discuss the off-shell model.

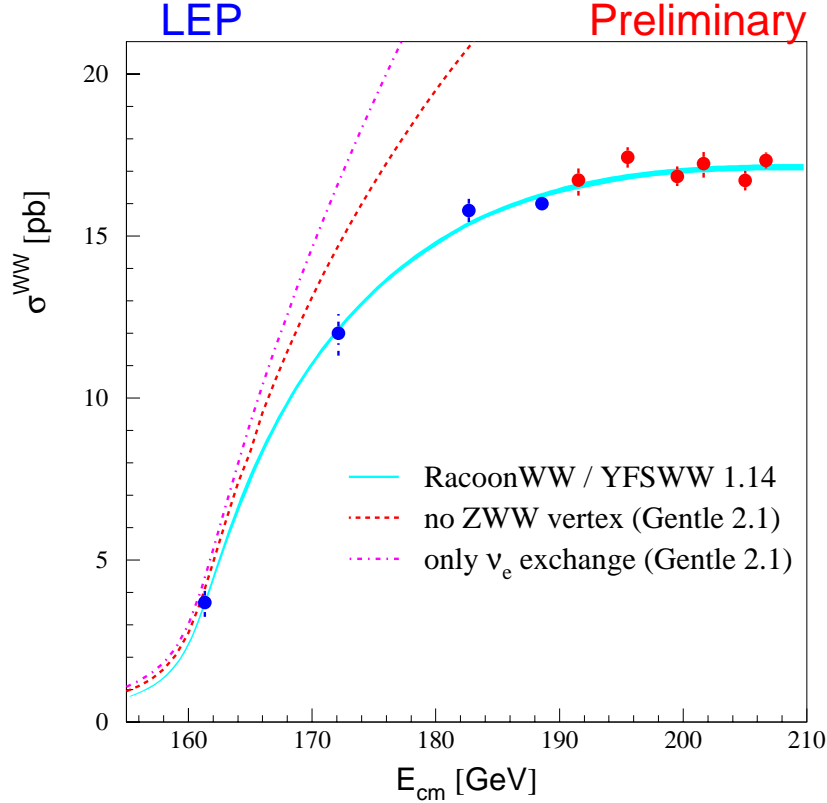


Figure 2.3: Preliminary  $WW$  cross section as function of the CM energy measured by the four LEP experiments [22]. The Monte Carlo simulations *RacoonWW* and *YFSWW* will be described in chapter 4. *GENTLE* [57] is a semi-analytic program.

The total cross section (Figure 2.3) of four fermion processes cannot be split into signal ( $\sigma_s$ ) and background ( $\sigma_b$ ) in a gauge invariant way. For practical reason, however, the following approximation is assumed:

$$\sigma_{tot} = \sigma_s + \sigma_b. \quad (2.33)$$

The  $WW$  contribution can be decomposed in the form

$$\sigma_s = \sigma^0 (1 + \delta_{EW} + \delta_{QCD}), \quad (2.34)$$

where  $\sigma^0$  is the Born contribution,  $\delta_{EW}$  are electroweak corrections (to lowest-order) and  $\delta_{QCD}$  is a QCD correction.

### 2.3.1 The On-shell Model

In this model, the  $W$  boson has no width. The  $WW$  signal cross section is given by [18]:

$$\sigma_{on}^0 \approx \frac{\pi\alpha^2}{s} \frac{1}{\sin^4 \theta_W} \cdot \beta + \mathcal{O}(\beta^3), \quad (2.35)$$

for an unpolarised beam,  $\beta \ll 1$  where  $\beta = \sqrt{1 - 4M_W^2/s}$  is the velocity of the *W* boson and  $\theta_W$  is the Weinberg angle. The  $\beta$  term comes from the *t*-channel. The *s*-channel and the *s* – *t* interference contributions are proportional to  $\beta^3$ . This is a consequence of CP conservation, fermion helicity conservation in the initial state, and the orthogonality of different partial waves [23]. This approximation is only valid up to a few GeV above threshold, (see Figure 2.3). The top curve shows the contribution of the *t*-channel only. One clearly sees that the *s*-channel  $\beta^3$  contribution cannot be neglected for energies well above threshold.

In order to determine the *W* mass with a precision of  $\approx 30$  MeV/ $c^2$ , it is necessary to include electroweak corrections. Two of the most important corrections include:

- Initial State Radiation (ISR): ISR has a large effect on the cross section (change of -20 % at threshold and -6 % at  $\sqrt{s} = 180$  GeV [18]), and determines the effective energy available in the CM frame of reference.
- The Coulomb singularity: Before the decay, the two *W* bosons can exchange a photon. This interaction induces a correlation between the two masses, which modifies the *W* mass distribution. Since this effect is proportional to  $1/\beta$  at the production threshold in the on-shell case, the Coulomb effect would diverge. In reality, because the *W* has a natural width, there exists a cut-off for multiple soft photon exchange between the *W* pair which eliminates the Coulomb divergence.

### 2.3.2 *W* Width

In the on-shell case, the *W* boson is treated as a stable particle, which is an approximation. The width of the *W* boson is one of the most important parameters in the study of *W* pair production. Moreover, the behaviour of the cross section and the branching ratios are affected by this width.

Since the *W* boson has a finite width, the Coulomb singularity is avoided. The *W* width is known theoretically with good precision, but experimentally it is relatively poorly known. The *W* width is dominated by decays into fermion-antifermion pairs (at the lowest-order). The partial width for each decay channel (massless fermions are assumed, i.e  $M_f \ll M_W$ ) is given by:

$$\Gamma_{W \rightarrow f_i f_j}^{Born} = \frac{\alpha}{6} \frac{M_W}{2 \sin^2 \theta_W} \cdot |V_{ij}|^2 N_c^f. \quad (2.36)$$

For leptonic decays, the CKM [20] mixing matrix  $V_{ij}$  is diagonal and the colour factor  $N_c^f$  is one. For hadronic decays, the element of the mixing matrix  $V_{ij}$  is the relevant element of the CKM matrix and the colour factor  $N_c^f$  is three. The total width is obtained by summing over the partial widths, in the Born approximation:

$$\Gamma_W^{Born} = \frac{3\alpha}{2} \frac{M_W}{2 \sin^2 \theta_W}. \quad (2.37)$$

Including QCD and electroweak radiative corrections which can be accounted for by parameterising the lowest-order in terms of  $G_F$  and  $M_W$  instead of  $\alpha$  and  $\theta_W$ , the *W* width is obtained as

$$\Gamma_{W \rightarrow l_i \nu_i} = \frac{G_F M_W^3}{6\sqrt{2}\pi}, \quad (2.38)$$

for a  $W \rightarrow l_i \nu_i$  decay and

$$\Gamma_{W \rightarrow u_i \bar{d}_j} = \frac{G_F M_W^3}{2\sqrt{2}\pi} |V_{ij}|^2 \left( 1 + \frac{\alpha_s (M_W^2)}{\pi} \right), \quad (2.39)$$

for a  $W \rightarrow u_i \bar{d}_j$  decay. The total width is then:

$$\Gamma_W = \frac{3G_F M_W^3}{2\sqrt{2}\pi} \left( 1 + \frac{2\alpha_s (M_W^2)}{3\pi} \right). \quad (2.40)$$

The mass dependence of the width of the  $W$  boson is clear ( $\Gamma_W$  is proportional to the third power of  $M_W$ ). Three possibilities exist for extracting of the  $W$  mass and its relation to the  $W$  width:

- The functional dependence  $\Gamma_W = \Gamma_W(M_W)$  is included as a Standard Model constraint;
- The Standard Model constraint is removed and the width is extracted with the  $W$  mass;
- The width is fixed at the Standard Model value [18]:  $2.094 \pm 0.002$ .

In this work, the choice of the  $W$  width is the functional dependence (2.40).

### 2.3.3 The Off-shell Model

The cross section (at the lowest order) can be expressed by a two-fold convolution of a hard scattering off-shell cross section with Breit-Wigner density functions [24]:

$$\sigma(s) = \int_0^s ds_- \rho(s_-) \int_0^{(\sqrt{s} - \sqrt{s_-})^2} ds_+ \rho(s_+) \sigma^0(s, s_-, s_+), \quad (2.41)$$

where

$$\rho(s) = \frac{1}{\pi} \frac{\Gamma_W M_W}{|s - M_W^2 + iM_W \Gamma_W|^2}, \quad (2.42)$$

is the relativistic Breit-Wigner density function associated to the  $W^\pm$  propagators. The  $s_+, s_-$  are the invariant masses (squared) for the  $W^+, W^-$  and the  $\sigma^0(s, s_-, s_+)$  is the cross section at the lowest order, which contains term corresponding to the CC03  $W$  pair production. Explicit calculations can be found in [24]. The on-shell cross section is simply

$$\sigma^{on}(s) = \sigma^0(s, M_W, M_W). \quad (2.43)$$

An interpretation of equation (2.41) is that the  $W$  mass influences the cross section through the off-shell propagators, all the other parts are approximately independent of  $M_W$  and  $\Gamma_W$  (not including radiative corrections). To incorporate the energy dependence of loop corrections to the  $W$  propagator, an  $s$ -dependent width

$$\Gamma_W(s) = \frac{s}{M_W^2} \Gamma_W, \quad (2.44)$$

is used.  $\Gamma_W(s)$  is called the “running width”. In the simulation described in chapter 4, a fixed width (i.e no  $s$ -dependence) is used. The expression of the  $W$  mass in the two schemes is closely related near resonance by a variable transformation [18]:

$$M_W = M_W^{meas} - \frac{1}{2} \frac{(\Gamma_W^{meas})^2}{M_W^{meas}},$$

$$M_W \approx M_W^{meas} - 27 \text{ MeV}/c^2. \quad (2.45)$$

This  $27 \text{ MeV}/c^2$  correction is applied to the measured  $W$  mass ( $M_W^{meas}$ ) and this dependence is not the one described by the equation (2.40) which concerns the  $M_W$  dependence on  $\Gamma_W$ .

As for the on-shell model, we have to take into account radiative electroweak corrections. The largest effect to the total cross section is the Initial State Radiation (ISR). However, ISR also affects the differential cross-section ( $W$  mass distribution) by softening the expected Breit-Wigner resonant structure. Figure 2.4 displays the effect of ISR and other electroweak corrections to the total  $WW$  cross-section.

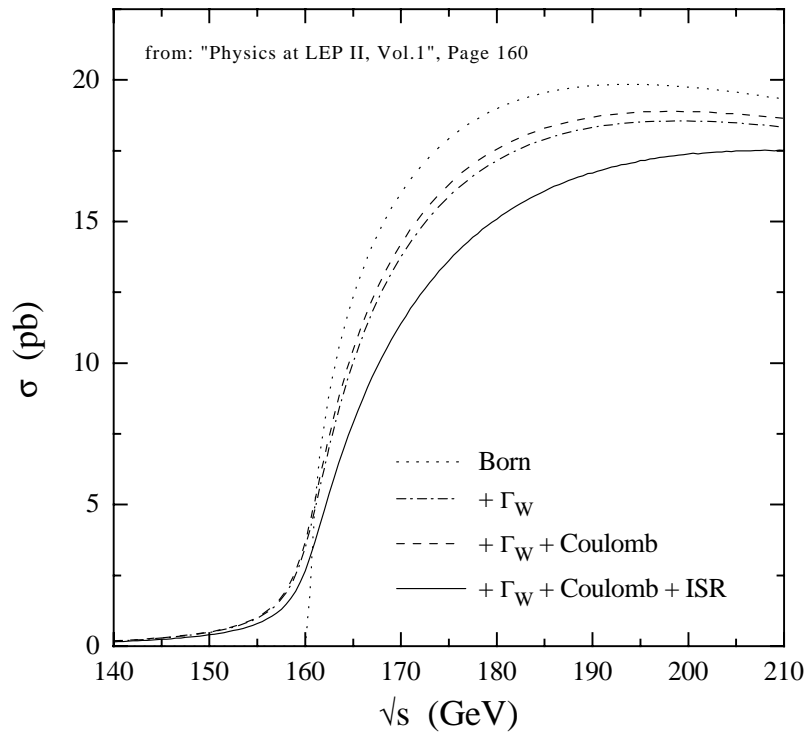


Figure 2.4: *The cross-section for  $e^+e^- \rightarrow W^+W^-$  in various approximations: (i) Born (on-shell) cross-section, (ii) Born (off-shell) cross-section, (iii) with first order Coulomb correction, and (iv) with initial state radiation.*



# Chapter 3

## Description of the Apparatus

### 3.1 The LEP Collider

The Large Electron-Positron (LEP) Collider (Figure 3.1) is the world's largest circular particle accelerator. Its circumference is 26.66 km. Electrons and positrons are delivered to LEP by an injector chain. The electrons are first accelerated to 200 MeV in the Linear Injector of LEP (LIL). Some of these electrons are used to produce positrons by collision with a fixed tungsten target [25]. The electrons and positrons are then accelerated to 600 MeV in the Electron-Positron Accumulator (EPA).

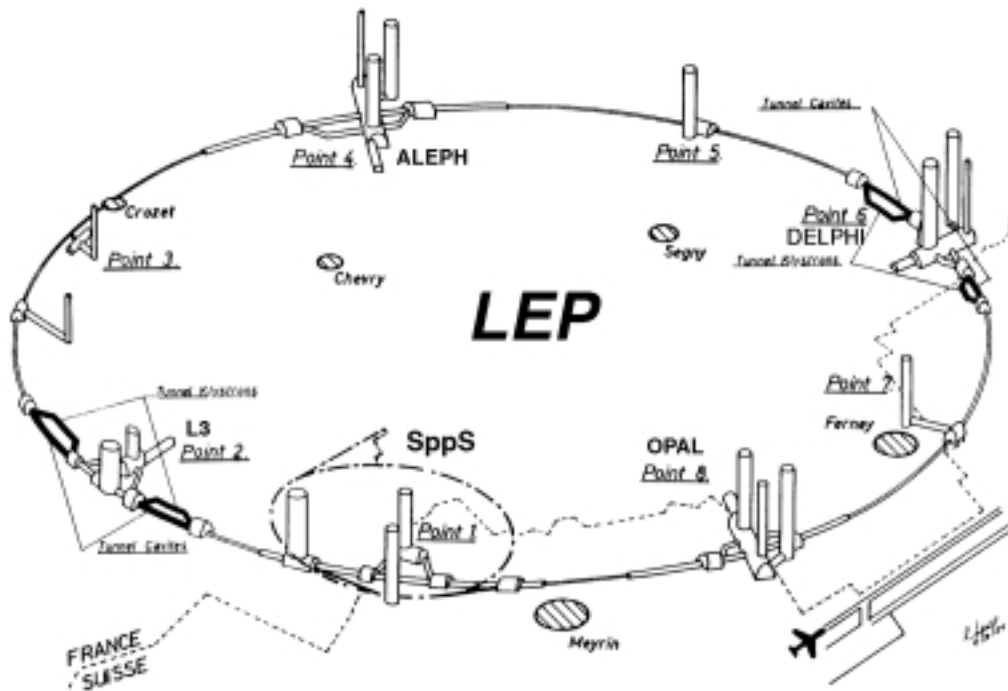


Figure 3.1: Schematic view of the LEP ring with the four experiments and a part of the injector chain.

The beams are injected into the Proton Synchrotron (PS) to accelerate them to 3.5 GeV.

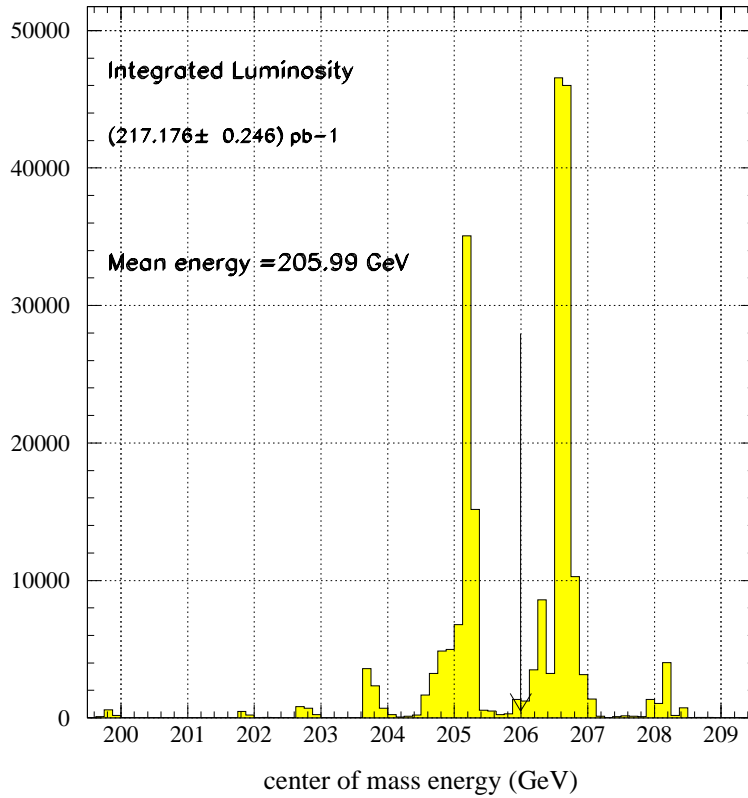


Figure 3.2: *Distribution of the integrated luminosity in 2000 as a function of the CM energy. The mean energy of 205.99 GeV is indicated by the downward vertical arrow.*

The beams are then transferred to Super Proton Synchrotron (SPS), which operates as a 23 GeV injector for LEP. The electrons and positrons are guided by a lattice of bending magnets located around the ring [25].

In the initial configuration, LEP could operate only at beam energies in the order of 45.6 GeV (called LEP I). For LEP II the accelerator was required to increase the energy of the CM system to above  $2M_W \simeq 161$  GeV. This has been achieved by changing resistive radio frequency (Rf) copper cavities with super-conducting NbTi Rf-cavities.

### 3.1.1 Luminosity

The rate  $\dot{N}$  of a given type of interaction is determined by the total cross section  $\sigma$  of the corresponding physical process and the luminosity  $\mathcal{L}$  of the colliding beams

$$\dot{N} = \sigma \mathcal{L}. \quad (3.1)$$

The luminosity at LEP is given by

$$\mathcal{L} = \frac{N^- N^+ k f}{4\pi \sigma_x \sigma_y}, \quad (3.2)$$

where

- $f$  : frequency of the bunch collisions,  $f = 11.246$  Hz,
- $k$  : number of bunches in each beam,  $k = 4$ ,
- $N^-, N^+$  : number of electrons (positrons) in a bunch,  $\approx 54 \cdot 10^{10}$ ,
- $\sigma_x, \sigma_y$  : transverse dimensions of the beam,  $\sigma_x = 145 \mu\text{m}, \sigma_y = 5 \mu\text{m}$ .

The integrated luminosity  $L$ , defined by  $L = \int \mathcal{L} dt$ , delivered by LEP during LEP II is approximately  $700 \text{ pb}^{-1}$  at a CM energy between 161 GeV and 209 GeV (details are given in Table 3.1).

During the year 2000, the LEP machine was in the so-called ‘‘Higgs boson mode’’ to increase the possibility of discovering the Higgs boson. Some techniques have been developed to increase the CM energy. The beams were accelerated to a certain energy, usually 102 GeV, using the full capacity of the machine. The Rf frequency was then shifted to gain a few GeV (between 0.5 and 2.5 per beam). As a result, there are many different CM energy values, between 200 GeV and 209 GeV (see Figure 3.2).

Year	$\sqrt{s}$ [ GeV ]	L [ $\text{pb}^{-1}$ ]
1996	161	11.1
1996	172	10.7
1997	183	56.8
1998	189	174.2
1999	192	28.9
1999	196	79.8
1999	200	86.3
1999	202	41.9
2000	200-205*	81.6
2000	205-209*	134.6
end of LEP	-	702.0

Table 3.1: Value of  $L$ , the integrated luminosity, at LEP II recorded by ALEPH (for the year 2000, see in the text for more details.).

### 3.1.2 The Measurement of the LEP Energy

The LEP beam energy is the absolute scale for measuring the  $W$  boson mass if the event is constrained to the beam energy (see chapter 6). Consequently the beam energy has to be measured very precisely. At LEP I, the average beam energy was obtained with an uncertainty of 1 MeV, using the technique of resonant depolarisation [26].

At LEP II this technique can not be used since the beams are not sufficiently polarised. Instead, one must make several resonant depolarisation measurements at low energy and then extrapolate to higher energies. Most of the beam energy error comes directly from this extrapolation.

## 3.2 ALEPH - Apparatus for LEP PHysics

The ALEPH detector [27] was built to measure the events created by  $e^+e^-$  collisions in LEP and was designed to accumulate as much information as possible. ALEPH is an axially symmetric detector (Figure 3.3) which covers as much of  $4\pi$  solid angle as possible, with the interaction point at the centre of the apparatus.

ALEPH uses a reference coordinate system, with an origin point at the theoretical beam crossing. The positive  $z$ -axis is along the nominal  $e^-$  beam direction. For the two other components, we can use Cartesian  $(x, y, z)$  coordinates ( $x$ -axis pointing through the LEP centre, the  $y$  direction is orthogonal to  $x$  and  $z$ ) or cylindrical coordinates  $(r, \phi, z)$ . The direction of the  $z$ -axis is the same for both systems.

In the following section, short descriptions of each sub-detector are given, starting with those closest to the interaction point and working away from it.

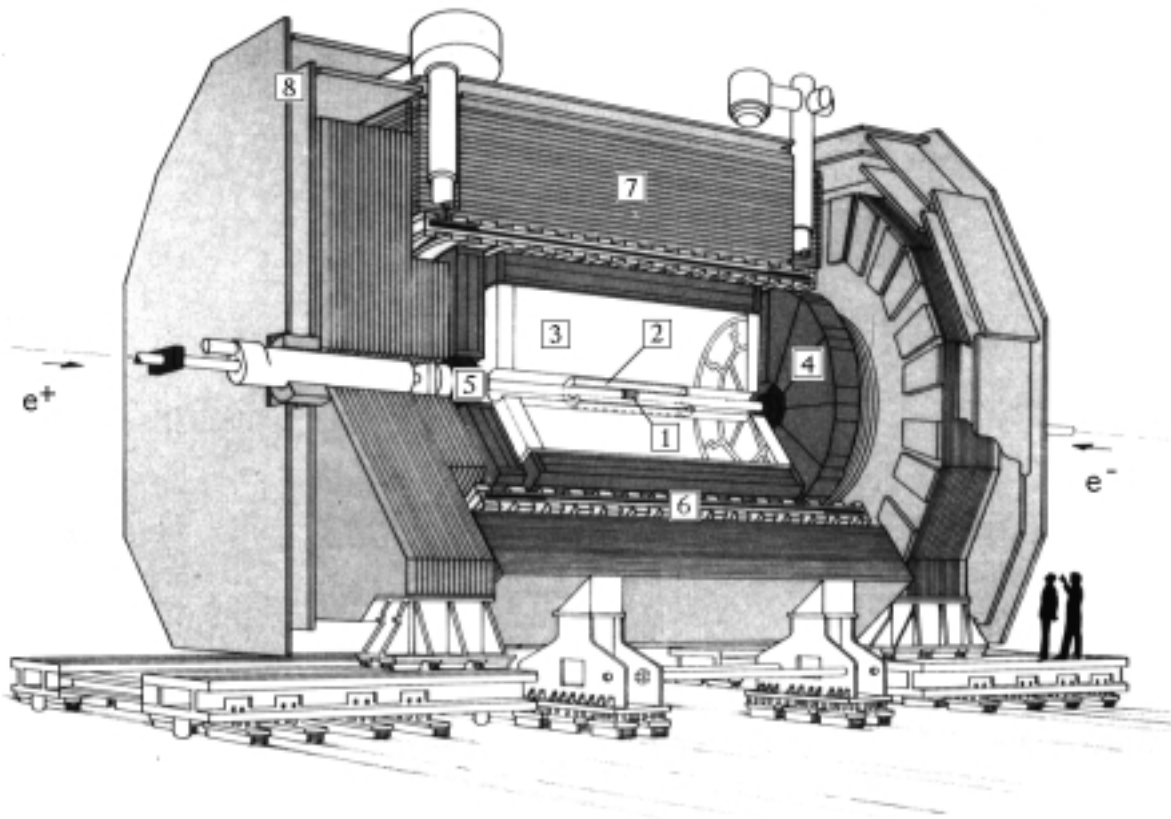


Figure 3.3: *The ALEPH-Detector.* [1]: *Vertex detector, VDET.* [2]: *Inner Tracking chamber, ITC.* [3]: *Time Projection Chamber, TPC.* [4]: *Electromagnetic Calorimeter, ECAL.* [5]: *Luminosity Monitors, LCAL.* [6]: *Superconducting Magnet Coil.* [7]: *Hadron Calorimeter, HCAL.* [8]: *Muon Detection Chambers.*

### 3.2.1 The Vertex Detector

The Vertex Detector is the first sub-detector which a secondary particle meets.

It consists of two concentric layers of double-sided silicon wafers, at average radii 63 mm and 110 mm from the beam pipe and has a total length of 40 cm, providing a polar angular acceptance of  $|\cos\theta| < 0.95$  for detection of charged particles. A photo of the VDET is shown in Figure 3.4. The VDET has a resolution of  $10\ \mu\text{m}$  in the  $r\phi$  direction and  $15\ \mu\text{m}$  in the  $z$  direction for tracks perpendicular to the beam. The VDET is used to identify an accurate position of the vertex of the decay charged products, like hadrons containing  $b$  or  $c$  quarks.

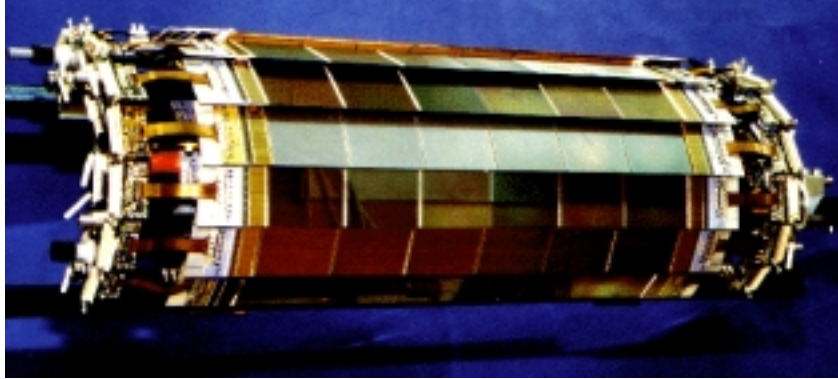


Figure 3.4: *The ALEPH Vertex Detector.*

### 3.2.2 Inner Tracking Chamber

The Inner Tracking Chamber (ITC) is a cylindrical multi-wire drift chamber with a  $ArCO_2$  gas mixture. The active volume is a cylinder of 2 m long and 570 mm in diameter. 960 sense wires are strung in 8 concentric layers which provides 8 accurate  $r-\phi$  points for  $|\cos\theta| < 0.97$ . The wires run parallel to the beam direction and the  $r-\phi$  coordinate is obtained by measuring the drift time, with a precision of roughly  $150\ \mu\text{m}$ . The  $z$  coordinate is obtained by measuring the difference in the arrival times of pulses at the two ends of each sense wire (Figure 3.5), with a precision of 7 cm. It also provides the only tracking information for the level-1 trigger.

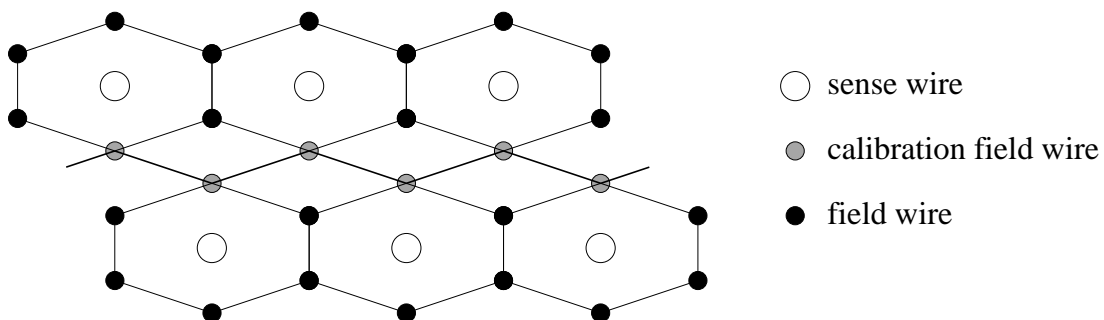


Figure 3.5: *Schematic view of drift cell in the ITC.*

Detector	$\Delta p_t/p_t^2 (GeV/c)^{-1}$
TPC	$1.2 \cdot 10^{-3}$
+ ITC	$0.8 \cdot 10^{-3}$
+ VDET	$0.6 \cdot 10^{-3}$

Table 3.2: *Transverse momentum resolution. Every line is a step further in the reconstruction.*

### 3.2.3 Time Projection Chamber

The Time Projection Chamber (TPC) is the central detector in ALEPH and provides an excellent momentum and angular resolution for charged particles. The TPC has a cylindrical structure with two wire-chamber end-plates and a central membrane (Figure 3.6) and with a length of 4.7 m and inner and outer radius of 0.31 m and 1.8 m respectively. An electric field of 11 kV/m exists between the wire chambers and the central membrane. The electrons produced from ionization of the  $ArCH_4$  gas mixture (91%  $Ar$ , 9%  $CH_4$ ), drift parallel to the beam axis and towards the wire chamber. The  $r - \phi$  coordinate is measured by interpolating the signals induced on cathode pads. The  $z$ -coordinate is determined from the drift velocity and the drift time.

The trajectory of a charged particle in the TPC is a helix due to the strong magnetic field. The TPC can measure 21 points (or hits), of the projected helix on the end-plates and at least four points are required to carry out the helix reconstruction. The trajectory of the charged particle is provided by combining the measurements of the three sub-detector VDET, ITC and TPC. The resolution is given in Table 3.2 and obtained using  $e^+e^- \rightarrow Z^0 \rightarrow \mu^+\mu^-$  events. The other aim of the TPC is to identify different particles. For charged particles

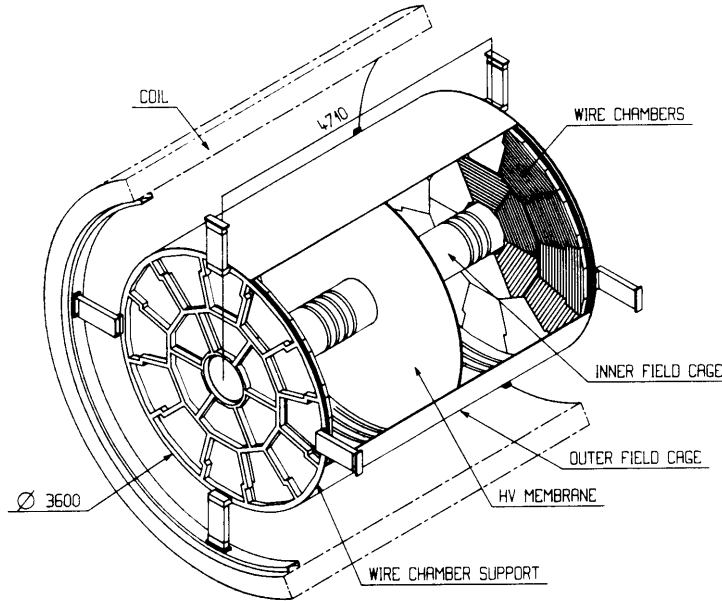


Figure 3.6: *Overall view of the TPC.*

which traverse the entire TPC volume, the ionization is sampled 340 times due to the small spacing between sense wires (4 mm). This is a measure of  $dE/dx$  of a track because the pulse height measured on one sense wire is a direct measure of the number of electrons created by the track in the wire acceptance. The  $dE/dx$  measurement is important for the identification of the electron and also provides an ability to distinguish pions, kaons, and protons in the relativistic rise region. Using the dependence of the mean  $dE/dx$  on velocity and the momentum information, the mass and the identity of a charged particle can be deduced.

### 3.2.4 Electromagnetic Calorimeter

The first three sub-detectors give only tracking information of a charged particle. The aim of the Electromagnetic Calorimeter (ECAL) is to measure the energy of all the electromagnetic showers, neutral (like the photon) or charged. The ECAL is arranged as a barrel surrounding the TPC and as two end-caps (Figure 3.7), so that the calorimeter is hermetic ( $3.9\pi$  solid angle). The ECAL is an alternation of lead and wire chambers, with a nominal thickness of nearly 22 radiation lengths. The barrel and the two end-caps are composed of 12 modules each. In each module, the cathode pads and the wire chambers are arranged in towers, pointing towards the interaction point. Each tower is read out in three sections of depth (each section is called “storey”), corresponding to the first 4, the middle 9 and the last 9 radiation lengths. Cracks account for 2% of the barrel and 6% of the end-cap surfaces. The ECAL energy resolution is

$$\frac{\Delta E}{E} = \frac{0.18}{\sqrt{E(\text{GeV})}} + 0.009, \quad (3.3)$$

for an electron detected in the barrel and emitted at  $90^\circ$ . The resolution of the calorimeter is degraded in two regions, one due to the overlap region where the electromagnetic showers develop into both barrel and end-cap modules and the other close to the inner edge of the calorimeter at low polar angle.

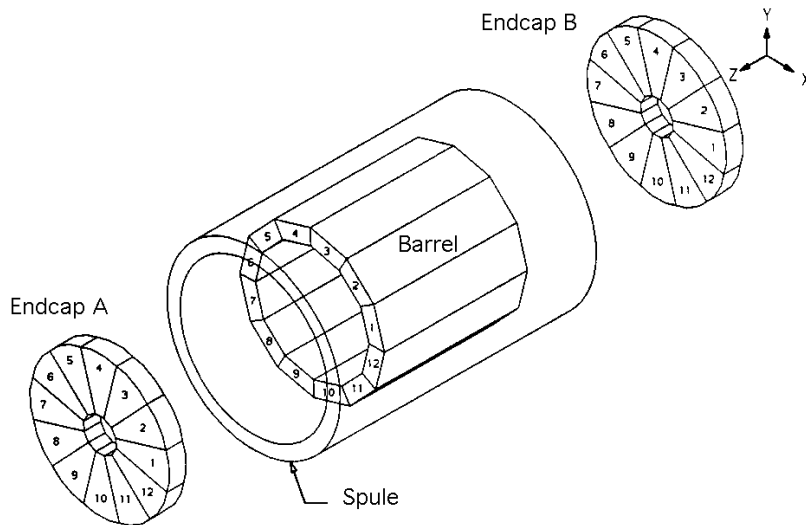


Figure 3.7: Overall view of the ECAL.

With the information from the TPC and the ECAL, electron estimators can be defined (and are used for the lepton selection). The first estimator is the  $dE/dx$  estimator:

$$R_I = \frac{I - \langle I \rangle}{\sigma_I} \quad (3.4)$$

where  $I$  is the measured  $dE/dx$ ,  $\langle I \rangle$  is the average of the measured  $dE/dx$  for an electron and  $\sigma_I$  is the resolution. The  $R_T$  and  $R_L$  estimators measure the transversal and longitudinal dimensions of the electromagnetic showers. Charged tracks are extrapolated from the TPC and their crossing point is computed in each of the three segments in depth of the calorimeter. The estimator  $R_T$  is defined using the four storeys closest to the extrapolated track in each segment as

$$R_T = \frac{E_4/p - \langle E_4/p \rangle}{\sigma_{E_4/p}}, \quad (3.5)$$

where  $E_4$  is the energy deposited in the selected towers,  $p$  is the momentum of the charged track measured in the TPC, the ratio  $E_4/p$  is the mean energy fraction deposited in four central towers and  $\sigma_{E_4/p}$  is the resolution of the ratio. The estimator  $R_L$  is defined by:

$$R_L = \frac{X_L - \langle X_L \rangle}{\sigma_{X_L}}, \quad (3.6)$$

where  $X_L$  is the inverse of the mean position of the longitudinal energy of the shower, defined by:

$$X_L = \frac{E_4}{\sum_{i=1}^4 \sum_{j=1}^3 E_i^j S_j}, \quad (3.7)$$

where  $E_i^j$  is the energy deposited in the selected storeys  $i$  of segment  $j$  and  $S_j$  is the mean depth of energy deposition in that segment. All the electron estimators are normalised.

### 3.2.5 Super-conducting Magnet

The Magnet consists of a fully calorimetrized iron yoke (HCAL, see next paragraph) and a super-conducting solenoid producing a uniform field of 1.5 T parallel to the LEP beam direction and corresponding in uniformity to the TPC requirements. The solenoid operates at 4 Kelvin, using 5000 A and consuming only 100 W of power for refrigeration purposes.

### 3.2.6 Hadron Calorimeter

The large iron structure that constitutes the main support of ALEPH and contains the return flux of the magnetic field also acts as the absorber for hadrons and helps to identify muons (Figure 3.8). Like ECAL, the Hadron Calorimeter, HCAL, is subdivided in a barrel which consist of 12 modules and two end-caps, each with 6 modules. Each module is structured into 23 iron slabs and the active detector is inserted between two slabs. This active detector is composed of limited streamer tubes.

The resolution of HCAL for pions is

$$\frac{\sigma_E}{E} = \frac{0.85}{\sqrt{E} [GeV]}. \quad (3.8)$$

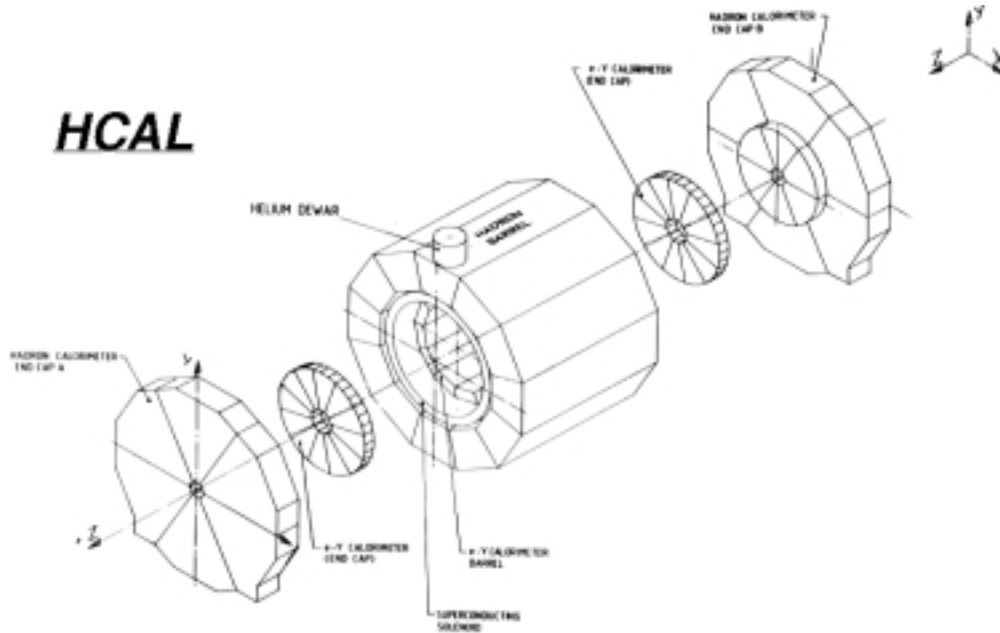


Figure 3.8: Overall view of the HCAL, showing the individual modules of the end-caps and barrel regions.

### 3.2.7 Muon Detection Chambers

On the outer side of the HCAL, two double layers of limited streamer tubes are used to detect the muons which have traversed the full iron thickness. Since the layers are separated from each other by 50 cm, the position and the angle can be measured. The spatial resolution of the muon chamber is 3.5 mm.

### 3.2.8 Luminosity Monitors

As already mentioned, the measurement of the luminosity provides the normalisation for the measurement of cross-sections. Using the theoretically well-known QED Bhabha scattering process ( $e^+e^- \rightarrow e^+e^-$ ), the luminosity is found from the number of events detected divided by the Bhabha cross section. The differential Bhabha cross section (lowest QED order) in the approximation of small angle scattering is obtained by integrating the differential cross section:

$$\frac{d\sigma}{d\Omega} \simeq \frac{4\alpha^2}{E^2} \frac{1}{\theta^4}, \quad (3.9)$$

where  $\Omega$  is the solid angle,  $E$  the beam energy and  $\alpha$  the fine structure constant. At low angles, weak interference effects are strongly reduced. The luminosity monitors are composed of:

- The Luminosity Calorimeter (LCAL), used for off-line analysis.
- The Silicon Calorimeter (SICAL) was the principal luminosity monitor for LEP I. At the start of LEP II the SICAL provides a cross check for the LCAL.

- The Bhabha Calorimeter (BCAL), is located closer to the beam pipe and is used for on-line analysis.

### 3.3 Trigger System

The major purpose of the ALEPH trigger is to identify all events involving  $e^+e^-$  initial states and to initiate the readout system, while reducing the rate of background events (non- $e^+e^-$  initial states) to a “low” level [27]. A “low” trigger rate ( $\sim 10$  Hz) is one that is compatible with the expected physical  $e^+e^-$  interaction rate. In addition, another trigger was set-up, being sensitive to two-photon interactions.

Keeping the total trigger rate at a low level is necessary for the following technical reasons:

- The open-time for the TPC gate [27] is reduced.
- The dead-time (read-out time for the electronics) is reduced to an acceptable limit.
- The amount of unwanted data recorded on disk is reduced.

For these reasons, the trigger was designed in three different levels. The first level (Level 1) provides a decision within  $5 \mu\text{s}$ , which is fast compared to the time between two beam crossings ( $23 \mu\text{s}$ ) [28]. This decision is based on the presence of electromagnetic energy or a coincidence between a charged track detected in the ITC and energy in one of the calorimeters.

After a positive decision at Level 1, the second level (Level 2) verifies some of the Level 1 charged track triggers by replacing the ITC tracking information by the TPC tracking information available  $50 \mu\text{s}$  after the beam crossing (time required for the ionization electrons to drift to the TPC end-plates). After a positive Level 2 decision, the whole detector is “read out”.

Thus the next event which may be seen in the detector is the following third beam crossing.

The Level 3 trigger (Level 3), which is defined in software, is used to reject background events passing Levels 1 and 2 (such as beam gas interactions or off momentum particles hitting the collimators). The rate at Level 3 is then reduced to 1-2 Hz which is consistent with the expected event rate at the  $Z^0$  resonance.

#### 3.3.1 Detector Components used in the Trigger

The sub-detectors involved in the trigger scheme are HCAL, ECAL, LCAL, ITC and TPC. In order to monitor the  $e^+e^-$  collision rate, trigger signals from the luminosity calorimeters (SICAL and BCAL) are also used. To correlate the presence of the particle signals in the various detector elements, the apparatus is divided into projective segments of the different sub-detectors.

#### 3.3.2 Creation of Physics Trigger

Three complementary triggers are used to select  $Z^0$  decays in Level 1 (see Table 3.3):

- The total energy trigger is derived from the ECAL modules by adding the signals from the wire plane of the barrel and of the end-caps. An minimum energy of 5.5 GeV in the barrel, or 4.6 GeV for one end-cap, or 1.7 GeV in each end-cap is required.
- The electromagnetic track trigger requires a track candidate in the ITC in coincidence with an energy deposit in an ECAL module to which the track is pointing.

- The muon track trigger is based on ITC-HCAL coincidence and requires a track in the ITC in coincidence with four planes of HCAL tubes in the same azimuthal region.

Some of these three complementary triggers are updated at Level 2 (that is, the TPC is used at Level 2 to confirm the ITC information used at Level 1). In addition two other triggers are used to calculate the trigger efficiency.

- An electromagnetic track trigger is based on a low ECAL wire energy threshold (less than 200 MeV) but with a more restrictive requirement on the ITC track. This trigger has a higher background, especially at high energy. Therefore, it is down-scaled and tightened by requiring the presence of two ITC tracks.
- A back-to-back trigger is constructed by requiring two track segments back-to-back in the ITC. This trigger must be confirmed at Level 2.

Other triggers, with a larger rate, are used for verification purpose, such that every event does not need to be written on tape. A scale factor is used, meaning that a fraction only of these triggers is kept. Other triggers are used only for testing purpose, so they are enabled on request.

At the  $Z^0$  peak, the Level 2 rate is of the order of 4-5 Hz, where Bhabha events in the luminosity calorimeter contribute 2-3 Hz,  $Z^0$  events and two-photon events contribute about 0.5 Hz each, and the remainder is electronic noise, cosmic rays and beam related background.

At higher energies, the rate is of the order of 5-6 Hz, due to higher beam related background and two-photon interactions.

The basic triggers for hadronic events are the total energy trigger and the muon track triggers. These two triggers are independent and are more than 99.7% efficient for the hadronic decays. Their combined efficiency exceeds 99.999% with an uncertainty of less than 0.001%.

For the purely leptonic final states, the main triggers are the total energy, the electromagnetic and muon track triggers. Since there are two leptons which can trigger independently, the single lepton efficiency is measured from the observed number of events in which one or both events have triggered and is used to calculate the overall efficiency for lepton pairs. Since the bending of the magnetic field prevents back-to-back high momentum tracks from simultaneously pointing to insensitive regions between modules, the trigger inefficiency for all lepton channels is less than  $3 \cdot 10^{-5}$ .

### 3.4 Data Acquisition

The Data Acquisition (DAQ) has the primary task of reading out the data coming from every sub-detector, following a Level 2 “yes” decision. Following the data stream from the sub-detector to the reconstruction of the physics events, a tree-like architecture is used. The Readout Controllers are used to initialise the sub-detector readout and create a new data format. Then this information is sent to the Event Builder which builds a “sub-event” for each sub-detector. All the “sub-events” are collected by the Main Event Builder, which performs a synchronisation and checks the event completeness. As part of the Main Event Builder, the Level 3 trigger is called to reject unwanted events. At the end of the chain, the Main Readout Computer collects all the accepted events. The “online” analysis, the event display and verification tasks are then performed and the event is stored. The event reconstruction is another task of the DAQ.

### 3.4.1 Event Reconstruction

The Facility for ALepH COmputing and Networking (FALCON) performs directly the reconstruction of the event after a “run”<sup>1</sup> has been taken and written on tape. FALCON operates in two modes:

- The processing of raw data shortly after a run ends.
- At the end of the data taking periods, the full set of data is reprocessed using the currently best knowledge of the detector.

The output of FALCON is ready to perform an analysis (the format of the output is called Production Output Tape (POT)). The POTs are then transferred to the CERN Computer Centre, where they are stored.

The full reconstruction is performed by one single program called Job to Understand Lep Interactions in Aleph (JULIA) which is executed from FALCON. The information from each sub-detector is treated in the following steps:

- the charged tracks are reconstructed;
- the  $dE/dx$  of the charged tracked is obtained from the TPC wire information;
- the primary vertex is then reconstructed;
- Calorimeter energy deposits are clustered;
- the energy flow [29] analysis is performed;
- the particles are identified.

The energy flow algorithm [29] is used to improve the resolution of the visible energy in an event. This algorithm also avoids double counting by taking into account redundant information. One aspect of quality criteria imposed on ALEPH data is that all entries in this algorithm are well measured. The first step of the energy flow algorithm is to remove all possible noise of the calorimeter and exclude badly reconstructed tracks. After the so-called “cleaning” is done, the charged tracks are required to have at least 4 hits in the TPC. The trajectory of each track is then extrapolated through the ITC and the VDET. If the track originated from the interaction point, the track is kept. If it is not the case, a study of the secondary vertex allows to determine if there is a neutral particle with a short decay length (like a B meson) or not. The tracks are then extrapolated to the calorimeter.

A list containing all objects in the detector is created. A particular treatment is then applied for different particle types:

- For electrons, the deposit in the ECAL is analysed. If the energy measured in the calorimeter does not agree<sup>2</sup> with the energy calculated from the momentum coming from the tracking, an additional particle is created with the energy difference, and it is attributed to be a photon bremsstrahlung. The electron and the bremsstrahlung photon are then removed from the list.

---

<sup>1</sup>A run is, in ALEPH, a certain number of events, corresponding to 2 hours of data taking or at most 600 Mbytes.

<sup>2</sup>More than 3 standard deviations.

- The muons identified in the muon chambers or with their HCAL pattern are subtracted from the list of object.
- The identified photons are also removed.
- The remain objects, seen in the detector, are then split into 2 parts, the neutral and the charged objects, with their respective four-momenta.

The physics analysis of interest can then start.

Trig Bit	Scale Factor	In	Short Name	Long Name Description
0	65000		RNDM_TST	Random Test Trigger (PLU-Level)
1	20	Y	SNG_C_E2	Single Charged ElMag * ITC_RPZ(No TPC)
2	1	Y	SNG_N_EL	Single Neutral ElMag Energy
3	1		TAG_SNGC	Single Charged ElMag * BCAL_TRG
4	5	Y	SiCAL_ME	SiCAL High * Low
5	1	Y	LW_LO_HI	LCW_A_Low * B_high + A_high * B_Low
6	20	Y	LW_A+BLO	LCW_A_Low + LCW_B_low
7	1	Y	LW_A+BVH	LCW_A_high + LCW_B_high
8		Y	SNG_MUON	Single Muon (No TPC update)
9		Y	SNG_C_EM	Single Charged ElMag (No TPC update)
10			MIST_LV2	(L1 Cycle: OFF, L2 CYCLE: ON)
11				
12			LW_A_LOW	single arm side A
13			LOW_B_LOW	single arm side B
14			BCAL_TRG	Single Arm BCAL (10 GeV in 1/4 module)
15		Y	SNG_MUX2	SNG_MUON (TPC update)
16		Y	SNG_EMX2	SNG_C_EM (TPC update)
17		Y	ETT_EWBA	Total Energy ECW Barrel
18		Y	ETT_EWEA	Total Energy ECW Endcap A
19		Y	ETT_EWEB	Total Energy ECW Endcap B
20		Y	ETT_EWE*	Total Energy ECW (Endcap A * Endcap B)
21		Y	VDET_LSR	MiniVertex LaserShot (External)
22				
23		Y	TPC_LASR	TPC Laser Shot (External)
24				
25			Z0_Trigg	SNG_C_EM * SNG_MUON
26			TRK_CNT1	ITTC >2, Lv2 = TPTI >2
27		Y	TRK_CNT2	ITBB, Lv2 = (TPTI+TPTO)>1
28			T0_SYNCH	On if T0_Module NOT synchronised to beam
29		Y	DBL_C_E2	SNG_C_E2 * ITTC ≥ 2 (TPC update)
30		Y	COS_HCBA	ITBB * HCW(≥ 10 double planes)
31		Y	RNDM_TRG	DownScaled GBX-Trigger (External;TPU)

Table 3.3: Physics triggers (an example from MAY 1999, \* = “AND”, + = “OR”). Y means that the trigger is enabled.

# Chapter 4

## Monte Carlo Simulation

In the previous chapter, a description of the treatment of the data coming from the ALEPH detector was given. Now the simulation tools are introduced which are used to:

- compare a model to the experimental data,
- develop and test the reconstruction programs,
- check the sensitivity of variables to a physical parameter (i.e.  $M_W$ ),
- design and optimise the analysis.

Monte Carlo techniques are very useful to fulfil such requirements. They are based on random numbers which are used to simulate physics processes. A given Monte Carlo simulation is usually composed of several programs, where each program is dedicated to reproduce a specific model (or theory) or to simulate the experimental setup. The discussion will be limited to the Monte Carlo simulations or programs which are used in the analysis described in this thesis.

### 4.1 Generators

As a first step, a Monte Carlo package needs to be chosen to test the associated theoretical predictions. In this context, the execution of a typical Monte Carlo simulation consists of three steps:

- Initialisation including the input parameters;
- Event generation where an event routine is called;
- Closing evaluation where the total cross section is calculated.

#### 4.1.1 $WW$ Monte Carlo Simulation

##### KORALW

The Monte Carlo package used to simulate the production of  $W$  events in ALEPH is KORALW, version 1.21 [30]. This generator is based on a so-called Master Formula, detailed in reference [30]. This master formula represents all the knowledge of the theory, with some simplifications due to finite calculation time. In particular, KORALW includes the full lowest order  $e^+e^- \rightarrow 4f$  process, but with approximations of the radiative (QED) correction.

To generate the full set of 4-fermion diagrams and their associated matrix elements, the GRACE package [31] with fixed  $W$  and  $Z$  widths is used.  $O(\alpha)$  corrections can be separated in two classes depending on the following criteria. If the radiative correction affects only one branch, the radiative correction is said factorizable. Factorizable QED corrections are taken into account by the YFS [32] exponentiation method. This method can include Infra-Red (IR) photonic corrections before the Monte Carlo simulation takes place. Currently, only  $3^{rd}$  order ( $\alpha^3$ ) real corrections have been calculated. The generation of the 4-momenta for each  $W$  decay is done by sampling an approximate phase space distribution (after the application of the YFS method). In order to recover the original phase space distribution, events falling below a certain weight are discarded. The main properties of this generator are the following:

- matrix element for  $W$  pair production,
- decay of the  $W$  boson into massive fermion,
- kinematics with exact four momentum conservation for the entire  $WW$  creation and decay processes.

The width of the  $W$  boson is taken from the Standard Model predictions ( $\Gamma = 2.094 \pm 0.014 \text{ GeV}/c^2$ ).

In order to use KORALW events, several interfaces are provided, which will be describe later in the section 4.2. However, the QED corrections are not implemented in a complete way. This might not be sufficient for a precision measurement [33]. Therefore, additional and independent Monte Carlo programs are also used to check the KORALW output, e.g. the RacoonWW (RAdiative CORection ON  $e^+e^- \rightarrow W^+W^- \rightarrow 4f$ ) [34] and the YFSWW [35] Monte Carlo simulations.

### RacoonWW

As explained in chapter 2, the  $W$  boson is not a stable particle. Therefore, the final state is not composed of the two  $W$  bosons, but their decay products instead. Problems can arise from a singularity at the pole. At LEP II, the  $W$  bosons are produced almost on-shell<sup>1</sup>. To take advantage of this fact, one can project the off-shell matrix element onto the on-shell matrix element. This approximation is called the Double Pole Approximation (DPA) in the case of doubly resonant bosons. Usually, one refers to the leading pole approximation. More details concerning this calculation are given in [33]. The DPA is used in the RacoonWW Monte Carlo simulation to estimate the virtual  $O(\alpha)$  corrections to  $e^+e^- \rightarrow W^+W^- \rightarrow 4f$ . No additional approximations are applied for the virtual photonic corrections. For the real photonic part of the higher orders corrections, the full matrix element of the process  $e^+e^- \rightarrow 4f\gamma$  and the Initial State Radiation are treated via the structure function approach [33]. Unfortunately, the RacoonWW Monte Carlo generator has negative weights. This feature of the program does not allow an efficient generation. This means that RacoonWW is only used at generator level to compare its prediction with the one of YFSWW.

### YFSWW

Concerning the real correction, the basic principles of YFSWW are similar to KORALW. The YFS exponentiation is used to calculate the real radiative corrections up to  $3^{rd}$  order. For the virtual correction, a leading pole approximation is also used. The three doubly resonant

<sup>1</sup>This does not mean that the  $W$  boson is stable, but it is a real particle in this case.

CC03  $WW$  contributions are the only diagrams used in the generation. This means that there are two possibilities to use YFSWW, either to generate full reconstructed events or to interface this generator with KORALW. In the context of this work, the interface approach is used. The relevant information is that YFSWW and KORALW have a common base: the doubly  $W$ -resonant ( $WW$ ) process with the same universal<sup>2</sup> radiative corrections.

### 4.1.2 Background

As seen in chapter 2, there are several different processes which may produce a 4-fermion final state which is not a doubly resonant  $W$  boson. These background processes should be rejected (if possible) or well controlled. Moreover, 2-fermion final states cannot be excluded so easily. Therefore a brief description of all types of background generators is given in the following section.

#### PYTHIA

PYTHIA [36] was used to produce the following background processes:

- $e^+e^- \rightarrow Z/\gamma \rightarrow q\bar{q}(\gamma)$ ;
- $e^+e^- \rightarrow ZZ$ ;
- $e^+e^- \rightarrow We\bar{\nu}$ ;
- $e^+e^- \rightarrow Ze^+e^-$ .

Two points are worth noting. Firstly, certain topologies of  $ZZ$  events are included in the 4f-GRACE package. These “ $WW$  like” events must be removed from the  $ZZ$  sample in order to avoid double counting. Secondly, the  $We\bar{\nu}$  process is treated as background, since this process is not a doubly resonant diagram.

#### KORALZ

KORALZ [37] has the same fundamental principle as KORALW except that it is used to generate single  $Z^0$  production instead of doubly resonant  $W$  production. The only decay channel considered is  $e^+e^- \rightarrow Z/\gamma \rightarrow \tau\tau$ . There is the possibility that  $\tau$ -pair events could look like  $W$  pair events, since the  $\tau$  can either decay into a low multiplicity jet or into a lighter charged lepton.

#### PHOTO2

At LEP II, the process with the largest cross section is a two-photon initial state interaction. For these events, it is very unlikely to see a large energy deposit in the detector or a large multiplicity event. However, the cross section is so large that some of the events may be produced in phase space regions similar to  $WW$  physics, so it also needs to be considered as background. The events are simulated using PHOTO2 [38].

---

<sup>2</sup>Universal corrections are Initial State Radiation (ISR), Final State Radiation (FSR) and the Coulomb correction.

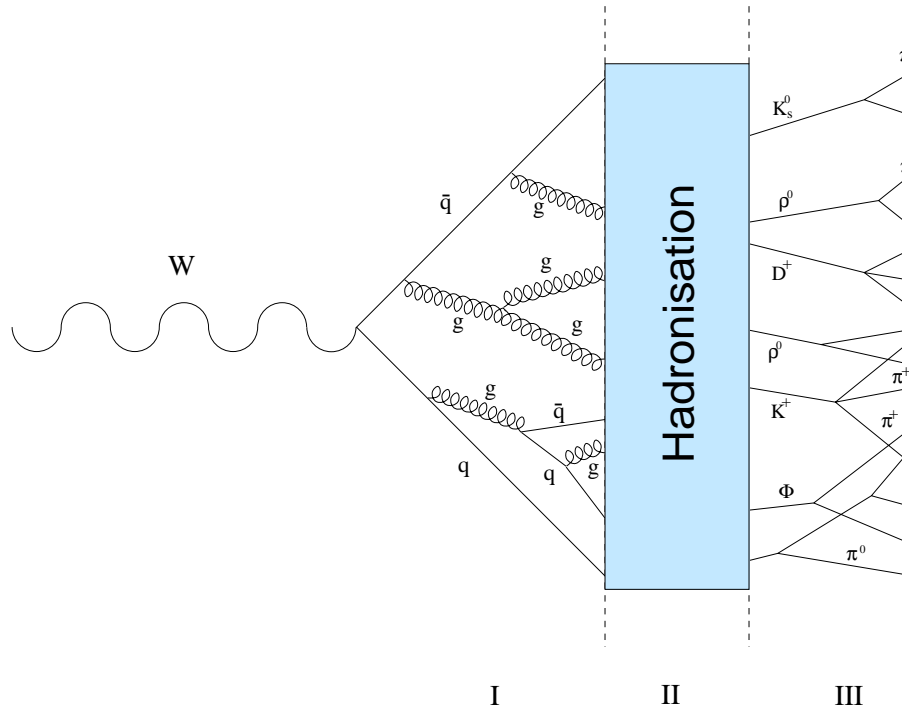


Figure 4.1: View of the parton shower and the fragmentation process. The three phase are explained in the text.

## 4.2 External Packages

After the generation phase, there are 4-fermions (or 2-fermions for some background reactions) in the final state. QCD effects [39] and the radiation in the final state have not yet been taken into account. Therefore, external packages are used to simulate the fragmentation<sup>3</sup> of the quarks and to implement the Final State Radiation (FSR).

### 4.2.1 Fragmentation

The evolution of a quark into observable hadrons can be separated into three phases, as shown in Figure 4.1.

**The first phase:** Parton branching process.

The evolution of the initial quark in the colour field is described by the Altarelli-Parisi equation [40]. A quark may radiate a bremsstrahlung gluon, which intern may split into a quark-antiquark pair or a pair of gluons, as shown in Figure 4.2. A parton shower develops until the available momentum transfer for subsequent branching is below some threshold. At that point, hadronisation sets in.

This technique is used by the JETSET [36] model and by the HERWIG [41] model. Another approach is called the dipole cascade model in the ARIADNE [42] model. The quark pair radiates a gluon. The resulting  $q\bar{q}g$  is then treated as two dipoles, one between the quark and the gluon or the gluon and the antiquark. Every produced dipole radiates a gluon which produces a new dipole.

<sup>3</sup>The fragmentation process is defined as the hadronisation and the subsequent decay.

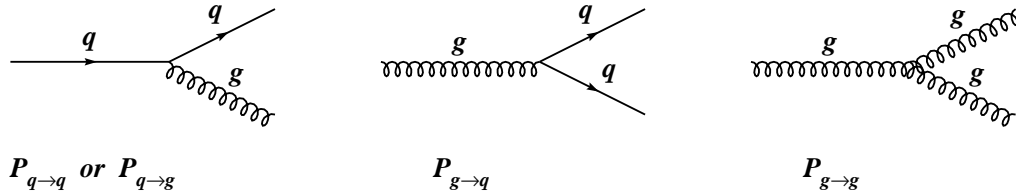


Figure 4.2: Schematic view of the three possible processes in the parton shower: Radiation of a gluon, production of a quark antiquark pair and gluon splitting.

**The second phase:** Hadronisation.

The hadronisation process is not (yet) theoretically calculable from fundamental principles.

Phenomenological models are used to describe the transition from colour partons to colourless hadrons. In the string fragmentation model, a colour flux tube is stretched between quarks. As the distance between the quarks increases, the density of energy of the string becomes larger. When the energy of the string is large enough, the string breaks to produce a new pair of quark. As the string breaks and a new quark-antiquark is created, the energy in the new strings is reduced. This process stops when there is not enough energy to produce a new pair quark-antiquark. This approach is used by the JETSET and ARIADNE package.

Another model is the so-called cluster model. At the end of the parton shower, all gluons split into quark-antiquark pairs. Neighbouring  $q\bar{q}$  pairs are merged into a cluster if the resulting cluster is colour neutral. If the cluster is heavier than a given mass, it will decay into a pair of lighter cluster otherwise it will decay into hadrons. The difference between a cluster and a hadron is the following: a hadron is on-shell, whereas a cluster is off-shell. If the cluster can not decay into two on-shell hadrons, it decays into two off-shell clusters (or one on-shell hadron and one off-shell cluster). This continues until only on-shell hadrons exist in the final state. This approach is used by the HERWIG package.

**The third phase:** Decays of unstable particles.

After hadronisation, a set of primary hadrons is produced. Unstable short-lived particles decay according to the corresponding matrix element. Measurement of lifetimes, masses and branching fraction are incorporated into the model. The JETSET package is found to be in better agreement [39] with the data at the  $Z^0$  resonance; therefore the HERWIG and ARIADNE models are only used to assess a systematic uncertainty for the fragmentation.

### 4.2.2 Final State Radiation

The final state interaction (bremsstrahlung with matter for electrons or radiation of photons in the final state) of the leptons is also simulated. The package which is used for final state radiation is PHOTOS [43]. GEANT [44] is used to simulate the electron bremsstrahlung in matter. PHOTOS [43] simulate final radiation from electrons and muons. The algorithm used in PHOTOS is based on a second order calculation of charged particle radiation in a leading-log approximation.

### 4.3 Detector Simulation

So far, only physics processes have been simulated. However, the behaviour of the ALEPH detector for these processes must also be simulated. The package, simulating all the sub-detectors, is called GALEPH [45]. GALEPH is based upon GEANT [44], version 3.21 which treats the detector (or sub-detectors) as geometrical volumes. The main duty of GEANT (or GALEPH) is the “transport” of particles through an experimental setup. The GEANT package simulates:

- **tracking devices.** A tracking device is characterised by the tracking parameter of the media which fills the volume. Moreover, GEANT also simulates multiple-scattering, energy loss through ionization and decays of particles using Monte Carlo techniques.
- **the calorimeters.** The electromagnetic and hadronic interactions of a generated particle with atoms and nuclei in the calorimeter are simulated by the Monte Carlo EGS [46] and GHEISHA [47] packages, respectively.
- **the electron bremsstrahlung.** The electron bremsstrahlung is very important for this analysis since one of the studied final states is composed of a high energetic electron. 44 % of these electrons are emitting bremsstrahlung photons with sizeable energies.

The propagation of the simulated analog signal is further simulated through the electronic chain. This signal is digitised by simulation of the electronics from each detector, allowing effects like thresholds, noise or gain fluctuations.

### 4.4 Summary

After GALEPH, the simulated events pass the program JULIA (see section 3.4.1) for reconstruction. These events, at this level, are treated in exactly the same way as real events. Therefore, simulated and real data can be subjected to the same analysis programs. The generated numbers of events are given in Appendix B, for all CM energies which are studied in this thesis.

# Chapter 5

## Event Selection

The distinguishing feature of  $W^+W^- \rightarrow \bar{q}qe\nu$  and  $W^+W^- \rightarrow \bar{q}q\mu\nu$  events, the signal, is the presence of a high momentum, isolated electron or muon, originating from the interaction point, along with a large amount of missing momentum. The data set which is used in this work has been collected by ALEPH at energies in the range of  $189 \leq \sqrt{s} \leq 209$  GeV and corresponds to an integrated luminosity of  $L = 650 \text{ pb}^{-1}$ . The selection of semi-leptonic events is done in the following way.

A preselection step with cuts against the dominant background is followed by the selection of events with an isolated electron or an isolated muon. The selection searches firstly for muon events. Remaining events are then tested against electron criteria. The remainder of the events which are not tagged as electron or muon events is divided in two groups, namely the 4-quarks or  $\tau\nu q\bar{q}$  exclusively. However, in this work, only the  $e(\mu)\nu q\bar{q}$  channel will be considered. After clustering the hadrons into jets, the selection is refined by using a neural network analysis.

### 5.1 Preselection

The aim of the preselection is to remove various types of backgrounds, which have a completely different topology than the  $WW \rightarrow e(\mu)q\bar{q}$  events, such as beam gas and two-photon interactions, without losing efficiency for selected signal events. These background events are relatively easy to exclude as they either do not originate from the interaction point or have a very low visible energy. In order to reject contributions from these events, one defines a “good” charged track. Such a track fulfills the following criteria:

- It has four or more measured space points in the TPC;
- It originates from a cylinder of length 20 cm in the  $z$ -direction and a radius of maximum 2 cm centred on the interaction point;
- The angle  $\theta$  between the beam and the track in question has to be  $|\cos(\theta)| < 0.95$ .

All events which do not have four good charged are removed. Consequently most of the purely leptonic events are removed. In addition, the total energy of all the good charged tracks has to be larger than  $0.10\sqrt{s}$ . This cut removes two-photon interactions. A cut on the missing momentum is used to reduce the  $e^+e^- \rightarrow Z^0/\gamma \rightarrow qq\gamma$  contribution, where  $\gamma$  is an ISR photon. The ISR photon is mainly emitted along the beam pipe. This leads to an unbalanced longitudinal momentum in a particular topology. A set of cuts can be derived to

remove this background. The missing momentum of the event can be calculated by applying the four-momentum conservation<sup>1</sup>. The energy of the photon is then:

$$E_\gamma = \frac{E_{cm}}{2} \left( 1 - \frac{M_Z^2}{E_{cm}^2} \right), \quad (5.1)$$

where  $M_Z$  is the  $Z^0$  mass and  $E_{cm}$  the CM energy. A two dimensional cut on the longitudinal missing momentum ( $\not{p}_z$ ) is then applied:

$$\not{p}_z < \max \left( 2E_\gamma - \sqrt{\not{E}^2 - \not{p}_t^2} - 6, E_\gamma - 27.5 \right), \quad (5.2)$$

where  $\not{E}$  is the missing energy and  $\not{p}_t$  is the missing transversal momentum.

## 5.2 Lepton Selection

In order to find the lepton, a loop runs over all the measured charged tracks belonging to the event. Each track is then in turn excluded from the event and the rest of the event is clustered into 2 jets, using the jet algorithm described in the next section. A discriminant variable is then calculated for each track:

$$V = P * \sin \theta, \quad (5.3)$$

where  $P$  is the momentum of the particle and  $\theta$  the isolation angle of track. The track which maximises this discriminant variable is then taken as the lepton track. If the sum of the missing momentum and the momentum of this lepton candidate is smaller than 30 GeV/c, the event is rejected. This means that  $W^+W^- \rightarrow q\bar{q}q\bar{q}$  events, which are fully contained in the detector and essentially have no intrinsic missing momentum, will be rejected with this cut.

### 5.2.1 Electron

Three normally distributed identification variables are used to identify electrons. These are the mean of  $dE/dx$  in the TPC ( $R_I$ ), the transverse ( $R_T$ ) and longitudinal ( $R_L$ ) profiles of the electromagnetic shower in the ECAL (see section 3.2.4). The value of the fit [29] to  $dE/dx$  is required to converge with at least 50 measured values of  $dE/dx$ . The ( $R_L$ ) estimator is used only to reject event with a wrong measured momentum in the TPC. The other two variables depend on the ECAL geometry:

- Barrel or end-cap region:  $R_T > -3$ ;
- Overlap (between barrel and end-cap) region:  $R_T > -5$  or  $R_I > -0.5$  (the  $dE/dx$  is only used when the electron shower is not fully contained.);
- Crack <sup>2</sup> region:  $R_T > -7$  or  $R_I > -0.5$ .

<sup>1</sup>At this level of the selection, the missing four-momentum is obtained by summing all the four momenta of all energy flow object seen in the detector.

<sup>2</sup>A crack region is defined as an un-instrumented part of the ECAL.

### 5.2.2 Muon

The principal characteristic of muons is their penetration through the whole detector. The selection criteria require at least one signal in the muon chamber or a specific pattern in HCAL (over 7 nuclear interaction lengths). The momentum of the muon must be larger than 3 GeV/c (the minimum momentum required for a muon to transverse the detector material in front of the muon chamber). If the lepton track fulfils both (electron and muon) criteria (2% of the cases), it is taken as a muon candidate.

### 5.2.3 Corrections

The lepton was identified in the previous section. The last step of the “selection” of the lepton is to look for possible radiation of photons, which modify the four-momentum of the lepton. In 44 % of the  $W \rightarrow e\nu$  events, a photon is emitted with an energy larger than 0.5 GeV. If an energy deposit is found in a cone of 2.5 degrees around the impact point of the lepton track with ECAL, the momentum associated to this energy deposit is added to the lepton momentum [63]. Starting from the interaction point, there is a considerable amount of material between the different sub-detectors, i.e interfaces VDET-ITC and ITC-TPC, where bremsstrahlung photons are likely to occur. A cone is then defined for these two cases. If an energy deposit in the ECAL is observed which is within either of these cones, the momentum associated to this energy is added to the electron momentum.

In addition to this detector effect, the possibility that either the electron or the muon radiate a photon<sup>3</sup> is taken into account: the Final State Radiation (FSR). As described in section 4.2, the PHOTOS model is used to generate a photon in 18 % of all the  $W \rightarrow e\nu$  and 9% of all the  $W \rightarrow \mu\nu$ , where 90% of the photons are in a cone of 30 degrees to the charged track. In order to find this photon, the GAMPEX [48] package is used. The momentum of each photon with an energy larger than 500 MeV is added to the lepton track. In the rest of the analysis, the reconstructed lepton is always composed of the track and the photon.

## 5.3 Jet Reconstruction

Quarks have never been observed to exist as free particles. Instead, quarks are said to fragment into “jets” of particles. This hadronisation process is characterised by the fact that the strong force, which binds quarks together, grows as the distance between the quarks. This causes quarks to be permanently bound within hadrons. By clustering together the particles from the quark hadronisation process, one obtains a single entity known as jet. Thus for our purposes, the momentum of a jet represents the best estimate of the momentum of the original quark resulting from the decay of a  $W$  boson.

### 5.3.1 Algorithms

Many algorithms are available to find jets, but only two, JADE [49] and DURHAM [50], are usually used in ALEPH. One begins by defining a metric  $y$  in the phase space of four-momenta of reconstructed particles. The jets are constructed from pairs of four-momenta which lie within a distance  $y_c$  from each other. For each pair of four-momenta  $(i,j)$ , one calculates the corresponding distance,  $Y_{ij}$ , in the phase space.

---

<sup>3</sup>This algorithm is performed after the bremsstrahlung photon search.

New objects are obtained iteratively by adding the 4-momenta of two objects with  $Y_{ij} < y_c$ . This iterative procedure stops when there are no further object-pairs which fulfil this condition. When all the pairs have a distance larger than  $y_c$ , the iteration stops and the remaining individual four-momenta are called jets.

### DURHAM Algorithm

The principal difference between the JADE and DURHAM algorithms is that the DURHAM algorithm reflects more the role of the transverse momentum of a pair of tracks, while the JADE algorithm emphasises the invariant mass of the pair. The DURHAM algorithm uses the definition:

$$Y_{ij} = 2 \min(E_i^2, E_j^2) (1 - \cos \Theta_{ij}) \quad (5.4)$$

where  $E_i, (E_j)$  is the energy of the  $i^{th}$  ( $j^{th}$ ) particle and  $\Theta_{ij}$  is the angle between them (for JADE, the term  $\min(E_i^2, E_j^2)$  is replaced by  $E_{ij} = E_i E_j$ ). The DURHAM algorithm is used because it provides a better angular resolution and is less sensitive to soft gluon radiation [51].

### Clustering Scheme

The jet clustering can be done in different ways, depending on the desired properties of the reconstructed jet. To define the momentum and the energy of the reconstructed jet, we can use the following schemes:

$$\begin{array}{ll} E \text{ Scheme} & \vec{P}_{ij} = \vec{P}_i + \vec{P}_j \\ & E_{ij} = E_i + E_j \end{array}$$

$$\begin{array}{ll} P \text{ Scheme} & \vec{P}_{ij} = \vec{P}_i + \vec{P}_j \\ & E_{ij} = |\vec{P}_{ij}| \end{array}$$

$$\begin{array}{ll} E_0 \text{ Scheme} & \vec{P}_{ij} = E_{ij} (\vec{P}_i + \vec{P}_j) / |\vec{P}_i + \vec{P}_j| \\ & E_{ij} = E_i + E_j \end{array}$$

The  $P$  scheme assigns particles to the correct jet with the highest efficiency (but only the momentum is conserved), albeit with massless jets. The  $E$  scheme (both energy and momentum are conserved) is then used to form the 4-momenta of each jet in a Lorentz invariant way. The combination of the two last schemes is called the ‘‘DURHAM PE’’ scheme. The event is forced into two jets. This part of the selection does not reject events.

### 5.3.2 Jet Energy Corrections

The direct measurement of the  $W$  mass depends strongly on the Monte Carlo simulation (this will be detailed in the following chapters). Therefore, the agreement between data and Monte Carlo simulation is extremely relevant for the analysis. Several checks have to be performed on the reconstructed jet. At the beginning of every running period, the detector is calibrated using data taken at the  $Z^0$  resonance. This data set, roughly  $3 \text{ pb}^{-1}$  taken every year, is also used to perform data and Monte Carlo comparisons. At the resonance,  $Z^0$  are produced

at rest. This means that the jets are back to back and the energy of both jets is half of the  $Z^0$  mass. The jet energy is then compared to the beam energy for data and Monte Carlo simulation, and the double ratio is then built:

$$Ratio = \frac{(E_{jet}/E_{beam})_{data}}{(E_{jet}/E_{beam})_{MC}}. \quad (5.5)$$

Figure 5.1 shows the double ratio as a function of the polar angle of the jet. There is a small but significant discrepancy between data and Monte Carlo simulation, which needs to be taken into account. Most of the discrepancy is in the end-cap region and in the overlap between the barrel and the end-cap. The energy of all the simulated jets is corrected by the value of the double ratio for a given bin in  $\cos\theta$ .

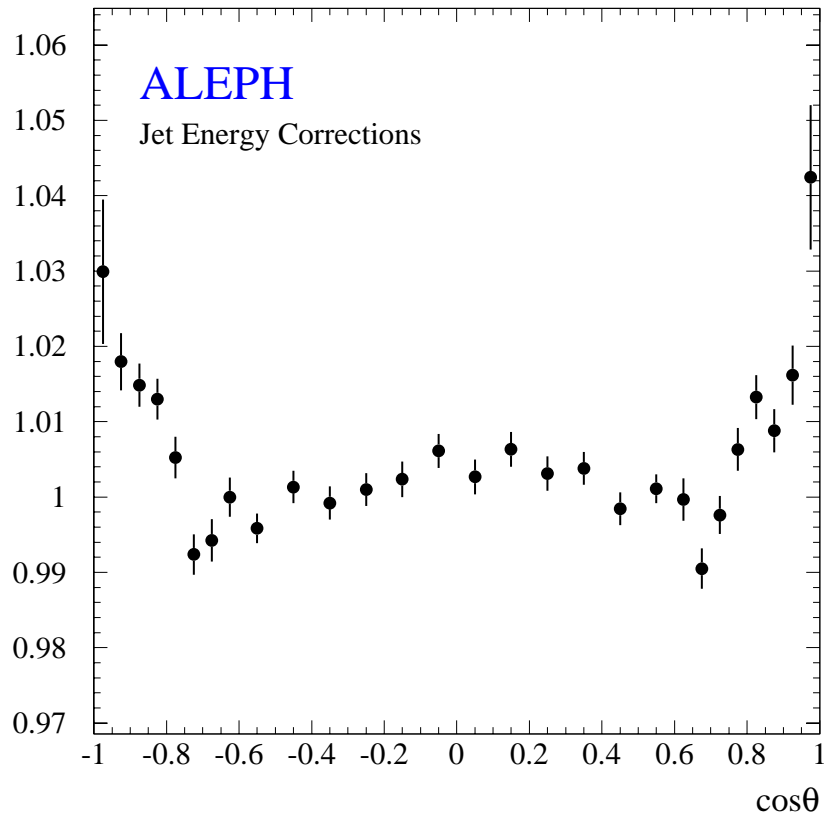


Figure 5.1: The jet energy corrections ( $Ratio = \frac{(E_{jet}/E_{beam})_{data}}{(E_{jet}/E_{beam})_{MC}}$ ) for the year 1998 as a function of the polar angle [19].

## 5.4 Neural Network Selection

After reconstructing the event, the selection of events is further refined using a Neural Network technique. This improves the purity of the sample without reducing too much the selection efficiency. The input to the Neural Net are the following variables <sup>4</sup>, shown in Figure 5.2 for

<sup>4</sup>These variables are, in general, correlated.

the  $e\nu q\bar{q}$  channel and in Figure 5.3 for the  $\mu\nu q\bar{q}$  channel:

- Corrected momentum of the lepton;
- Missing transverse momentum;
- Isolation of the lepton.

The isolation of the lepton is defined as:

$$Iso = \log(\tan(\alpha_{jet})/2) + \log(\tan(\alpha_{ch})/2), \quad (5.6)$$

where  $\alpha_{jet}$  is the angle between the lepton and the closest jet and  $\alpha_{ch}$  is the angle between the lepton and the nearest good charged track (with a momentum greater than 0.2 GeV/c).

Figure 5.4 shows the neural network output for selecting electrons and muons respectively. The separation between the signal Monte Carlo and the background is very good and the Figure 5.4 shows also a very good agreement between data and Monte Carlo events.

In the next chapter, kinematic cuts will be introduced (see section 6.4.1), hence the quality of the selection is only here defined with respect to two quantities: the efficiency ( $\epsilon$ ) to select a true (generated) semi-leptonic event and the purity ( $\rho$ ) of the sample. The quality  $Q$  of the selection is then defined:

$$Q = \sqrt{\epsilon\rho}. \quad (5.7)$$

The cut on the neural network output is chosen such that  $Q$  is maximised. Tables 5.2 and 5.3 give the efficiency and the purity of the selection. It is also clear from this table that the quality of the selection does not change significantly with increasing CM energy. The number of selected and expected events, given in Table 5.1, are obtained applying a cut of 0.6 on the neural network output.

## 5.5 Summary

The selection and the reconstruction of semi-leptonic events have been discussed. After a preselection which rejects events with a different signature than the signal, a selection based on a neural network analysis is performed, leading to a purity above 90 % to select semi-leptonic events with an efficiency at the level of 79.5 % for the  $e\nu q\bar{q}$  channel and 89.5 % for the  $\mu\nu q\bar{q}$  channel.

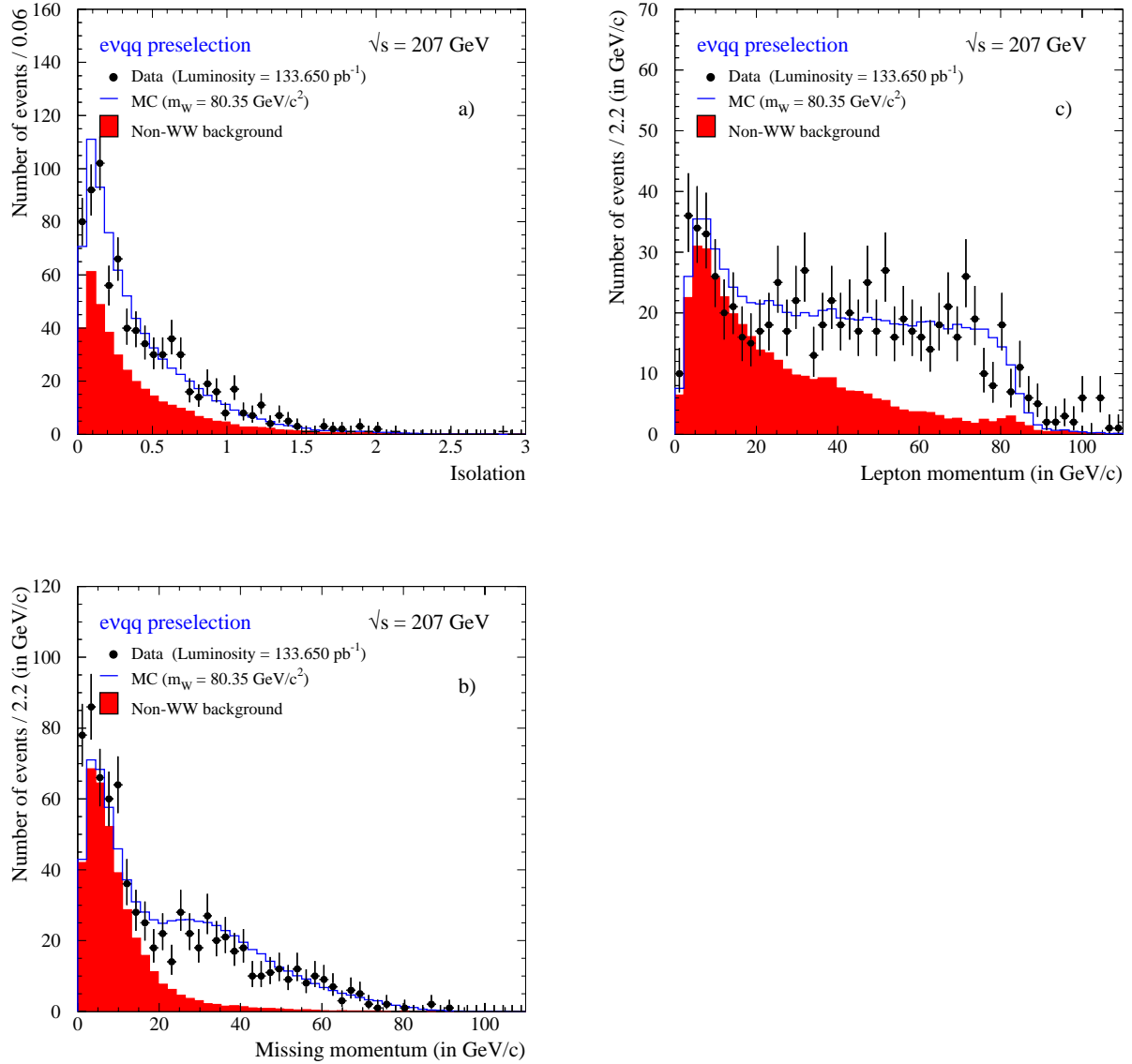


Figure 5.2: Distribution of *c*) the lepton momentum, *b*) the missing momentum and *a*) the isolation of the  $evq\bar{q}$ . These three variables are the input of the neural network.

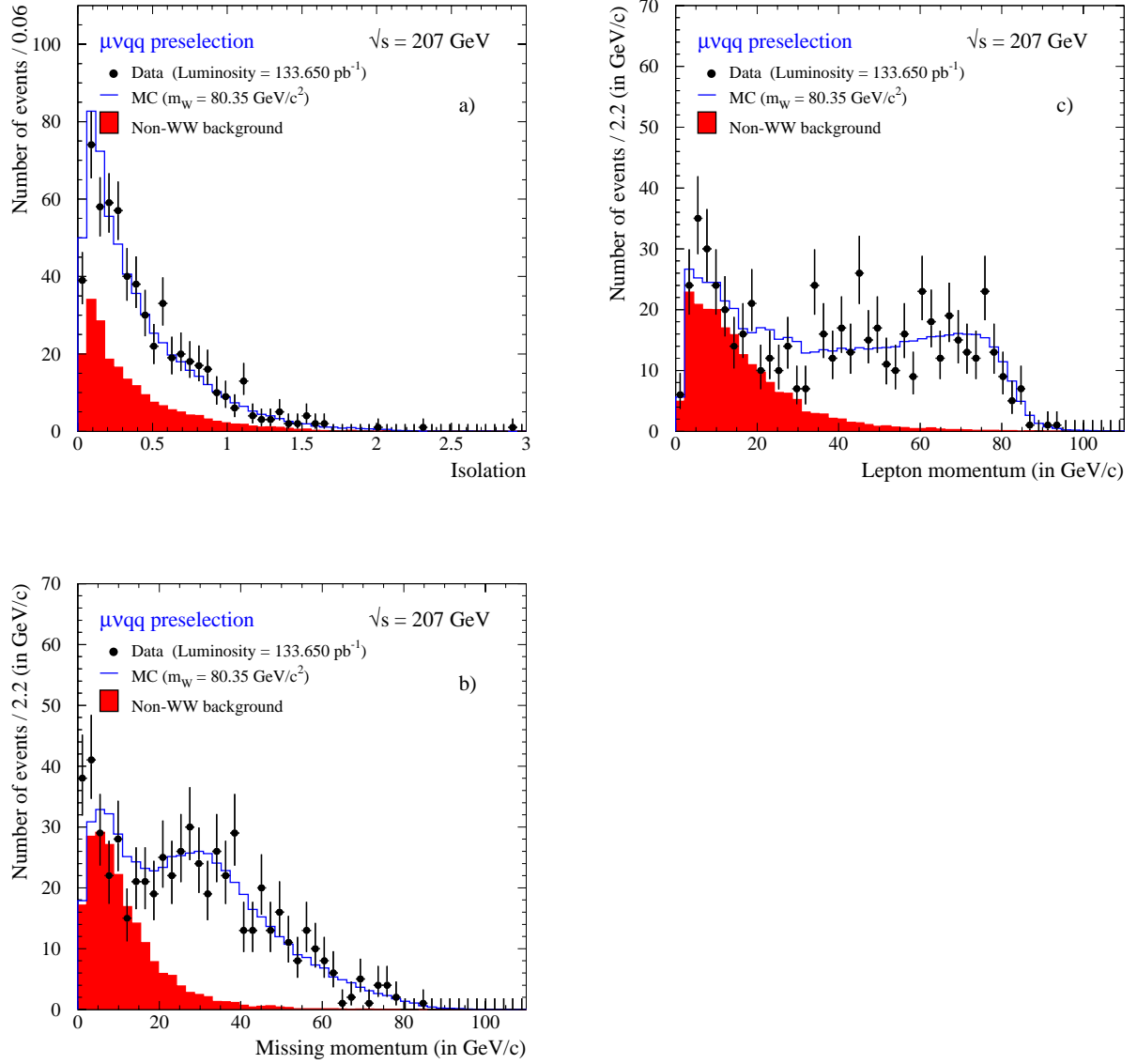


Figure 5.3: *Distribution of c) the lepton momentum, b) the missing momentum and a) the isolation of the  $\mu\nu q\bar{q}$  channel. These three variables are the input of the neural network.*

$e\nu q\bar{q}$							
$\sqrt{s}$ in GeV	188.6	191.6	195.5	199.5	201.6	204.9	206.5
L [in pb <sup>-1</sup> ]	174.2	28.9	79.9	86.3	41.9	81.6	133.
WW $\rightarrow$ 4f	365.6	62.4	176.6	190.9	93.2	182.6	302.7
WW $\rightarrow e\nu q\bar{q}$	352.4	59.8	168.1	182.2	88.7	173.5	287.1
WW $\rightarrow \mu\nu q\bar{q}$	0.1	0.0	0.1	0.1	0.0	0.1	0.1
WW $\rightarrow \tau\nu q\bar{q}$	13.0	2.5	7.9	8.3	4.3	8.5	15.1
WW $\rightarrow q\bar{q}q\bar{q}$	0.0	0.0	0.0	0.0	0.0	0.0	0.0
WW $\rightarrow l\nu l\nu$	0.9	0.1	0.5	0.3	0.2	0.5	0.4
qq( $\gamma$ )	9.3	1.1	4.6	3.9	1.0	4.1	6.3
ZZ	1.3	0.2	0.6	0.8	0.7	0.4	1.5
We $\nu$	2.2	0.5	1.4	1.5	0.8	1.6	3.1
Zee	4.2	0.6	1.6	2.0	0.9	2.6	3.2
$N_{exp}$	383.4	64.8	184.8	199.1	96.6	191.3	316.8
$N_{obs}$	355	63	183	199	109	179	302
$\mu\nu q\bar{q}$							
$\sqrt{s}$ in GeV	188.6	191.6	195.5	199.5	201.6	204.9	206.5
L [in pb <sup>-1</sup> ]	174.2	28.	79.9	86.3	41.9	81.6	133.
WW $\rightarrow$ 4f	393.8	67.7	189.2	209.5	102.4	199.7	327.5
WW $\rightarrow e\nu q\bar{q}$	0.2	0.0	0.1	0.1	0.0	0.1	0.1
WW $\rightarrow \mu\nu q\bar{q}$	372.2	63.6	177.3	195.1	95.0	184.2	302.2
WW $\rightarrow \tau\nu q\bar{q}$	21.4	4.	11.6	14.4	7.2	15.1	24.6
WW $\rightarrow q\bar{q}q\bar{q}$	0.0	0.1	0.0	0.0	0.0	0.0	0.0
WW $\rightarrow l\nu l\nu$	0.0	0.0	0.2	0.3	0.2	0.4	0.8
qq( $\gamma$ )	0.9	0.2	1.2	0.9	0.3	1.1	1.6
ZZ	2.4	0.5	1.5	2.0	2.1	1.9	3.7
We $\nu$	0.1	0.0	0.0	0.0	0.0	0.0	0.1
Zee	0.0	0.0	0.0	0.0	0.0	0.0	0.0
$N_{exp}$	397.1	68.4	191.9	212.8	104.8	202.7	332.9
$N_{obs}$	393	67	175	218	100	198	354

Table 5.1: Summary of the selected data samples and comparison with the Monte Carlo prediction for signal and background.

$\sqrt{s}$	Efficiency	Purity
188.6	81.4 %	91.9 %
191.6	79.4 %	92.3 %
195.5	79.1 %	91.0 %
199.5	78.7 %	91.5 %
201.6	79.3 %	91.8 %
204.9	78.1 %	90.6 %
206.5	78.2 %	90.7 %

Table 5.2: Efficiency and purity of the selection of  $e\nu q\bar{q}$  events.

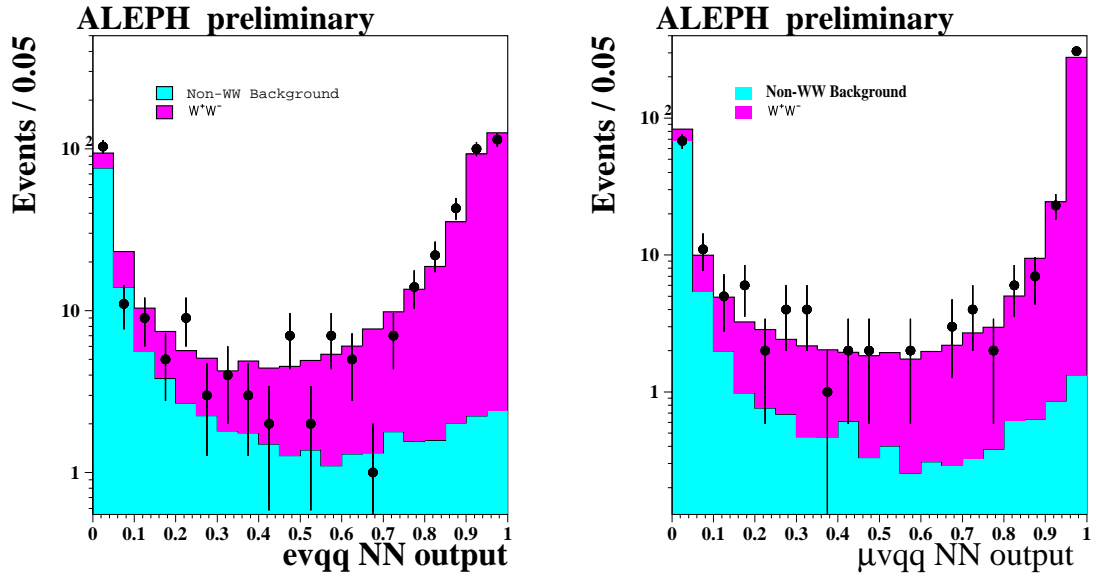


Figure 5.4:  $evq\bar{q}$  and  $\mu\nu q\bar{q}$  Neural Network output for Monte Carlo and data. An event with a probability larger than 0.6 is assumed to be a semi-leptonic event (CM energy of 207 GeV).

$\sqrt{s}$	Efficiency	Purity
188.6	89.7 %	93.7 %
191.6	89.5 %	93.0 %
195.5	89.4 %	92.4 %
199.5	89.5 %	91.7 %
201.6	89.1 %	90.7 %
205	88.5 %	90.8 %
207	89.0 %	90.7 %

Table 5.3: Efficiency and purity of the selection of  $\mu\nu q\bar{q}$  events.

# Chapter 6

## Determination of the $W$ Mass

The  $W$  mass is determined by using the  $W^+W^- \rightarrow q\bar{q}l\nu$  channel, containing two jets, one electron or muon and one neutrino. To improve the invariant mass resolution of the fermion pair forming the  $W$  boson, a kinematic fit is imposed on each event. To extract the  $W$  mass for each data sample, a maximum likelihood fit to the resulting di-fermion invariant mass distribution is then performed.

### 6.1 Concept of Constrained Fit

At LEP, the CM energy  $\sqrt{s}$  is well known. This information is used to improve the resolution of the event. The constraints for four-momentum conservation are:

$$\sum_i^4 E_i = \sqrt{s}, \quad (6.1)$$

$$\sum_i^4 \vec{P}_i = \vec{0}, \quad (6.2)$$

where  $(E_i, \vec{P}_i)$  is the 4-momenta of each fermion  $i$  ( $i = 1, 2, 3, 4$ ). This gives a total of four constraints which may be used in a kinematic fit to improve the measured four momentum  $(E_i^{meas}, \vec{P}_i^{meas})$  for each fermion  $i$ . In this work, the Lagrange multipliers technique is used. The fitted momentum is parametrised in the following way:

$$\vec{P}_i^{fit} = y_i^1 |\vec{P}_i^{meas}| \vec{u}_i^r + y_i^2 \vec{u}_{\theta i} + y_i^3 \vec{u}_{\phi i} \quad (6.3)$$

where  $y_i^1$  is a longitudinal scale of the momentum of measured particles and  $y_i^2$  and  $y_i^3$  are the two transverse components. The fitted energy is scaled with the momentum such that the velocity ( $\beta$ ) is held constant:

$$\frac{|\vec{P}_i^{meas}|}{E_i^{meas}} = \frac{|\vec{P}_i^{fit}|}{E_i^{fit}} = \beta. \quad (6.4)$$

The following  $\chi^2$  is now introduced:

$$S(\mathbf{y}, \vec{\lambda}) \equiv \chi^2 = \chi_{meas}^2 + \chi_{hypothesis}^2, \quad (6.5)$$

which is defined as the sum of two  $\chi^2$ s, one corresponding to the statistical fluctuations of the measurement

$$\chi_{meas}^2(\mathbf{y}) = (\mathbf{y} - \mathbf{y}^0)^T W (\mathbf{y} - \mathbf{y}^0), \quad (6.6)$$

and the other one corresponding to the 4-momentum conservation (i.e the constraints)

$$\chi_{hypothesis}^2 = 2 \sum_{k=1}^{k=m} \lambda_k f_k(\mathbf{a}, \mathbf{y}), \quad (6.7)$$

where  $\lambda_k$  are  $m$  Lagrange multipliers corresponding to  $m$  constraints, the  $f_k$  are the constraint functions. In equation (6.6), the  $\mathbf{y}$  are the fitted values ( $y_1, y_2, y_3$ ) defined in equation (6.3),  $\mathbf{y}^0$  are the measured values of the momentum components, and  $W = V^{-1}$  is the inverse of the covariance matrix for the measured values. The parameter  $\mathbf{a}$  represents a vector of unmeasured parameters, which are here the three momentum components of the neutrino.

### 6.1.1 Momentum Calibration for Detector Acceptance

In order to use as much information as possible, one can use Monte Carlo studies to calibrate, i.e. correct on average, the raw reconstructed momentum according to known acceptance effects of the detector. Such correction factors typically depend on the true momentum and true angles of the particle or jet. In this work, the following notation is used: reconstructed quantities which are corrected for detector acceptance effects using Monte Carlo are called “measured” quantities. Explicitly, the correction (i.e. calibration) factors  $\mathbf{y}^0$  to the reconstructed quantity are defined by:

$$\vec{P}_i^{meas} \equiv \vec{P}_i^{corr} = y_i^{0,1} |\vec{P}_i^{rec}| + y_i^{0,2} \vec{u}_{\theta_i} + y_i^{0,3} \vec{u}_{\phi_i}. \quad (6.8)$$

If no corrections are required, the value of these parameters  $y_i^{0,1}$ ,  $y_i^{0,2}$  and  $y_i^{0,3}$  is 1, 0, 0 respectively. It is very important to note that while these correction parameters account for detector acceptance effects on average, they do not in general satisfy the constraints of 4-momentum conservation—they merely improve the reconstruction of the event on average.

### 6.1.2 Minimisation of the $\chi^2$

Applying the correction parameters  $y_i^{0,1}$ ,  $y_i^{0,2}$  and  $y_i^{0,3}$ , the measured momentum is modified. As derived in appendix A, the minimisation of the  $\chi^2$  is recursive. The massless neutrino is directly reconstructed using three momentum conservation of the event and so three momentum conservation is an implicit characteristic (or hidden quality) of all quantities, including the  $\chi^2$ . As a result, in order to impose overall four momentum conservation, only one explicit constraint is needed in the  $\chi^2$ . The number of parameters in the fit is then 9 (i.e three vectors  $\mathbf{y}^0$ , one for the lepton and one for each jet). The number of free parameters is equal to the number of parameters minus the number of constraints in the fit which is  $9 - 1 = 8$ . Now, the number of degrees of freedom for the fit is just the difference between the number of measured quantities and the number of free parameters which is 1 in this case. In general, for this type of fit, the number of degrees of freedom equals the number of constraints and so we will use the terminology of an  $N$  constrained fit to classify a fit with  $N$  degrees of freedom. In particular, this fit which imposes four momentum conservation with one neutrino in the final state will be called a “1C” fit.

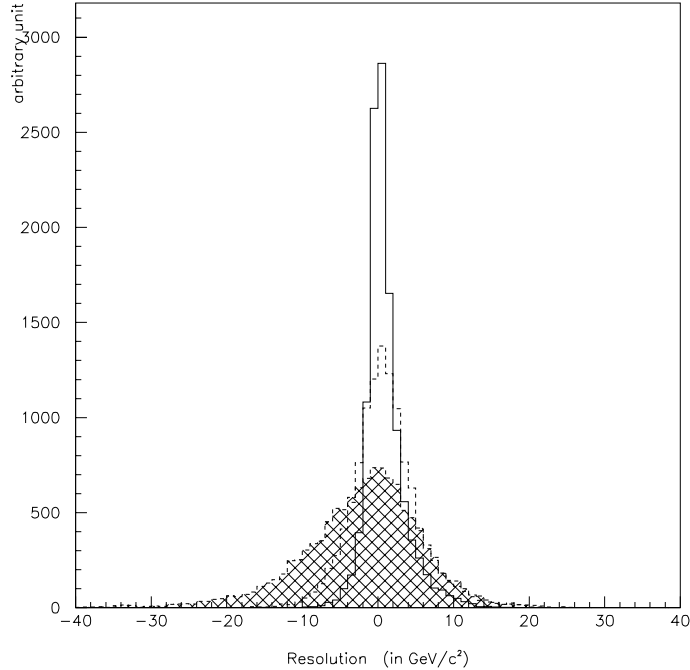


Figure 6.1: *The mass resolution: for measured di-jet (hatched histogram), 1C di-jet mass (dashed line), 2C mass (solid line).*

To further improve the invariant mass resolution, one can use the additional constraint which requires the pair produced W bosons have to have equal <sup>1</sup> masses for a given event. Such a fit is characterised as a “2C” fit and results in a single mass estimator for each event. As a matter of terminology, this event-by-event single mass estimator for the W boson will be called the 2-constrained mass or ”2C” mass. The recursive fit process stops when the  $\chi^2$  converges to a minimum. This means that the  $k$  constraints are satisfied:

$$\sum_k |f_k(\mathbf{a}, \mathbf{y})| < \epsilon. \quad (6.9)$$

for a given  $\epsilon$ .

### 6.1.3 Stability and Performance of the Kinematic Fit

Figure 6.1 shows the effect of the kinematic fit on the resolution which is defined as the difference between the reconstructed (i.e fitted) mass and the true (i.e generated) mass. For the 2C fit, the underlying “generated” quantity is the average of the generated hadronic and leptonic masses. One clearly sees the improvement going from the raw di-jet mass to the 1C hadronic mass and from the 1C hadronic mass to the 2C mass. Table 6.1 gives the improvement in the resolution going from the raw di-jet mass to the 2C mass. Since the 1C leptonic mass and the 1C hadronic mass are obtained using the 4-momentum conservation,

<sup>1</sup>This quantity is not a physical quantity, but a mass estimator, since the  $W$  boson has a finite width. Moreover, no direct comparison with an underlying generated mass is possible.

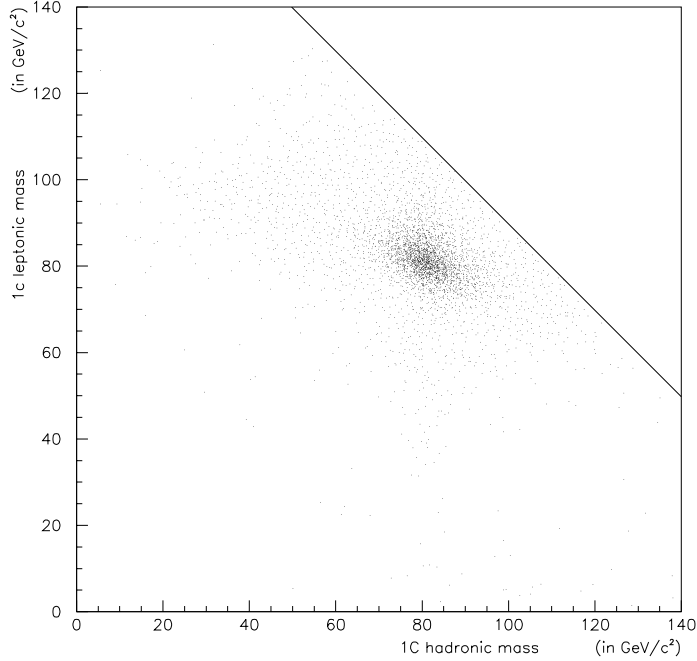


Figure 6.2: *The two-dimensional mass distribution. The line represents the kinematic limit due to energy conservation.*

there should be a negative (anti-correlation) between these quantities. This is illustrated in Figure 6.2. The calculated correlation for each event is shown in Figure 6.3.

Another useful distribution is the probability distribution of a  $\chi^2$ . It is used to estimate the quality of  $\chi^2$  fit. The flatness of the distribution means that the difference between the measured and the fitted parameters is consistent with the value of the error. In other words, this means that the  $\chi^2$  probability describes a true  $\chi^2$  distribution with Gaussian hypothesis. This is in fact observed in Figure 6.4 for large value of the  $P(\chi^2)$  (i.e small value of the  $\chi^2$ ). One clearly sees a large peak at values around zero. This means the fit hypothesis was not correct for these events with a large  $\chi^2$ . Typically, an event with an ISR photon or a background event does not fulfil one of the constraints. In addition, there are events which

-	$W$ mass [in $\text{GeV}/c^2$ ]	
method	mean	R.M.S
reconstruction ( $W \rightarrow q\bar{q}$ )	-2.14	9.44
1 C ( $W \rightarrow q\bar{q}$ )	1.92	7.05
1 C ( $W \rightarrow l\nu$ )	0.06	8.88
2 C ( $WW \rightarrow l\nu q\bar{q}$ )	0.66	4.04

Table 6.1: *Effect of the kinematic fit.*

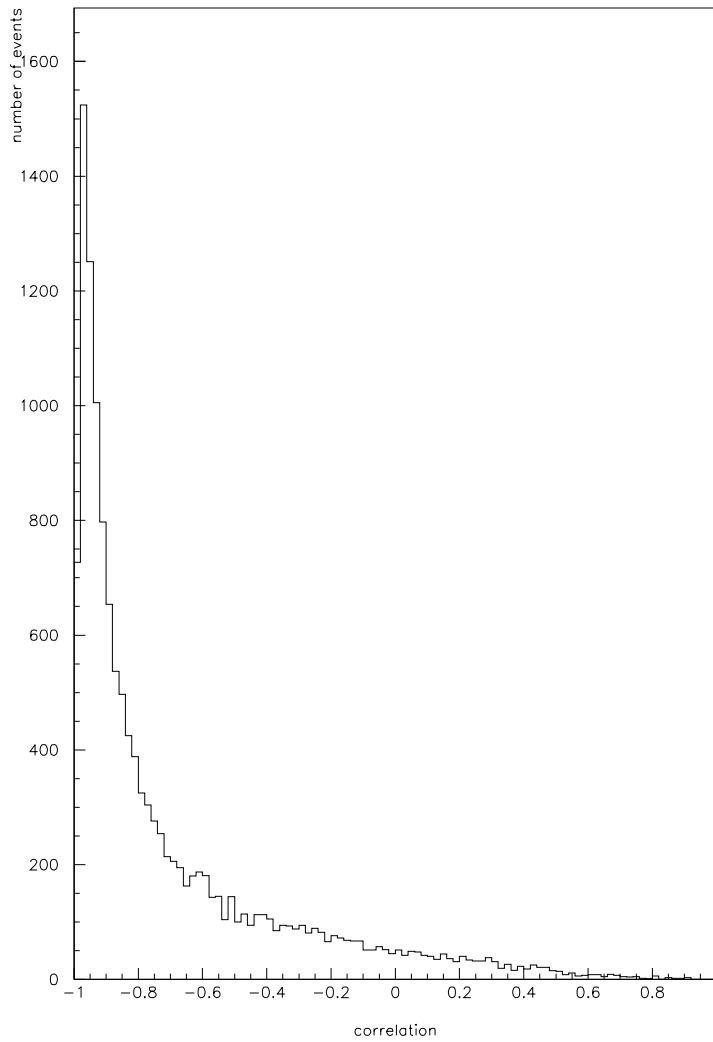


Figure 6.3: *Correlation between the 1C hadronic and leptonic mass distribution.*

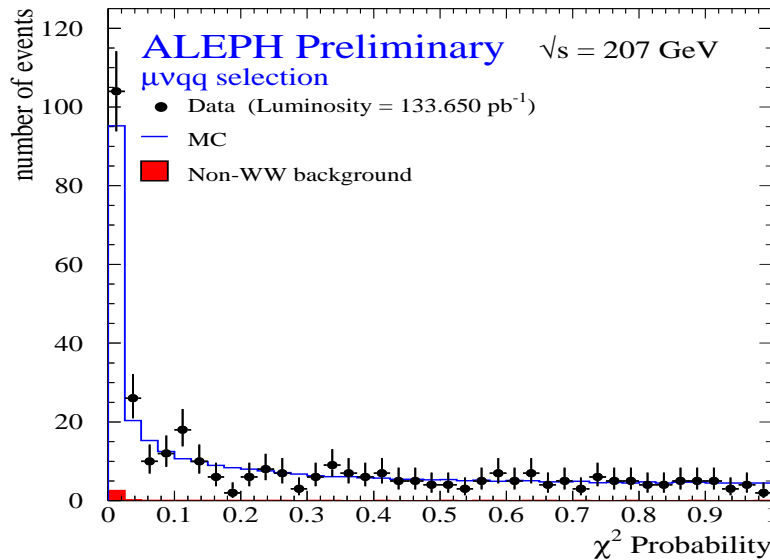


Figure 6.4:  $\chi^2$  Probability of the constrained fit for data and simulated events.

are badly reconstructed<sup>2</sup>. It is worth noting that if the  $\chi^2$  is too large (i.e. the  $\chi^2$  probability is too low), the fit error for the fitted quantity no longer represents a Gaussian one standard deviation uncertainty. Nevertheless, Monte Carlo simulations agree well with the data for both the peak region and the flat region as shown in figure 6.4, and demonstrate that badly reconstructed events are well understood at the Monte Carlo simulation level.

## 6.2 Mass Extraction

In the previous sections the selection of semi-leptonic  $WW$  events has been described and a kinematic fit<sup>3</sup>, which imposes four-momentum conservation, has been introduced. These tools are used to extract the  $W$  mass from the invariant mass spectrum of the selected data. There exist several methods which can be applied for the mass extraction. For example, the  $W$  mass can be obtained by directly fitting a Breit-Wigner function to the data [53]. However, some effects must be accounted for, such as the acceptance of the detector, the initial state radiation (ISR) and the background. The inclusion of these effects, present both in data and in Monte Carlo simulation, distort the Breit-Wigner shape of the reconstructed  $W$  mass distribution. Therefore, a calibration is needed which may introduce systematic effects. A more sophisticated methods must be used. The method, studied in [55], consists of folding a Breit-Wigner with a Gaussian function representing the detector effects. This method has also some drawbacks. Firstly, the detector resolution is not necessarily Gaussian. Secondly, effects such as ISR, Final State Radiation (FSR) and distortions due to detector acceptance cuts are certainly not Gaussian. Therefore, in order to take these distortions into account, one could vary the  $W$  mass in the Monte Carlo simulations. The reconstructed mass distribution, obtained from “real” data, is then compared to the mass distributions from the Monte Carlo simulations. The simulation with the mass distribution closest to that of the

<sup>2</sup>There are non-Gaussian tails in the resolution of the detector.

<sup>3</sup>In fact, two fits are performed: a 1C and a 2C.

data gives then the “measured”  $W$  mass. Clearly, this method has the advantage of taking into account all the distortion effects described above. However, the amount of computer processing time required to produce many Monte Carlo samples is a restricting factor. For this reason, only one large sample of Monte Carlo simulated events is generated at a given reference mass,  $M_W^{ref}$ , which is then “reweighted” to generate an “additional sample” for a different  $W$  mass [56].

### 6.2.1 Reweighting Method and Maximum Likelihood Fit

To accomplish this, each event  $i$  in the reference sample is given a weight, which is determined by the ratio of  $WW$  matrix elements between a new  $W$  mass ( $M_W$ ) and the reference  $W$  mass<sup>4</sup> ( $M_W^{ref}$ ):

$$w_i(M_W, \Gamma_W) = \frac{|\mathcal{M}(M_W \Gamma_W, p_1^i, p_2^i, p_3^i, p_4^i)|^2}{|\mathcal{M}(M_W^{ref} \Gamma_W^{ref}, p_1^i, p_2^i, p_3^i, p_4^i)|^2} \quad (6.10)$$

where  $p_j^i$  ( $j = 1, 2, 3, 4$ ) denotes the four momentum of the outgoing fermion  $j$ . The matrix element (given in reference [24]) has been calculated for the CC03 diagrams.

The probability density function (PDF)  $\Phi$  to observe a particular value for  $M_W$  given a mass estimator  $m$  (from the kinematic fit described above) is written as [56]:

$$\Phi(m_i; M_W) = \frac{\rho_s(M_W) N_s^i(M_W) + \rho_b(M_W) N_b^i}{\Delta m_i N_{TOT}}, \quad (6.11)$$

where  $N_s^i(M_W)$  is the weighted number of signal events in the  $i^{th}$  bin with  $m_i \leq m < m_{i+1}$  and

$$N_s^i(M_W) = \sum_{j=1}^{n_s^i} w_j(M_W), \quad (6.12)$$

$n_s^i$  is the number of signal events from the reference sample found in bin  $i$  and  $N_b^i$  is the total number of background events found in the same  $i^{th}$  bin,  $\rho_s$  is the purity of the selection and  $\rho_b = 1 - \rho_s$  is the fraction of background events. An adaptive binning is incorporated by including a variable bin width  $\Delta m_i$  bin in the PDF ( $\Phi$ ).  $N_{TOT}$  is the total number of reference events:

$$N_{TOT} = \sum_{i=1}^{N_{bin}} \left( \rho_s(M_W) \sum_{j=1}^{n_s^i} w_j(M_W) + \rho_b(M_W) N_b^i \right) \quad (6.13)$$

where  $N_{bin}$  is the number of reconstructed mass bins. The calculated purity depends (slightly) upon the  $W$  mass in the semi-leptonic WW selection. This dependence can be expressed in terms of the cross section  $\sigma_s$ . A parameterisation (parabolic), obtained using the program GENTLE [57], is:

$$\sigma_s(M_W) = \sigma_s(M_W^{ref}) \left( 1 - A(M_W - M_W^{ref}) - B(M_W - M_W^{ref})^2 \right), \quad (6.14)$$

The constants A and B are given in Table 6.2 for every CM energy. This parameterisation is only acceptable if the  $W$  mass is close to the reference  $W$  mass.

<sup>4</sup>The  $W$  width is assumed to vary as a function of the  $W$  mass, see section 2.3.3.

$\sqrt{s}$	A	B
189 GeV	0.003358	-0.002178
192 GeV	0.007098	-0.001406
196 GeV	0.011353	-0.001026
200 GeV	0.014698	-0.000774
202 GeV	0.016179	-0.000652
205 GeV	0.018202	-0.000319
207 GeV	0.019146	-0.000519

Table 6.2: Value of the constants used in the parameterisation as a function of the CM energy.

The purity can then be written as:

$$\rho_s(M_W) = \frac{\epsilon_s \sigma_s(M_W)}{\epsilon_s \sigma_s(M_W) + \epsilon_b \sigma_b} \quad (6.15)$$

where  $\epsilon_s, \epsilon_b$  are the efficiencies of the selection for signal and background, respectively. The best estimate of the  $W$  mass is then that  $M_W$  which maximises the likelihood function:

$$\mathcal{L}(M_W) = \prod_{i=1}^{N_{evt}} \Phi(m_i; M_W) \quad (6.16)$$

where  $N_{evt}$  is the number of selected data events which enter in the maximisation. Numerically, it is more convenient to use the logarithm of the likelihood function:

$$l(M_W) = -2 \log \mathcal{L}(M_W) = -2 \sum_{i=1}^{N_{evt}} \log(\Phi(m_i; M_W)) \quad (6.17)$$

## 6.2.2 Multi-dimensional Reweighting

In the description of the concept of the reweighting method in the previous section, a single mass estimator was used. This method can be generalised to several dimensions for a given set of variable, as it was done in [60]. To achieve this, one introduces  $d$  estimators  $m^1, m^2, m^3, \dots$  spanning a  $d$ -dimensional space with bins in that space designated by  $m_{ijk\dots}$  so that the number of reweighted signal events in bin  $m_{ijk\dots}$  is given by

$$N_s^{ijk\dots} = \sum_{n=1}^{n_s^{ijk\dots}} w_n(M_W), \quad (6.18)$$

similarly to equation (6.12),  $N_s^{ijk\dots}$  being the number of signal events in bin  $ijk$ . Rewriting the PDF (6.11) in the general case, one gets:

$$\Phi(m_{ijk\dots}; M_W) = \frac{\rho_s(M_W) N_s^{ijk\dots}(M_W) + \rho_b(M_W) N_b^{ijk\dots}}{\Delta V_{ijk\dots} N_{TOT}} \quad (6.19)$$

where  $N_b^{ijk\dots}$  is the number of background, in the same  $N_s^{ijk\dots}$  bin. The hyper-volume  $\Delta V_{ijk\dots}$  is the replacement of the bin width  $\Delta m_i$ . Using these additional quantities, one can build

Correlation (in %)	$M_{2C}$	$\Delta M_{2C}$	$M_{1C}^h$	$M_{1C}^l$	$\Delta M_{1C}^h$	$\Delta M_{1C}^l$
$M_{2C}$	100	-	-	-	-	-
$\Delta M_{2C}$	-13	100	-	-	-	-
$M_{1C}^h$	37	-18	100	-	-	-
$M_{1C}^l$	50	10	-39	100	-	-
$\Delta M_{1C}^h$	-5	12	6	9	100	-
$\Delta M_{1C}^l$	9	13	-4	9	35	100

Table 6.3: Correlations between the different  $W$  mass estimators and their errors.

the following multi-variate likelihood function

$$\mathcal{L}(M_W) = \prod_{i=1}^{N_{evt}} \prod_{j=1}^{N_{evt}} \prod_{k=1}^{N_{evt}} \dots \Phi(m_{ijk\dots}; M_W). \quad (6.20)$$

This likelihood provides an unbiased estimator of the  $W$  mass [56]. Moreover, using this construction of the PDF, the correlations between the chosen estimators are automatically taken into account. These estimators are chosen according to their sensitivity to the  $W$  mass.

### 6.2.3 Choice of Estimators

As discussed in section 6.1.2, the 2C mass provides an exceptionally good estimator of the  $W$  mass. Hence, the 2C mass is used as an estimator in the likelihood (see reference [63] for an example of a one dimensional likelihood fit).

In addition to variables directly related to the  $W$  mass (1C hadronic  $W$  mass, 1C leptonic  $W$  mass, 2C mass), the three independent elements of the event-by-event covariance matrix for the two 1C masses as well as the single event-by-event fit error for the 2C mass are considered as other dimensions in a multi-dimensional likelihood fit. One motivation for including the event-by-event kinematic fit errors in the unbinned likelihood is that events are categorised according to their mass error. This allows the PDF to more accurately describe these “groups” of events. The expected exclusive sensitivities for all of the considered estimators are given in Table 6.4. The correlations between the different estimators are given in Table 6.3.

Due to the enormous amount of Monte Carlo statistics required to construct a multi-dimensional reference PDF, we restrict our likelihood to at most three dimensions. Table 6.5 shows that a three-dimensional likelihood fit using the 1C hadronic  $W$  mass, the 2C mass and the fit error of the 2C mass improves the statistical sensitivity to the  $W$  mass by 10% over the one-dimensional likelihood fit which uses only the 2C mass.

It has been shown in [61] and [62] that the lepton energy carries independent information on the  $W$  mass. However, the information comes only from the rapidly changing part near the end-points of the lepton spectrum. In [60], the lepton energy was tested as an estimator. However, obtaining an accurate PDF describing the end-point energy spectrum requires a too large sample of Monte Carlo simulated events.

### 6.2.4 Choice of the binning

Figure 6.5 is a two dimensional projection of the three dimensional binning, where the x-axis is the 2C mass and the y-axis is the 1C hadronic mass. The bins are chosen such that every

estimator	$M_{2C}$	$M_{1C}^h$	$M_{1C}^l$	$M_{2C} \otimes M_{1C}^h$	$M_{1C}^h \otimes M_{1C}^l$
sensitivity (in $\text{MeV}/c^2$ )	$170 \pm 7$	$309 \pm 17$	$368 \pm 21$	$164 \pm 7$	$177 \pm 8$

Table 6.4: *Expected errors for different mass estimators ( $evq\bar{q}$  channel, CM of 189 GeV) .*

bin has the same number of events.

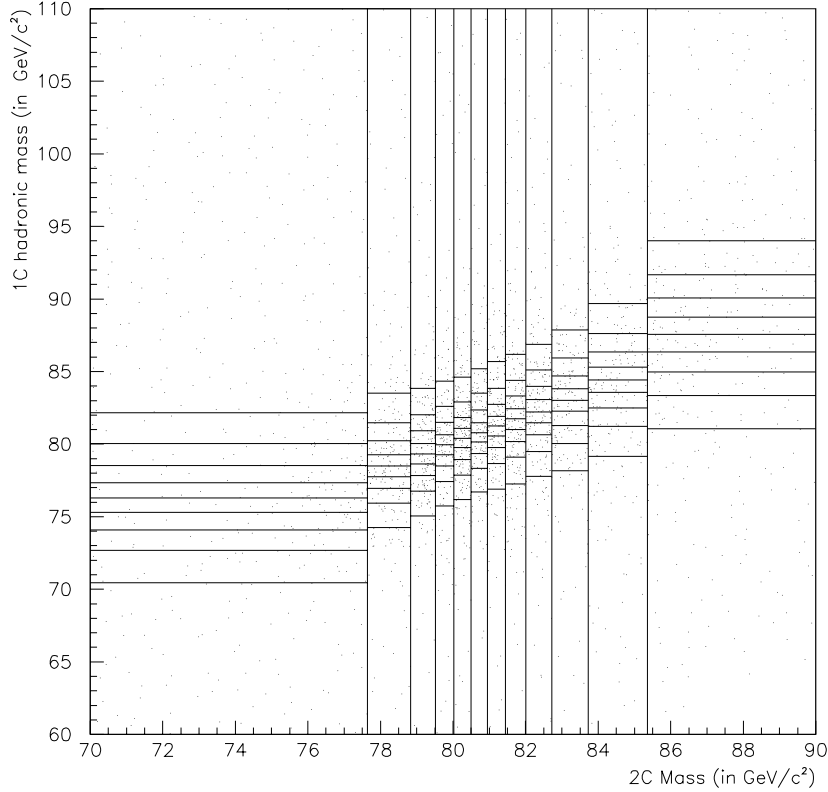


Figure 6.5: *Two dimensional projection of the binning of the 2C mass and the 1C hadronic mass. The dots represent Monte Carlo events used to build the reference. The number of events per bin is required to be greater than 200.*

As discussed in section 6.1.3, the error on the 2C mass has only a statistical meaning if the  $\chi^2$  probability distribution is flat. For low  $\chi^2$  probabilities, the error on the 2C mass is then not reliable and a cut is introduced:

- For  $P(\chi^2) \geq 0.03$ , a 3-dimensional reweighting is used, with the 1C hadronic mass as the second dimension and the error on the 2C mass as the third one:  $M_{2C} \otimes M_{1C}^h \otimes \Delta M_{2C}$ .
- For  $P(\chi^2) < 0.03$ , only the 2C mass is used as estimator.

$E_{CM}$	Channel	Exp. error ( $GeV/c^2$ )
188.6	$e\nu q\bar{q}$	$0.156 \pm 0.007$
188.6	$\mu\nu q\bar{q}$	$0.142 \pm 0.007$
191.6	$e\nu q\bar{q}$	$0.378 \pm 0.035$
191.6	$\mu\nu q\bar{q}$	$0.348 \pm 0.034$
195.6	$e\nu q\bar{q}$	$0.232 \pm 0.015$
195.6	$\mu\nu q\bar{q}$	$0.223 \pm 0.013$
199.6	$e\nu q\bar{q}$	$0.246 \pm 0.017$
199.6	$\mu\nu q\bar{q}$	$0.213 \pm 0.010$
201.6	$e\nu q\bar{q}$	$0.328 \pm 0.027$
201.6	$\mu\nu q\bar{q}$	$0.312 \pm 0.027$
204.5	$e\nu q\bar{q}$	$0.271 \pm 0.015$
204.5	$\mu\nu q\bar{q}$	$0.248 \pm 0.010$
206.5	$e\nu q\bar{q}$	$0.213 \pm 0.013$
206.5	$\mu\nu q\bar{q}$	$0.190 \pm 0.008$

Table 6.5: *Expected statistical error for every CM energy.*

Both PDF's are combined before the minimisation. The standard binning which depends on the Monte Carlo sample, is then:  $12 * 10 * 3$  for the 3-dimensional reweighting and  $20 * 1 * 1$  for the 1-dimensional one. The sizes of the generated Monte Carlo samples (see Appendix B) are chosen such that this requirement is fulfilled. To insure stable results of the fit, the number of events per bin is required to be larger then 200 [59].

## 6.3 Cross Check of the Method

### 6.3.1 Expected Statistical Errors

The expected statistical sensitivity of a given method is usually obtained by performing a fit to several simulated samples, each of which has the size of the data sample. Each simulated sample is subsequently treated like the real “data”. The distribution obtained by histogramming the subsequent measurements provides an indication of the quality of the analysis:

- the mean of the distribution should be compatible with the Monte Carlo generated mass,
- the RMS of the distribution should be compatible with the fit error averaged over all of the samples.

The pull<sup>5</sup> distribution is also checked. A Gaussian fit is performed to the pull distribution and the results are in agreement with a Gaussian hypothesis which is a mean value of zero and a width of one unit. The distributions obtained are shown in Figure 6.6. The numerical results are given in Table 6.5.

<sup>5</sup>The definition of a pull distribution is the difference between the the fitted value of the sample and the input (or generated) value, divided by the error of the fit, since the error of the generated value is neglected.

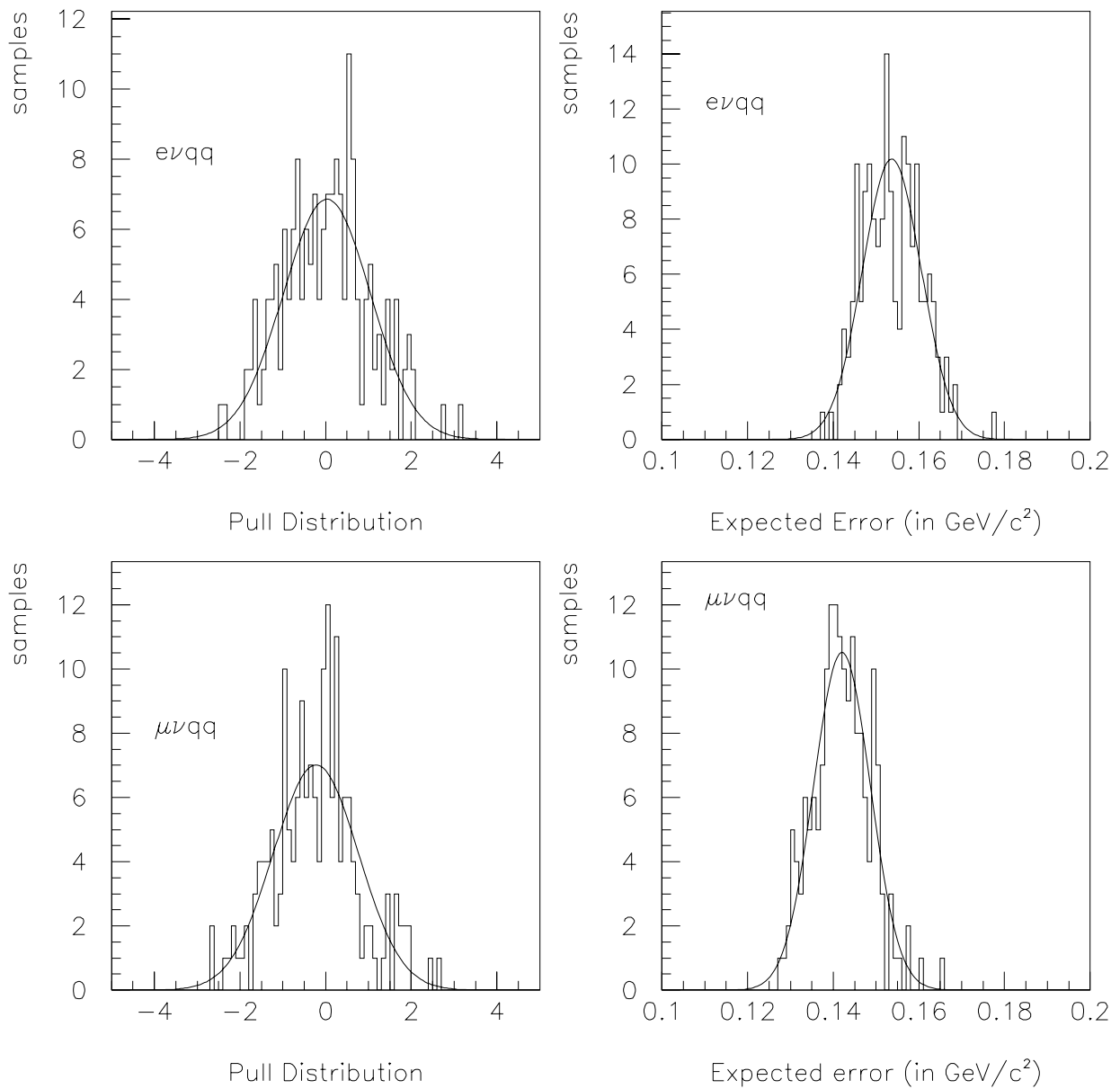


Figure 6.6: Pull distributions and expected statistical errors of  $M_W$  for the electron and muon channels, at  $E_{CM} = 188.6\text{GeV}/c^2$ .

Channel	$\sqrt{s}$	a	b (in GeV/c <sup>2</sup> )
$e\nu q\bar{q}$	188.6	$0.937 \pm 0.027$	$80.348 \pm 0.013$
$\mu\nu q\bar{q}$	188.6	$0.996 \pm 0.019$	$80.37 \pm 0.01$
$e\nu q\bar{q}$	195.6	$0.975 \pm 0.061$	$80.401 \pm 0.025$
$\mu\nu q\bar{q}$	195.6	$0.913 \pm 0.057$	$80.338 \pm 0.023$
$e\nu q\bar{q}$	206.6	$0.927 \pm 0.048$	$80.375 \pm 0.019$
$\mu\nu q\bar{q}$	206.6	$0.998 \pm 0.042$	$80.36 \pm 0.017$

Table 6.6: Numerical value of the slope and offset of the calibration curve. All of them are compatible with an offset equal to the reference mass (no bias) and a unit slope.

### 6.3.2 Linear Behaviour

One of the main reasons for using the reweighting method is that the likelihood is by construction unbiased.

In order to verify this, several samples of Monte Carlo simulated events are generated, each with a different input  $W$  mass, and a linearity cross-check is performed. Background events are added according to the purity of the selection and their cross sections. Figure 6.7 shows six fitted masses as a function of the generated one. A straight line

$$m_{fitted} = a * (M_{true}) + b, \quad (6.21)$$

is then fitted to the points. The dotted line is the result of the fit. For comparison, the ideal line (a unit slope and an offset of 80.35 GeV/c<sup>2</sup>) is also plotted. The value of the slope,  $a$ , and the offset,  $b$ , are given in Table 6.6, in agreement with the expectation.

## 6.4 Data Results

The distribution of the 2C mass is shown in Figure 6.4 for all the data with  $\sqrt{s} > 202$  GeV where the reference  $W$  mass distribution from Monte Carlo simulation is reweighted to the measured  $W$  mass. As explained in section 3.1.1, the data set corresponding to Monte Carlo events generated at 205 GeV CM energy is composed of LEP CM energies between 200 GeV and 206 GeV. For stability reasons, all data which have CM energies between 200 GeV and 203 GeV are discarded as they are too far away from the Monte Carlo generated CM energy of 205 GeV. This corresponds to approximately 2 pb<sup>-1</sup>. The results of the fits to the data taken in 1998, 1999 and 2000 are listed in Table 6.7. All fit errors presented in Table 6.7 are in agreement with the expected statistical errors shown in Table 6.5. The results presented here are obtained from a likelihood fit which uses a PDF constructed from Monte Carlo generated with a fixed  $W$  width. Therefore the 27 MeV/c<sup>2</sup> from equation (2.45) is added to the fitted  $W$  mass.

### 6.4.1 Mass Window

Since an invariant mass is fitted, the results should not depend on a mass window cut. A default mass window is chosen at 189 GeV CM energy, which is: [70., 90.] (in GeV/c<sup>2</sup>) for 2C mass <sup>6</sup>, [60., 110.] (in GeV/c<sup>2</sup>) for the 1C mass and [0., 5.] (in GeV/c<sup>2</sup>) for the error on

<sup>6</sup>The same mass windows are used for the 3-dimensional PDF as well as the 1-dimensional PDF.

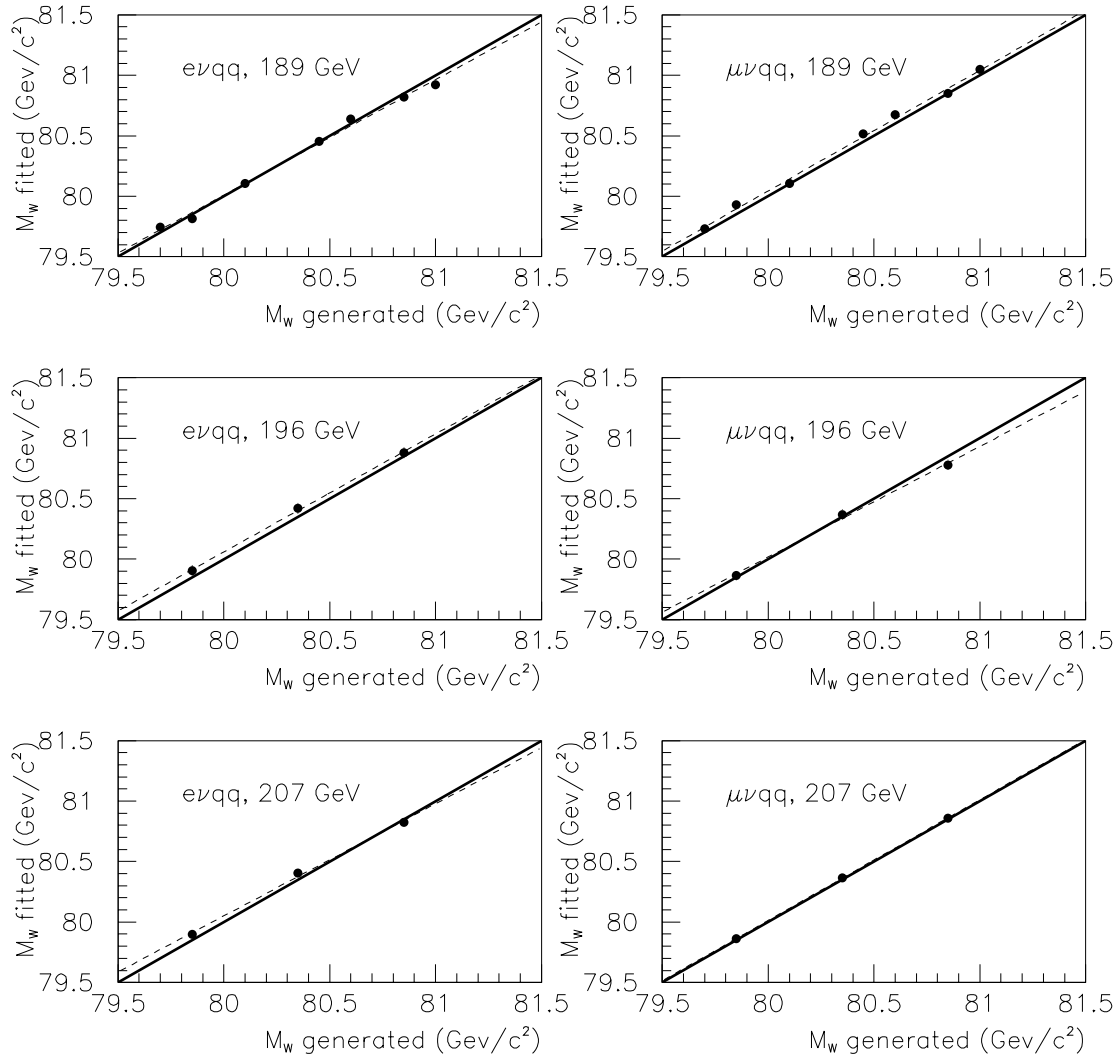


Figure 6.7: The fitted mass,  $M_{fit}$ , as a function of the generated mass. The result of a straight line fit to the point is shown as a dotted line. The solid line correspond to the ideal case, i.e. the fitted mass is equal to the generated one. The values of the slope and the offset are given in Table 6.6. The CM energy is also indicated.

$\sqrt{s}$	$evq\bar{q}$ , in $\text{GeV}/c^2$		$\mu\nu q\bar{q}$ , in $\text{GeV}/c^2$	
	Fitted Mass	Statistical Error	Fitted Mass	Statistical Error
188.6	80.337	0.155	80.278	0.141
191.6	80.980	0.398	80.293	0.350
195.5	80.500	0.240	80.934	0.225
199.5	80.608	0.243	80.129	0.218
201.6	80.403	0.333	80.990	0.317
204.5	80.711	0.267	80.393	0.273
206.5	80.798	0.202	80.219	0.173

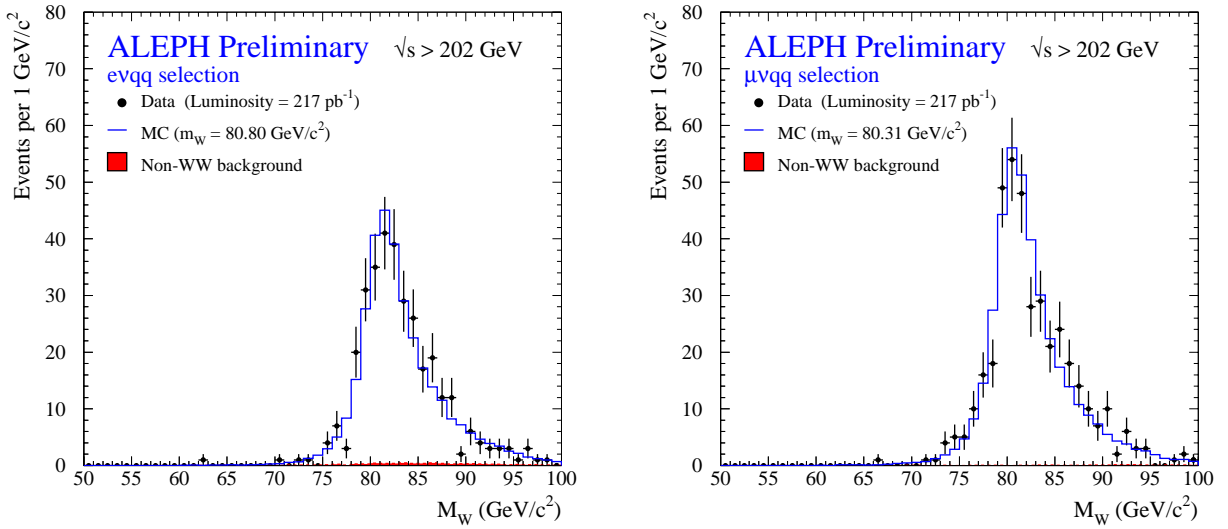
Table 6.7:  $W$  mass measured in the  $evq\bar{q}$  channel and in the  $\mu\nu q\bar{q}$  channel.

Figure 6.8:  $evq\bar{q}$  and  $\mu\nu q\bar{q}$  Invariant Mass Distributions for the data taken in 2000. The histograms represent the Monte Carlo simulation, split into non WW background and signal. The signal Monte Carlo has been weighted to the measured  $W$  mass in the data sample. The dots represent the data.

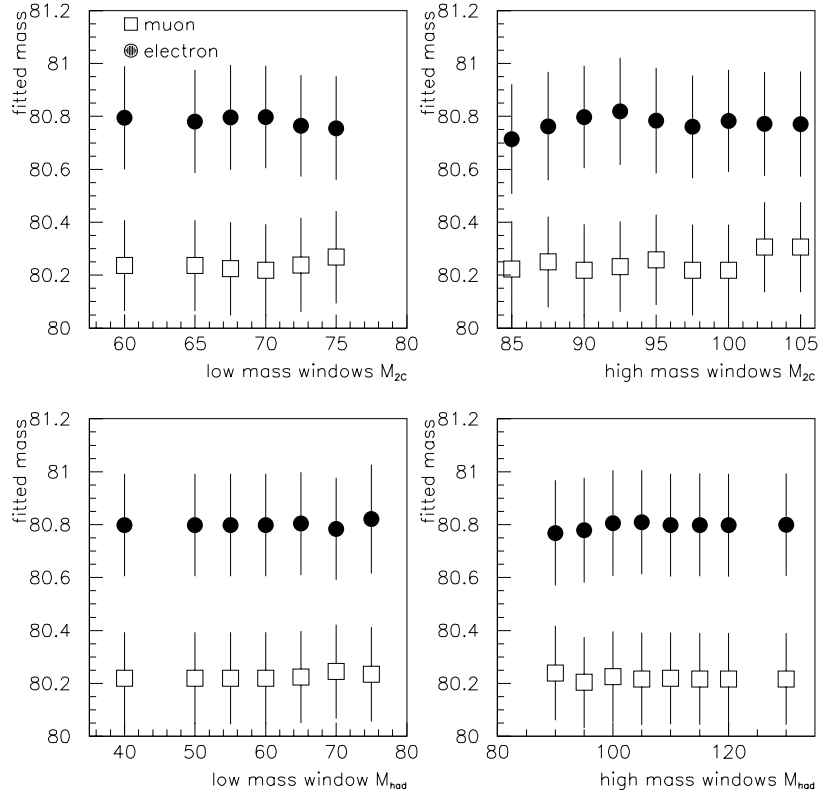


Figure 6.9: *Mass windows study for the 2C mass (upper plot) and for the hadronic mass (lower plot). All the units are in  $\text{GeV}/c^2$ .*

the 2C mass. The upper limit of the mass window of the 2C mass is chosen to be  $90 \text{ GeV}/c^2$  as it allows enough phase space for the kinematic fit to give realistic errors. The lower limit can be seen as a additional cut to remove further background events. Since the  $W$  mass is extracted from an invariant mass distribution, the mass window cuts are kept constant for all CM energies. The  $W$  mass extracted is stable for different mass windows<sup>7</sup>, as shown in Figure 6.9.

<sup>7</sup>This study has been performed for a CM energy of 207 GeV.

# Chapter 7

## Systematic Error

In the previous chapter, we have obtained a statistical error on the  $W$  mass measurement. But several other sources of error, coming from our lack of knowledge of the theory or uncertainties coming from the experimental apparatus need to be carefully investigated. The ALEPH detector is only known to a certain level of precision. The first section of this chapter is dedicated to determine the uncertainties concerning the detector. In addition, a small amount of background events still survives the selection criteria and may cause systematical bias. Hence, the second section is dedicated to estimate the impact of uncertainties in the background contamination. The beam energy is also known to only a finite uncertainty and is particularly important as this uncertainty propagates directly into the  $W$  mass measurement. Furthermore, the multi-dimensional reweighting uses a large sample of Monte Carlo simulated data to construct the reference PDF. As the number of events in each bin is finite, statistical fluctuations limit the accuracy of the PDF. Finally, the last section is devoted to the uncertainty of theoretical calculations used in the Monte Carlo generators.

Table 7.6 summarises the uncertainties from all the considered sources at the end of the chapter.

### 7.1 Detector related Errors

The method used to extract the  $W$  mass relies on a very good agreement between data and Monte Carlo simulation. At different stages of the analysis, Monte Carlo simulations are corrected to compensate any discrepancy between data and Monte Carlo simulation. The source of systematic uncertainty is parametrised in the Monte Carlo simulation and is varied by an estimated one standard deviation from its nominal value. The propagated effect on the  $W$  mass shift is taken as systematic error from this particular source. This is repeated for **all** known sources. If the statistical error on the shift is larger than the uncertainty itself, the statistical error is then quoted as a systematic uncertainty.

#### 7.1.1 Detector Alignment

The alignment of the VDET, ITC and TPC tracking sub-detectors is crucial for the measurement of the track's momentum. After the final alignment of the three tracking detectors, small and residual distortions remain in the tracks. The alignment itself is performed using  $Z^0/\gamma \rightarrow \mu^+\mu^-$  events produced at the  $Z^0$  resonance<sup>1</sup>. Corrections for these distortions are

---

<sup>1</sup>For calibration and alignment purpose, approximately  $3 \text{ pb}^{-1}$  of  $Z^0$  event are taken at the beginning of every data taking period.

modified angle	$\Delta \text{ MeV}/c^2$ (189 GeV)		$\Delta \text{ MeV}/c^2$ (207 GeV)	
	$e\nu q\bar{q}$	$\mu\nu q\bar{q}$	$e\nu q\bar{q}$	$\mu\nu q\bar{q}$
$\theta + 1 \text{ mrad}$	$1.2 \pm 1.5$	$1.2 \pm 2.5$	$1.6 \pm 1.8$	$-1.2 \pm 1.0$
$\theta - 1 \text{ mrad}$	$-1.6 \pm 1.7$	$3.6 \pm 1.4$	$-1.0 \pm 1.6$	$2.8 \pm 1.9$
$\theta$ smeared	$-2.4 \pm 2.8$	$4.4 \pm 1.6$	$0.4 \pm 1.3$	$1.8 \pm 1.0$
$\phi + 1 \text{ mrad}$	$-1.6 \pm 1.5$	$2.0 \pm 2.4$	$0.2 \pm 1.0$	$1.2 \pm 1.5$
$\phi - 1 \text{ mrad}$	$-1.6 \pm 1.0$	$2.8 \pm 1.8$	$-0.2 \pm 1.3$	$2.2 \pm 1.5$
$\phi$ smeared	$1.2 \pm 1.4$	$1.6 \pm 1.8$	$-0.2 \pm 1.1$	$1.2 \pm 1.3$

Table 7.1: Shifts as a result of an artificial bias of 1 mrad. No bias is seen at the level of 1.5 standard deviations.

evaluated by equalising the momentum of the charged track of 45.6 GeV/c in  $Z^0\gamma \rightarrow \mu^+\mu^-$  events. The maximal observed discrepancy is at the level of 2% for  $\cos\theta > 0.9$ . The positive and negative charged tracks are then equalised using the di-muon events. This correction is then systematically applied to all tracks of the data. A conservative systematic error of 10  $\text{MeV}/c^2$  is quoted for both channels, obtained by modifying the Monte Carlo by half of the full correction.

### 7.1.2 Lepton Angle

The measurement depends strongly on the characteristic of the lepton, since it is well measured. Therefore, additional checks are performed on the lepton polar and azimuthal angles. The alignment procedure shows a discrepancy in the angular distribution between data and Monte Carlo simulation at the level of 0.5 mrad [63]. In order to conservatively estimate any systematic uncertainty in the  $W$  mass, an artificial bias is created by adding or subtracting 1 mrad of the polar or the azimuthal angle of the lepton track in Monte Carlo simulated data. A sample of 10 k signal events is used at a CM energy of 189 GeV and a larger sample of 20 k is used at 207 GeV. All the shifts given in Table 7.1 are compatible with no effect at the level of 1.5 standard deviations. The systematic uncertainty from this source is neglected.

### 7.1.3 Radiation in the Final State

Approximately 40% of the  $e\nu q\bar{q}$  events have a bremsstrahlung photon reconstructed in the final state. When a bremsstrahlung photon is emitted close to the electron, a specific algorithm is used [48]. This algorithm consist of a search of energy deposit around the electron track, within a cone of 2.5 degrees. Since the electron and the photon are not really well separated, saturation effects happen, however independent of the angle [27]:

$$E_m/E = 1 - \alpha E, \quad (7.1)$$

where  $\alpha = (7.8 \pm 0.6) \cdot 10^{-4} \text{ GeV}^{-1}$  is the value of the saturation,  $E_m$  is the measured energy and  $E$  the incident one. The uncertainty of the saturation correction is applied to a Monte Carlo sample and the analysis was redone. A shift of 5  $\text{MeV}/c^2$  is observed and quoted as a systematic uncertainty for the  $e\nu q\bar{q}$  channel. The impact of this correction is marginal for the  $\mu\nu q\bar{q}$  channel, since a much smaller fraction of the events emit a bremsstrahlung photon from the muon.

### 7.1.4 Jet Corrections

As described in the section 5.3.2, the jet energy in the Monte Carlo simulation does not reproduce the jet energy in the data. The jet energy of every simulated event is then corrected by a certain amount. The uncertainty of the correction itself is used to estimate the maximal allowed fluctuation. This is then quoted as a systematic uncertainty. The shift is found to be stable as shown in Figure 7.1 where the correction is plotted for different years (1998, 1999 and 2000) [64]. A systematic shift is found at the level of  $4 \text{ MeV}/c^2$  for the  $e\nu q\bar{q}$  channel and  $8 \text{ MeV}/c^2$  for the  $\mu\nu q\bar{q}$  channel.

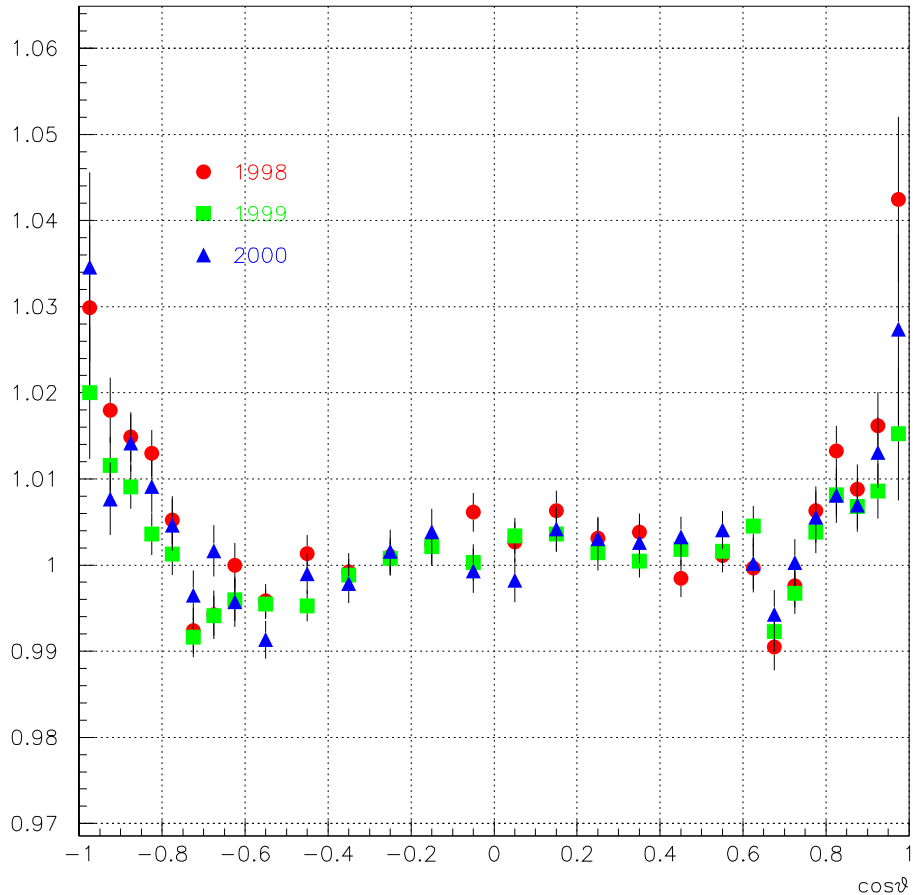


Figure 7.1: Ratio  $(E_{jet}/E_{beam})_{data}/(E_{jet}/E_{beam})_{MC}$  of the jet correction as a function of the polar angle for the 1998, 1999 and 2000  $Z^0$  calibration run.

### 7.1.5 Jet Angular Bias

Another use of the calibration  $Z^0$  data is to evaluate the uncertainty of the jet angular bias. Jets are selected and arranged into two types of particles: photons and charged tracks. This classification is done, since ECAL and tracking chambers are aligned independently. To study the jet angular bias, a variable defined as the difference between the angle of the photonic and the charged part,  $\theta_{\text{photon}} - \theta_{\text{charged}}$  is studied for calibration  $Z^0$  data and Monte Carlo simulation. The difference  $(\theta_{\text{photon}} - \theta_{\text{charged}})_{\text{data}} - (\theta_{\text{photon}} - \theta_{\text{charged}})_{\text{MC}}$  is calculated in bins of the jet polar angle and is represented by the points in Figure 7.2. The function plotted in the same figure is not fitted to the points, but it is a fit to the same difference

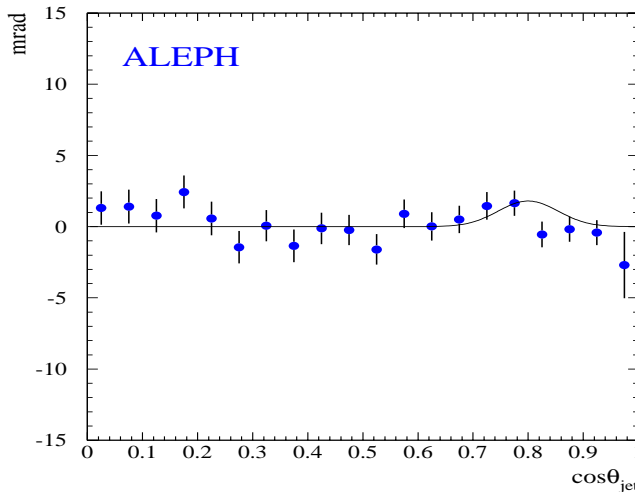


Figure 7.2: Mean difference Data and Monte Carlo simulation: the variable  $\theta_{hadrons} - \theta_{photon}$  as a function of the  $\cos(\theta_{jet})$  of jet of 45 GeV taken at the  $Z^0$  resonance. The full line is a fit to the large  $Z^0$  1994 sample, showing a discrepancy in the overlap region [19].

obtained with a much larger  $Z^0$  data sample (roughly  $62 \text{ pb}^{-1}$ , taken in 1994) to reduce the statistical uncertainty. The maximal difference observed is of the order of 2 mrad in the region where end-cap and barrel overlap. Moreover, other functions have been fitted to the 1994 data distribution. Monte Carlo simulated events are modified by these functions and the  $W$  mass is extracted with these events. The largest shift is found to be  $5 \pm 2 \text{ MeV}/c^2$  for the  $e\nu q\bar{q}$  channel and  $8 \pm 3 \text{ MeV}/c^2$  for the  $\mu\nu q\bar{q}$  at 207 GeV, consistent with the value obtained with the 189 GeV sample,  $6 \pm 3 \text{ MeV}/c^2$  for the  $e\nu q\bar{q}$  channel and  $4 \pm 2 \text{ MeV}/c^2$  for the  $\mu\nu q\bar{q}$  channel respectively. No CM energy dependence is observed.

### 7.1.6 Jet Angular Resolution

The calibration  $Z^0$  sample is then used to measure the angular jet resolution. Since  $Z^0$  are produced at rest in this sample, the jets should be back to back. The resolution is found to be better in the Monte Carlo simulation. To take this difference into account, a smearing of 3.5 mrad [63] is applied on the Monte Carlo simulation at the  $Z^0$  resonance for the polar angle and 2.6 mrad for the  $\phi$  angle. The shift observed for a single angle or both is shown in Table 7.2. The quoted systematic uncertainty is found to be  $7.5 \text{ MeV}/c^2$  for the  $e\nu q\bar{q}$  channel and  $5 \text{ MeV}/c^2$  for the  $\mu\nu q\bar{q}$ .

### 7.1.7 Calorimeter Calibration

In the previous section, the discrepancy between Data and Monte Carlo has been investigated after the full reconstruction of all the events. In addition, one may wish to test the reconstruction itself. The energy content of the jet is tested before the reconstruction. The energy flow algorithm is redone and the jet corrections are recalculated. With this modification, the  $W$  mass measurement is redone to obtain the systematic error. The energy calibration of the calorimeters for the Monte Carlo are obtained using the  $Z^0$  calibration run. In fact,

smeared angle	$\Delta \text{ MeV}/c^2$ (189 GeV)		$\Delta \text{ MeV}/c^2$ (207 GeV)	
	$evq\bar{q}$	$\mu\nu q\bar{q}$	$evq\bar{q}$	$\mu\nu q\bar{q}$
$\phi$	$0. \pm 5.5$	$7.2 \pm 4.3$	$-2.4 \pm 3.5$	$3.2 \pm 2.5$
$\theta$	$1.8 \pm 3.6$	$7.4 \pm 3.0$	$0.4 \pm 3.4$	$4.4 \pm 3.5$
$\theta + \phi$	$4.4 \pm 6.6$	$8.4 \pm 5.6$	$7.4 \pm 4.9$	$5.0 \pm 3.7$

Table 7.2: *Jet angular resolution. The last line is a smearing applied to both angles simultaneously.*

Source	$\Delta M_W$ (in $\text{MeV}/c^2$ )	
	$evq\bar{q}$ channel	$\mu\nu q\bar{q}$
Charged tracking	10	10
Jet energy Correction	4	8
Jet Angular Resolution	10	8
Jet energy Resolution	10	8
Calorimeter Simulation	20	5
Final State Radiation	5	0
Total	27	18

Table 7.3: *Summary of the detector systematic uncertainties.*

this assumes that the energy calibration remains constant during the full data taking period. The energy calibration of the calorimeters are monitored and as a result, the uncertainties of the calibration of the calorimeter ECAL and HCAL energy were assessed to be  $\pm 0.4\%$  and  $\pm 1.5\%$ , respectively [19]. To take both effect into account, the energy deposition for each event is smeared by this uncertainty. A Monte Carlo sample of 100 K WW events at a CM energy of 189 and 200 k WW events at a CM energy of 207 GeV are used to study this effect. The W mass measurement is then redone, and the difference between this modified Monte Carlo and the same Monte Carlo with the standard calibration is quoted as the systematic uncertainty for the calorimetry. The value obtained as 189 GeV and 207 GeV are 5  $\text{MeV}/c^2$  for the  $\mu\nu q\bar{q}$  channel and 20  $\text{MeV}/c^2$  for  $evq\bar{q}$  channel.

### 7.1.8 Summary

All systematic effects discussed so far are listed in Table 7.3 and combined quadratically to obtain a detector systematic uncertainty.

The two large samples of Monte Carlo events (189 GeV and 207 GeV) allow a check for any systematic change in the detector as a function of the CM energy. No significant CM energy dependency is found.

## 7.2 Background

Some background processes still survive the selection criteria. The error from this source is expected to be small, due to the high purity of the selection and the mass cuts. The purity is at the level of 95% for the  $e\nu q\bar{q}$  channel and 99% for the  $\mu\nu q\bar{q}$  channel after the mass window cut. There is a probability that one two-photon interaction survive the selection cuts. The normalisation of the background is modified by  $\pm 30\%$  since the background distribution in the  $e\nu q\bar{q}$  and  $\mu\nu q\bar{q}$  channels is expected to be flat. This variation of the cross section leads to an uncertainty on the  $W$  mass of  $1 \text{ MeV}/c^2$  for the muon channel and  $9 \text{ MeV}/c^2$  for the electron one. Both uncertainties are assumed to be uncorrelated.

## 7.3 Beam energy uncertainty

Every event entering the analysis was constrained to the beam energy. Therefore, the uncertainty of the beam energy has a large impact on the  $W$  mass measurement, especially since this uncertainty is correlated between years and channels. The LEP beam energy is recorded every 15 minutes or more frequently if significant shifts are observed in the Rf frequency of the accelerating cavities. The instantaneous values recorded nearest in time to the selected events are used in this analysis. The beam energy uncertainty is found to be:

- 20 MeV for the data taken in 1998 [66];
- 20 MeV for the data taken in 1999 [67];
- 25 MeV for the data taken in 2000 [68].

To propagate this uncertainty into the measurements, a linear transformation is applied:

$$\frac{\delta M_W}{M_W} = \frac{\delta E}{E}. \quad (7.2)$$

The equation 7.2 is tested by modifying the beam energy before the kinematic fit. As shown in Figure 7.3, the fitted mass depends linearly on the beam energy. As a result, the uncertainty quoted for both channel is  $17 \text{ MeV}/c^2$  for the years 1998 and 1999 and  $21 \text{ MeV}/c^2$  for the year 2000.

## 7.4 Method Related Uncertainty

The finite statistics of the reference sample may introduce a systematic effect in the measurement. The description of the PDF in terms of bins is not perfect and subject to statistical fluctuations. The uncertainty ( $\Delta M_W$ ) can be written as:

$$\frac{1}{(\Delta M_W)^2} = \left( \sum_{i=1}^N (\Delta M_W)_i^2 \right)^{-1}, \quad (7.3)$$

summed over the uncertainty from any particular  $i^{\text{th}}$  (out of  $N$  bins). The cross section of the  $i^{\text{th}}$  bin is defined as  $\sigma_i = N_i/\mathcal{L}$ , where  $N_i$  is the number of selected events and  $\mathcal{L}$  is the integrated luminosity. Rewriting the uncertainty of the  $W$  mass for the  $i^{\text{th}}$  bin, one gets

$$(\Delta M_W)_i = \Delta\sigma_i \left( \frac{\partial\sigma_i}{\partial M_W} \right)^{-1}. \quad (7.4)$$

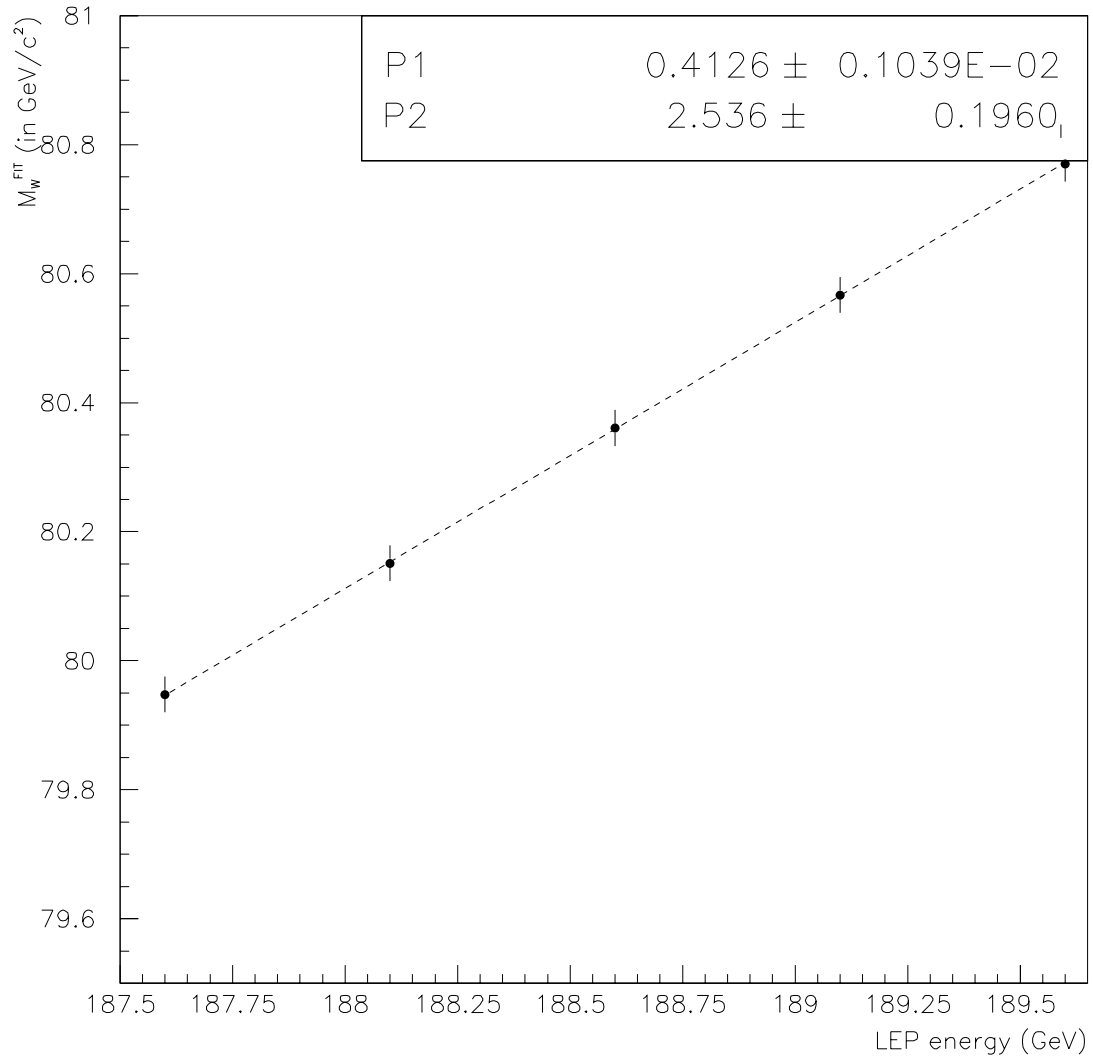


Figure 7.3: *Dependence of the  $W$  mass as a function of the CM energy. This study is performed for the  $e\nu q\bar{q}$  channel at a CM energy of 188.6 GeV. A straight line fit with slope  $P1$  and offset  $P2$  (in  $\text{GeV}/c^2$ ) is also shown.*

Introducing the density of bin  $\rho_i$ , defined as:  $\rho_i = \sigma_i/\sigma_{tot}$ , the gradient of this variable per bin is given by:

$$\frac{\partial \rho_i}{\partial M_W} = \frac{1}{\sigma_{tot}} \frac{\partial \sigma_i}{\partial M_W} = \frac{\mathcal{L}}{N_{tot}} \frac{\partial \sigma_i}{\partial M_W}. \quad (7.5)$$

Assuming that the uncertainty on the cross section  $\sigma_i$  is Poisson-like (i.e  $\Delta\sigma_i = \sqrt{N_i}/\mathcal{L}$ ) and including equation (7.5) in equation (7.3), the uncertainty on the  $(M_W)_i$  is given by:

$$(\Delta M_W)_i = \frac{\sqrt{N_i}}{N_{tot}} \left( \frac{\partial \rho_i}{\partial M_W} \right)^{-1}, \quad (7.6)$$

Hence, one sees that the precision of the reweighting method relies on the statistics of the reference sample. At all CM energies, the reference sample is composed of 1 million (see appendix B) generated 4f events. This method gives an uncertainties of 9 MeV/c<sup>2</sup> for the  $evq\bar{q}$  channel and 9 MeV/c<sup>2</sup> for the  $\mu\nu q\bar{q}$  channel. For the data taken in 2000, the Monte Carlo statistic simulation was produced before the end of the data taking period. The data taken in 2000 present the particularity that the CM energy is between 200 and 209 GeV. Therefore, the uncertainty due to the different CM energy is added to the finite reference and 20 MeV/c<sup>2</sup> is quoted as a systematic error for the finite reference Monte Carlo statistic for the year 2000.

This error describes the “knowledge” of the PDF, so the error is not assumed to be correlated, between year or between channel.

## 7.5 Theoretical Uncertainties

### 7.5.1 Fragmentation Process

As mentioned in chapter 4, the fragmentation is not yet fully understood theoretically. Hence, one must invent fragmentation models (ARIADNE, HERWIG, JETSET). The JETSET package, which uses a string (or LUND) model for the parton shower, is used for this analysis. The parameters used in JETSET to describe the fragmentation model are tuned using hadronically decaying  $Z^0$  events from data collected at the  $Z^0$  resonance. To test this model, two other fragmentation models are used. The fragmentation systematic uncertainty on the W mass is difficult to estimate since the fragmentation effect is folded with the detector resolution and jet clustering. To reduce these effects as much as possible, the same generated partons are fragmented using JETSET, HERWIG and ARIADNE (see section 4.2 for the details of the Monte Carlo simulation). If one replaces JETSET by HERWIG or ARIADNE, one observes a small effect in the W mass (see Table 7.4). The maximal shift observed between any two of the models in the  $evq\bar{q}$  channel is -11.2 MeV/c<sup>2</sup> and -15.2 MeV/c<sup>2</sup> for the  $\mu\nu q\bar{q}$  channel. As there is no reason that the fragmentation uncertainty should differ between the  $evq\bar{q}$  channel and the  $\mu\nu q\bar{q}$  channel, a common systematic uncertainty of 15 MeV/c<sup>2</sup> is quoted. In order to cross check this estimate, a second method comparing variables which are sensitive to fragmentation effects in the data and in the Monte Carlo simulation were studied [19]. The largest observed shift was at the level of 15 MeV/c<sup>2</sup> for both channels, in good agreement with the quoted fragmentation systematic uncertainty.

### 7.5.2 Radiative Corrections

In order to obtain an estimate of the systematic uncertainty due to the incomplete treatment of the radiative corrections, the results of two other generators are also considered. This

-	$e\nu q\bar{q}$ channel	$\mu\nu q\bar{q}$ channel
JETSET - HERWIG	$-11.2 \pm 8.9 \text{ MeV}/c^2$	$-15.2 \pm 9.4 \text{ MeV}/c^2$
JETSET - ARIADNE	$-6.8 \pm 5.8 \text{ MeV}/c^2$	$0.8 \pm 10.5 \text{ MeV}/c^2$
HERWIG - ARIADNE	$-14.0 \pm 12.1 \text{ MeV}/c^2$	$-15.2 \pm 10.4 \text{ MeV}/c^2$

Table 7.4: *difference of the fitted mass for ARIADNE, HERWIG and JETSET. The last line shows the consistency of the result. The maximal shift observed is quoted as a systematic uncertainty.*

-	$\Delta M_{e\nu q\bar{q}}^W$ in $\text{MeV}/c^2$	$\Delta M_{\mu\nu q\bar{q}}^W$ in $\text{MeV}/c^2$
Effect	Pseudo exp.	Pseudo exp.
Standard - ISR	$-7 \pm 3$	$-6 \pm 2$
Standard - Coulomb screening	$11 \pm 2$	$11 \pm 1$
Standard - (ISR + Coulomb screening)	$2 \pm 4$	$4 \pm 3$

Table 7.5: *Effect of the missing radiative correction on the  $W$  mass measurement.*

lack of radiative corrections might cause a significant systematic bias. Firstly, the two other generators, RacoonWW and YFSWW (see section 4.1.1) are compared. Since the generator RacoonWW can have negative weight, this generator can only be used to verify the prediction of YFSWW at truth level. The maximal observed deviation is at the level of  $5 \text{ MeV}/c^2$  in the  $W$  mass [33]. Comparing the generator KORALW and YFSWW and taking into account that KORALW and YFSWW are based on the same principle, one can reweight CC03 events of KORALW by YFSWW. The reference PDF is then calculated three times (there are two main improvements in YFSWW with respect to KORALW):

- with the inclusion of the exact  $O(\alpha)$  electroweak correction,
- with the Coulomb screening approximation,
- with both effects applied.

Pseudo experiments samples are then fitted with these three references and the results are listed in Table 7.5. The effects of the ISR and Coulomb correction [69] in fact compensate, but they are at the level of  $11 \text{ MeV}/c^2$ . However, in the evaluation of the systematic uncertainty, both effects are applied. Therefore the only systematic uncertainty comes from the difference between RacoonWW and YFSWW. The uncertainty quoted is then  $5 \text{ MeV}/c^2$  for all the semi-leptonic channels<sup>2</sup>.

## 7.6 Summary

The systematic uncertainties are summarised in Table 7.6. Since some uncertainties are correlated, the combination will be explained in the next chapter.

<sup>2</sup>The situation is different in the  $4q$  channel. In the  $4q$  channel, a systematic shift of  $5 \text{ MeV}/c^2$  is observed [65].

Source	$e\nu q\bar{q}$	$\mu\nu q\bar{q}$
Detector uncertainty *	27	18
MC Fragmentation*	15	15
Finite reference MC statistics	6	6
Finite reference MC statistics (2000 only)	20	20
Missing Radiative correction*	5	5
Background contamination	9	1
LEP energy (1999 and 1998) *	17	17
LEP energy (2000) *	21	21

Table 7.6: Summary of the systematic errors on  $M_W$ . The errors which are correlated between all the channels (not only the semi-leptonic channel, but also the  $q\bar{q}q\bar{q}$  and  $\tau\nu q\bar{q}$ ) are marked with \*.

# Chapter 8

## Discussion of the Results

The  $W$  mass measured in this thesis will now be combined with other ALEPH measurements. Then the obtained result will be combined with the other LEP experiments. At the end, this  $W$  mass is compared and combined with those from  $p\bar{p}$  collider measurement. The new “preliminary” world average obtained by direct measurement is then used to derive improved limits on the Higgs mass.

### 8.1 $W$ Mass Measurement in the Semi-leptonic Channel

The measurement of the  $W$  mass in the semi-leptonic channel has the advantage of a very clear topology: a high energetic isolated lepton along with a large amount of missing energy. An efficient neural network is developed to select  $WW \rightarrow l\nu q\bar{q}$  events and to exclude other processes. The selected events are reconstructed via a kinematic fit to improve the mass resolution, using Lagrange Multipliers and the well known CM energy. In this thesis, a maximum likelihood fit is performed to extract the  $W$  mass. Moreover, systematic studies are carried out and the  $W$  mass in the semi-leptonic channel is found to be:

$$\begin{aligned} M_W^{evq\bar{q}} &= 80.572 \pm 0.082 \text{ (stat.)} \pm 0.035 \text{ (syst.)} \text{ GeV}/c^2 \\ M_W^{\mu\nu q\bar{q}} &= 80.414 \pm 0.077 \text{ (stat.)} \pm 0.030 \text{ (syst.)} \text{ GeV}/c^2. \end{aligned}$$

These results are consistent<sup>1</sup> with earlier but still preliminary ALEPH results:

$$\begin{aligned} M_W^{evq\bar{q}} &= 80.542 \pm 0.083 \text{ (stat.)} \pm 0.035 \text{ (syst.)} \text{ GeV}/c^2 \\ M_W^{\mu\nu q\bar{q}} &= 80.404 \pm 0.076 \text{ (stat.)} \pm 0.030 \text{ (syst.)} \text{ GeV}/c^2. \end{aligned}$$

The small difference between these two measurements are explained as follows. For the 189 GeV sample, the changes with respect to the previous analysis are due to the fact that firstly the selection is now based on a neural network analysis and secondly the kinematic fit is different. However, the discriminant variables used in the neural network are the same. The method remains unchanged for the data set at highest energy. Moreover, the saturation effect in ECAL (see section 5.2.3 and 7.1.3) was not taken into account in the previous analysis. The effect is larger in the  $evq\bar{q}$  channel since the probability for the electron to emit a bremsstrahlung photon is larger. The difference observed is  $30 \text{ MeV}/c^2$  in the  $evq\bar{q}$  channel and  $10 \text{ MeV}/c^2$  in the  $\mu\nu q\bar{q}$  channel which leads to a change of the measured ALEPH  $W$  mass at the level of  $7 \text{ MeV}/c^2$ .

---

<sup>1</sup>Both measurements are within one standard deviation.

## 8.2 Combination of the W Mass Measurement

### 8.2.1 In ALEPH

The ALEPH results in all channels published for the 2001 Winter conferences [65] are:

$$\begin{aligned}
 M_W^{e\nu q\bar{q}} &= 80.542 \pm 0.083 \text{ (stat.)} \pm 0.035 \text{ (syst.)} \text{ GeV}/c^2, \\
 M_W^{\mu\nu q\bar{q}} &= 80.404 \pm 0.076 \text{ (stat.)} \pm 0.030 \text{ (syst.)} \text{ GeV}/c^2, \\
 M_W^{\tau\nu q\bar{q}} &= 80.370 \pm 0.122 \text{ (stat.)} \pm 0.029 \text{ (syst.)} \text{ GeV}/c^2, \\
 M_W^{qqqq} &= 80.507 \pm 0.054 \text{ (stat.)} \pm 0.026 \text{ (syst.)} \pm 0.037 \text{ (FSI)} \text{ GeV}/c^2.
 \end{aligned}$$

The combined result for the  $W$  mass in the semi-leptonic channel (all LEP II data) is:

$$M_W^{lvqq} = 80.456 \pm 0.051 \text{ (stat.)} \pm 0.032 \text{ (syst.)} \text{ GeV}/c^2.$$

As explained in chapter 7, there exist some correlations on the systematic uncertainties for different channels and/or years, which were carefully taken into account. The fully correlated errors are averaged over years and channels. The semi-leptonic channel has a better sensitivity to the  $W$  mass due to large theoretical uncertainties<sup>2</sup> in the 4q channel. The weight of the semi-leptonic channel in the combination is 73%. Looking at the difference between the fully hadronic and the semi-leptonic channel, a bias due to Final State Interactions (FSI) in the fully hadronic channel might be observed. However, no Final State Interactions are observed in ALEPH at the level of 150 MeV/c<sup>2</sup>:

$$M_W^{qqqq} - M_W^{lvqq} = 51 \pm 75 \text{ (stat. + syst.)} \text{ MeV}/c^2,$$

where the FSI uncertainties are not included. Combining the fully hadronic and the semi-leptonic  $W$  mass measurements, the  $W$  mass obtained in ALEPH from the direct reconstruction, is:

$$M_W = 80.477 \pm 0.038 \text{ (stat.)} \pm 0.023 \text{ (syst.)} \pm 0.015 \text{ (theo.)} \pm 0.017 \text{ (lep)} \text{ GeV}/c^2.$$

Adding the  $W$  mass obtained by the cross section measurement, the  $W$  mass obtained in ALEPH using all LEP II statistics is:

$$M_W = 80.471 \pm 0.038 \text{ (stat.)} \pm 0.023 \text{ (syst.)} \pm 0.015 \text{ (theo.)} \pm 0.017 \text{ (lep)} \text{ GeV}/c^2.$$

The statistical, systematic and theoretical errors are added in quadrature to obtain the total error on the  $W$  mass measurement. The total error of the  $W$  mass in ALEPH is 49 MeV/c<sup>2</sup>. For comparison purposes, the preliminary measurement of the four LEP collaborations are shown in Figure 8.1 and are summarised here:

$$\begin{aligned}
 M_W(\text{ALEPH}) &= 80.471 \pm 0.049 \text{ GeV}/c^2, \\
 M_W(\text{DELPHI}, [71]) &= 80.401 \pm 0.066 \text{ GeV}/c^2, \\
 M_W(\text{L3}, [72]) &= 80.398 \pm 0.069 \text{ GeV}/c^2, \\
 M_W(\text{OPAL}, [73]) &= 80.490 \pm 0.065 \text{ GeV}/c^2.
 \end{aligned}$$

A good agreement is found between the results of the four LEP experiments ( $\chi^2/\text{d.o.f}$  of 32.5 / 39). The combination procedure to compute the LEP value will be described in the next section. The main difference between ALEPH and the three other LEP experiments is that ALEPH is using the three dimensional ‘‘reweighting’’ method, which brings an improvement of 15% with respect to the one dimensional one, used by the other LEP experiments.

<sup>2</sup>The fully hadronic channel is systematically biased by colour reconnection or Bose-Einstein correlation.

### LEP Preliminary results on $M_W$ measurements

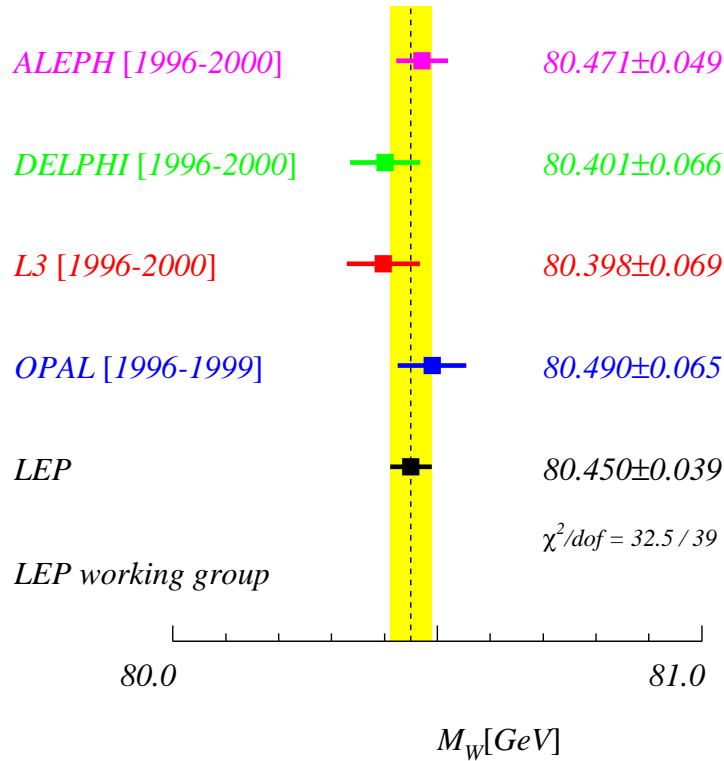


Figure 8.1: The  $W$  mass measured at LEP II from the 4 LEP experiments. The data taking period used to extract  $M_W$  in each experiment is also indicated.

#### 8.2.2 Combination Of All LEP W Mass Measurements

The four LEP experiments provide a more detailed input for the combination as the value given in the previous section. The four LEP experiments provide their results of the direct reconstruction (10 measurements <sup>3</sup> for ALEPH and DELPHI, 8 for OPAL <sup>4</sup> and L3 <sup>5</sup>) for the LEP combination. As explained in chapter 7, the subdivision per year allows a proper treatment of the correlation. Some correlated systematic uncertainties are year dependent, for example the beam energy or part of the detector systematics. Other systematic effects are fully correlated between the experiments, in particular the fragmentation and the Final State Interaction for the  $q\bar{q}q\bar{q}$  channel. For example, studies have shown that the sensitivity of the four LEP experiments on colour reconnection is the same [70]. There is no such study for Bose Einstein correlation, but it is assumed that this uncertainty is model dependent, implying that it is also fully correlated between the LEP experiments. Therefore, a common value for the FSI and the fragmentation uncertainties is taken for the combination of the

<sup>3</sup>An already combined measurement for the non-hadronic channel and a measurement of the hadronic channel per year.

<sup>4</sup>The results of the year 2000 are not yet public.

<sup>5</sup>The results of the year 1996 and 1997 are already combined.

four LEP experiments. In addition to the direct reconstruction of the  $W$  mass, the cross section at threshold for  $W$  pair production measurements<sup>6</sup> of the four LEP experiments has also been taken into account. Therefore a  $\chi^2$  composed of 40 measurements is minimised. The preliminary LEP  $W$  Mass obtained from these measurements is:

$$M_W = 80.450 \pm 0.039 \text{ GeV}/c^2,$$

which includes all LEP published results. As shown in Figure 8.1, the different measurements are in a good agreement with a  $\chi^2/d.o.f$  of 32.5/39.

### 8.2.3 World Average of Direct Measurement

In a  $p\bar{p}$  collider, the measurement of the  $W$  mass is more difficult. Since there are quarks and gluons in the initial state, the energy of the collision and the longitudinal component of the momentum are not known. The only information which can be used is the transverse mass or the transverse energy. In addition, the spectator quarks or gluons have also a none negligible probability to interact. This leads to an unavoidable QCD background and prevents the study of the hadronic decays of the  $W$  boson and  $W \rightarrow \tau\nu$ . The  $W$  mass obtained at the Tevatron is [75]:

$$M_W = 80.454 \pm 0.060 \text{ GeV}/c^2,$$

which is in good agreement with the value obtained by the LEP collaborations. The new preliminary world average  $W$  mass is [75]:

$$M_W = 80.451 \pm 0.033 \text{ GeV}/c^2.$$

## 8.3 Relevance of Precision in $W$ Mass Determination on the Standard Model

Figure 8.2 shows different results of the  $W$  mass measurement. The three first entries in the “table” have been described in the previous section. There are two main issues concerning the  $W$  mass measurement:

- Test of the Standard Model,
- Extract an upper limit on the Higgs mass.

Firstly, one can perform a fit, assuming the Standard Model, to the electroweak data [75] obtained mainly at LEP I, SLD (both operating at the  $Z^0$  resonance), NuTeV and CCFR (both measuring  $\sin\theta_W$  in neutrino-nucleon scattering). This is the fifth value of the  $W$  mass in Figure 8.2 and is equal to:

$$M_W(\text{indirect}) = 80.363 \pm 0.032 \text{ GeV}/c^2.$$

This value is obtained to check the agreement between the Standard Model and the LEP II data set. In this fit, the top mass and the Higgs mass are left as free parameters. The last

---

<sup>6</sup>This measurement has a weight of 2% in the combination, since the only common systematic uncertainty is the beam energy.

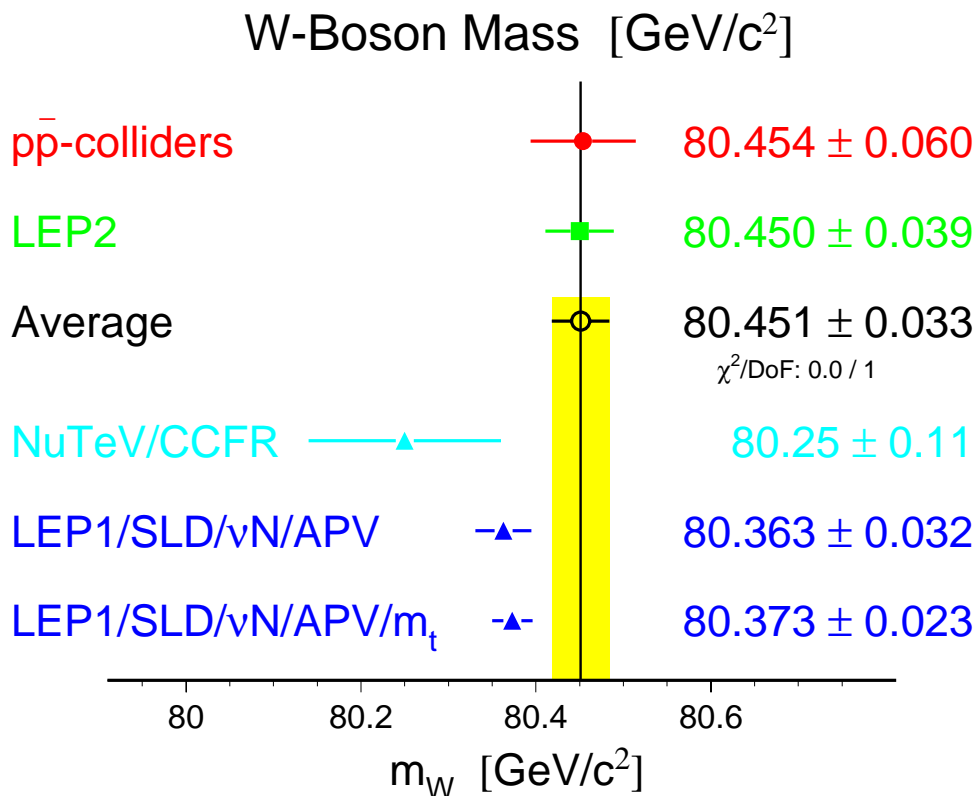


Figure 8.2: The preliminary world average  $W$  mass (summer 2001). The value  $p\bar{p}$ -collider is the combined mass from hadron machine whereas the value LEP2 is the LEP combination. The indirect  $W$  mass measurement is also shown, with and without the top mass as a fixed parameter.

value of Figure 8.2 is obtained by fixing the top mass as well, which leads to a reduction in the error:

$$M_W(\text{indirect} + \text{top}) = 80.373 \pm 0.023 \text{ GeV}/c^2.$$

Before using the top mass in a global electroweak fit, one wants to verify the agreement between the direct and indirect measurements of both the top and the  $W$  masses.

The measured top mass by D0 and CDF at the Tevatron is [75]:

$$M_{\text{top}} = 174.3 \pm 5.1 \text{ GeV}/c^2,$$

and the one obtained by the electroweak (without the measured  $W$  mass) fit is:

$$M_{\text{top}} = 180.3_{-9.2}^{+11.7} \text{ GeV}/c^2,$$

these are in excellent agreement.

Figure 8.3 shows the one standard deviation contours of the direct measurement and the indirect measurement of the top and the  $W$  masses. The Standard Model predictions for Higgs masses between 114 and 1000 GeV/c<sup>2</sup> are also shown. Both data sets prefer a low Higgs mass. The direct searches for the Higgs boson have so far not been successful [74]

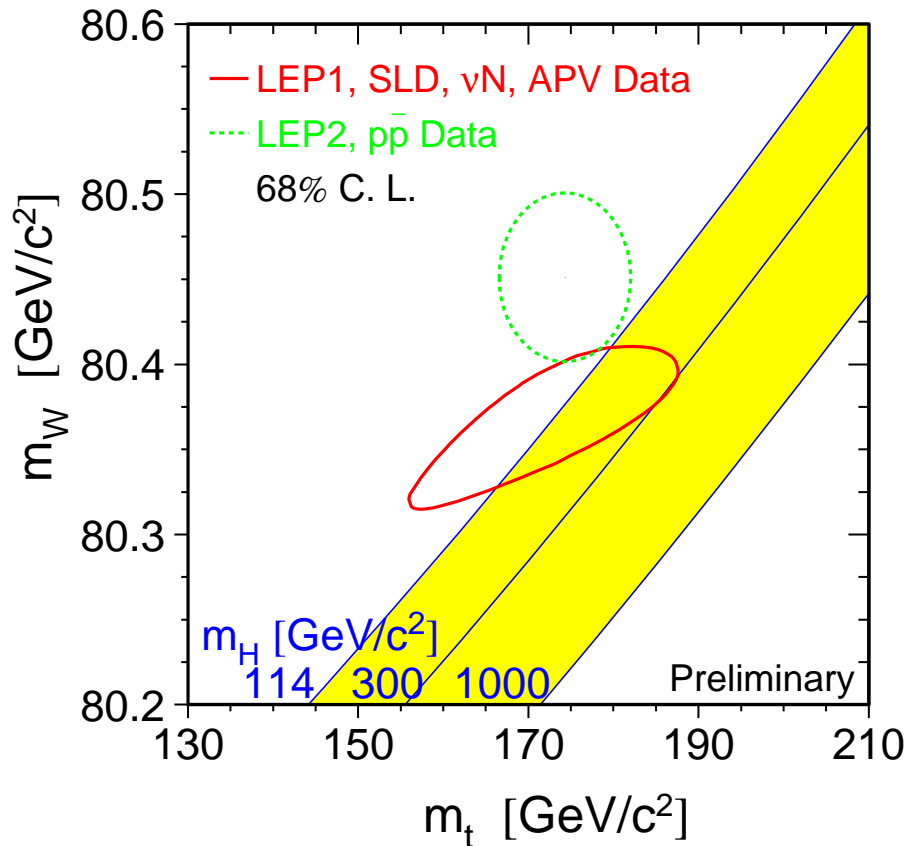


Figure 8.3: *Preliminary comparison between the indirect and direct measurement of the top mass and the  $W$  mass. The straight lines represent the relationship for the  $W$  and top masses as the function of the Higgs mass. The lower bound is the current limit obtained by direct searches.*

and have merely resulted in an exclusion region for the Higgs mass. As we have obtained a  $W$  mass and a top mass by direct and indirect measurements, one can hope to extract an indirect Higgs mass. The curve in Figure 8.4 is the result of the electroweak fit using **all** data. However, a precise value cannot be extracted since the Higgs contribution to the radiative corrections depends logarithmically<sup>7</sup> on the Higgs mass whereas that of the top enters quadratically. Using the parabolic form of the  $\chi^2$ , one can extract a value of the Higgs mass assuming the validity of the Standard Model:

$$M_H = 88_{-35}^{+53} \text{ GeV}/c^2,$$

or in term of limits:

$$M_H < 196 \text{ GeV}/c^2 \text{ at } 95\% \text{ C. L.}$$

<sup>7</sup>This is directly observed in the highly asymmetric error on the Higgs mass.

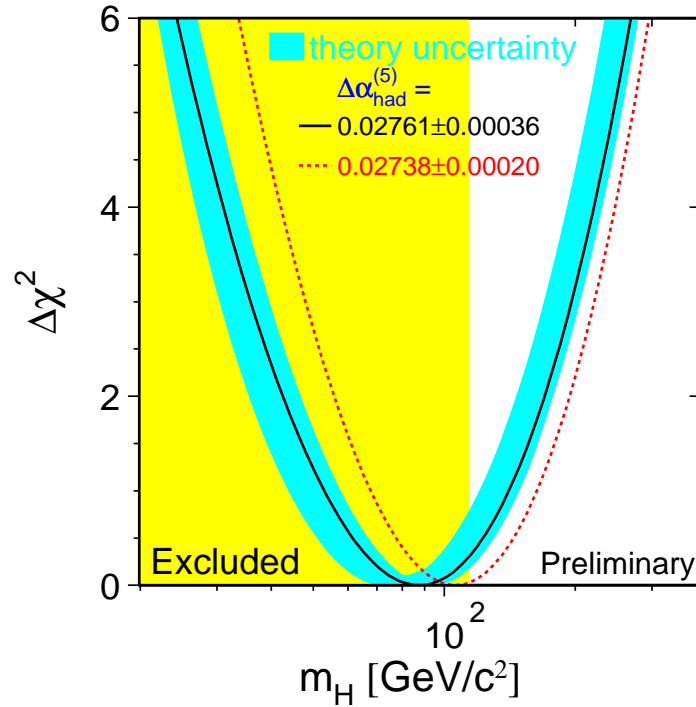


Figure 8.4:  $\Delta\chi^2$  of the global electroweak [75] fit as a function of the Higgs boson mass. The width of the band represents the theoretical uncertainties. The left part of the plot is excluded by direct searches at 95 % Confidence Level. The dash curve is the result obtained using an other evaluation of  $\Delta\alpha_{had}^{(5)}$  which is the contribution of the light quarks to the photon vacuum polarisation ([77] and [78]).

The ALEPH experiment has observed a 3 standard deviations excess in the search for the Standard Model Higgs boson [74] with a mass near  $114 \text{ GeV}/c^2$ , in good agreement with the above limit.



# Appendix A

## Constrained Fit

### A.1 Introduction

The problem is the following: suppose there is a set of  $n$  measurements  $y_i^0, i = 1, 2, \dots, n$  which deviate from their true value. Requiring that these variables fulfil  $m$  constraints  $\mathbf{f}(\mathbf{a}, \mathbf{y}) = 0$  (let  $k = 1, 2, \dots, m$  be the coordinate of the vector  $\mathbf{f}$ ) (for example, energy and momentum conservation). In the general case (for a detailed treatment of the mathematics, see reference [52]), we introduce a model which depends upon  $p$  parameters  $a_j, j = 1, 2, \dots, p$  which are unmeasured. Using the least squares method, the quadratic sum (also called the multi-variate  $\chi^2$  bilinear form)

$$\mathcal{S}(\mathbf{y}) = (\mathbf{y} - \mathbf{y}^0)^T W (\mathbf{y} - \mathbf{y}^0) \quad (\text{A.1})$$

has to be minimised, where

- $\mathbf{y}$  are the fitted values
- $\mathbf{y}^0$  are the measured values
- $W = V^{-1}$  is the inverse of the covariance matrix for the measured values

For convenience, the difference  $\mathbf{y} - \mathbf{y}^0$  ( $\mathbf{a} - \mathbf{a}^0$ ) will be written as  $\Delta\mathbf{y} = (\mathbf{y} - \mathbf{y}^0)$  ( $\Delta\mathbf{a} = (\mathbf{a} - \mathbf{a}^0)$ ).

In order to impose the constraints, we will introduce  $m$  parameters  $\lambda_k$ , known as Lagrange multipliers, one for each constraint. We define a new function:

$$\mathcal{L}(\mathbf{y}, \vec{\lambda}) = \mathcal{S}(\mathbf{y}) + 2 \sum_{k=1}^{k=m} \lambda_k f_k(\mathbf{a}, \mathbf{y}) \quad (\text{A.2})$$

where the number of degrees of freedom is given by the number  $m$  of Lagrange multipliers. Since both  $\mathcal{S}(\mathbf{y})$  and the constraint term are positive definite, the condition for a minimum of this function with respect to all the parameters  $\mathbf{y}$  and  $\lambda_k$  is equivalent to the condition for a minimum of  $\mathcal{S}(\mathbf{y})$  with  $f_k(\mathbf{a}, \mathbf{y}) = 0$ . If the constraints are linear, one can find the solution in one step. If not, the constraints are linearised with a first-order Taylor expansion and the solution can be found by an iterative process with a linear approximation [52].

The starting value for  $\mathbf{y}$  is taken to be the measured  $\mathbf{y}^0$  and the starting value for the unmeasured parameters  $\mathbf{a}$  is set to  $\mathbf{a}^0$  where  $\mathbf{a}^0$  is taken from the simulation. In general, the starting value does not satisfy the constraints.



## A.2 Without the Unmeasured Parameters

In this case, no unmeasured parameters are assumed so that the constraints are applied only on measured variables. Then equation (A.8) becomes

$$\begin{aligned} W\Delta\mathbf{y} + B^T\lambda &= 0 \\ B\Delta\mathbf{y} &= c \end{aligned} \quad (\text{A.9})$$

The solution is found by multiplying the first equation by  $W^{-1}$  from the left:

$$\Delta\mathbf{y} = -W^{-1}B^T\lambda \quad (\text{A.10})$$

by replacing  $\Delta\mathbf{y}$  in second equation of (A.9), we get:

$$\lambda = -W_B c \quad (\text{A.11})$$

with  $W_B = (BW^{-1}B^T)^{-1}$ . Including equation (A.11) in equation (A.10) we obtain

$$\Delta\mathbf{y} = W^{-1}B^TW_B c. \quad (\text{A.12})$$

this is the first step of a recursion for the non-linear problem. The next step consists of setting  $\Delta\mathbf{y}^* = \Delta\mathbf{y}$  so that the constraints are explicitly fulfilled. Applying this, the new value  $\mathbf{y}^{l+1} = \mathbf{y}^0 + \Delta\mathbf{y}$ , where  $\Delta\mathbf{y}$  is the previous calculated correction, is taken as the solution. Using  $c = B(\mathbf{y}^l - \mathbf{y}^0) - f^*$  and  $W^{-1} = V$  we can rewrite equation (A.12) and obtain the recursive formulae<sup>1</sup>:

$$\mathbf{y}^{l+1} = \mathbf{y}^0 + VB^TW_B \left( B(\mathbf{y}^l - \mathbf{y}^0) - \mathbf{f}(\mathbf{y}^l) \right) \quad (\text{A.13})$$

## A.3 General Case

We now want to treat the possibility of unmeasured parameters  $\mathbf{a}$ . We follow the same idea as in the previous section. The system of equations (A.8) is written in matrix notation:

$$\begin{pmatrix} W & 0 & B^T \\ 0 & 0 & A^T \\ B & A & 0 \end{pmatrix} \begin{pmatrix} \Delta\mathbf{y} \\ \Delta\mathbf{a} \\ \lambda \end{pmatrix} = \begin{pmatrix} 0 \\ 0 \\ c \end{pmatrix} \quad (\text{A.14})$$

The inverse of the matrix is:

$$\begin{pmatrix} W & 0 & B^T \\ 0 & 0 & A^T \\ B & A & 0 \end{pmatrix}^{-1} = \begin{pmatrix} C_{11} & C_{21}^T & C_{31}^T \\ C_{21} & C_{22} & C_{32}^T \\ C_{31} & C_{32} & C_{33} \end{pmatrix} \quad (\text{A.15})$$

with the following component (with  $W_A = A^TW_BA$ ):

$$\begin{aligned} C_{11} &= W^{-1} - W^{-1}B^TW_BBW^{-1} + W^{-1}B^TW_BAW_A^{-1}A^TW_BBW^{-1} \\ C_{21} &= W_A^{-1}A^TW_BBW^{-1} \\ C_{22} &= W_A^{-1} \\ C_{31} &= W_BBW^{-1} - W_BAW_A^{-1}A^TW_BBW^{-1} \\ C_{32} &= W_BAW_A^{-1} \\ C_{33} &= -W_B + W_BAW_A^{-1}A^TW_B \end{aligned}$$

<sup>1</sup>For example, this is used for the 4 jet events [74] where all four fermions in the event are measured.

The correction factor  $\Delta \mathbf{y}$ ,  $\Delta \mathbf{a}$  and the Lagrange multiplier  $\lambda$  are given by the following set of equation:

$$\begin{aligned} \Delta \mathbf{y} &= C_{31}^T c = (W^{-1} B^T W_B - W^{-1} B^T W_B A W_A^{-1} A^T W_B) c \\ \Delta \mathbf{a} &= C_{32}^T c = W_A^{-1} A^T W_B c \\ \lambda &= C_{31}^T c = (-W_B + W_B A W_A^{-1} A^T W_B) c \end{aligned}$$

The recursion formulae are given by:

$$\mathbf{y}^{l+1} = \mathbf{y}^0 + V B^T W_B (1 - A W_A^{-1} A^T W_B) \left( B(\mathbf{y}^l - \mathbf{y}^0) - \mathbf{f}(\mathbf{a}^l, \mathbf{y}^l) \right) \quad (\text{A.16})$$

Given a numerical accuracy  $\epsilon$ , the condition for convergence is:

$$\sum_k |f_k(\mathbf{a} + \Delta \mathbf{a}, \mathbf{y} + \Delta \mathbf{y})| < \epsilon. \quad (\text{A.17})$$

# Appendix B

## Monte Carlo Statistics

This Appendix lists in detail all the Monte Carlo statistic used for the analysis (there is one million event of W-pair generated per centre of mass energy), classified by centre-of-mass energy. When background events are not available for one energy, the closest set in energy is then used.

<b>Monte Carlo generated with a CM energy of 188.6 GeV</b>		
Type	Generated number	Cross section (in pb <sup>-1</sup> )
$e^+e^- \rightarrow W^+W^-$	1000 k	16.932
$e^+e^- \rightarrow q\bar{q}(\gamma)$	725 k	99.
$e^+e^- \rightarrow ZZ$	90 k	2.874
$e^+e^- \rightarrow We\bar{\nu}$	15 k	0.8351
$e^+e^- \rightarrow Ze^+e^-$	1957 k	99.11
$e^+e^- \rightarrow e^+e^-\gamma$	600 k	970
$e^+e^- \rightarrow \mu^+\mu^-\gamma$	150 k	8.3
$e^+e^- \rightarrow \tau^+\tau^-\gamma$	150 k	8.3

<b>Monte Carlo generated with a CM energy of 191.6 GeV</b>		
Type	Generated number	Cross section (in pb)
$e^+e^- \rightarrow W^+W^-$	1000 k	17.265
$e^+e^- \rightarrow q\bar{q}(\gamma)$	600 k	96.379

<b>Monte Carlo generated with a CM energy of 195.5 GeV</b>		
Type	Generated number	Cross section (in pb <sup>-1</sup> )
$e^+e^- \rightarrow W^+W^-$	600 k	17.621
$e^+e^- \rightarrow q\bar{q}(\gamma)$	600 k	90.632
$e^+e^- \rightarrow ZZ$	50 k	2.855
$e^+e^- \rightarrow Z\nu\nu$	20 k	0.015
$e^+e^- \rightarrow Ze^+e^-$	100 k	6.997
$e^+e^- \rightarrow We\bar{\nu}$	20 k	0.75
$e^+e^- \rightarrow e^+e^-\gamma$	15000 k	894.49
$e^+e^- \rightarrow t^+t^-\gamma$	50 k	7.54

<b>Monte Carlo generated with a CM energy of 199.5 GeV</b>		
Type	Generated number	Cross section (in pb <sup>-1</sup> )
$e^+e^- \rightarrow W^+W^-$	1000 k	17.812
$e^+e^- \rightarrow q\bar{q}(\gamma)$	1000 k	86.572
$e^+e^- \rightarrow ZZ$	50 k	2.847
$e^+e^- \rightarrow Z\nu\nu$	20 k	0.016
$e^+e^- \rightarrow Ze^+e^-$	100 k	7.072
$e^+e^- \rightarrow We\bar{\nu}$	20 k	0.811
$e^+e^- \rightarrow e^+e^-\gamma$	400 k	859.030
$e^+e^- \rightarrow t^+t^-\gamma$	30 k	7.223

<b>Monte Carlo generated with a CM energy of 201.6 GeV</b>		
Type	Generated number	Cross section (in pb <sup>-1</sup> )
$e^+e^- \rightarrow W^+W^-$	100 k	17.902
$e^+e^- \rightarrow q\bar{q}(\gamma)$	500 k	84.53
$e^+e^- \rightarrow ZZ$	100 k	2.847
$e^+e^- \rightarrow Z\nu\nu$	20 k	0.016
$e^+e^- \rightarrow We\bar{\nu}$	20 k	0.835
$e^+e^- \rightarrow Ze^+e^-$	100 k	98.948
$e^+e^- \rightarrow e^+e^-\gamma$	400 k	842.980
$e^+e^- \rightarrow t^+t^-\gamma$	50 k	7.043

<b>Monte Carlo generated with a CM energy of 205 GeV</b>		
Type	Generated number	Cross section (in pb <sup>-1</sup> )
$e^+e^- \rightarrow W^+W^-$	1000 k	17.976
$e^+e^- \rightarrow q\bar{q}(\gamma)$	1000 k	84.53
$e^+e^- \rightarrow ZZ$	50 k	2.83
$e^+e^- \rightarrow We\bar{\nu}$	20 k	0.866
$e^+e^- \rightarrow Ze^+e^-$	1800 k	98.948
$e^+e^- \rightarrow e^+e^-\gamma$	1000 k	818.630
$e^+e^- \rightarrow \tau^+\tau^-\gamma$	100 k	6.824

<b>Monte Carlo generated with a CM energy of 207 GeV</b>		
Type	Generated number	Cross section (in pb <sup>-1</sup> )
$e^+e^- \rightarrow W^+W^-$	1000 k	18.00
$e^+e^- \rightarrow q\bar{q}(\gamma)$	1000 k	84.53
$e^+e^- \rightarrow ZZ$	50 k	2.81
$e^+e^- \rightarrow We\bar{\nu}$	20 k	0.8845
$e^+e^- \rightarrow Ze^+e^-$	100 k	7.18
$e^+e^- \rightarrow Z\nu\nu$	20 k	0.019
$e^+e^- \rightarrow e^+e^-\gamma$	1000 k	802
$e^+e^- \rightarrow t^+t^-\gamma$	100 k	6.678

# Bibliography

- [1] E. Fermi, Attempt at a Theory of Beta-Rays, *Il Nuovo Cimento* **11** (1934) 1.
- [2] T. D. Lee, M. Rosenbluth and C. N. Yang, Interaction of Mesons with Nucleons and Light Particles, *Phys. Rev* **75** (1949) 905.
- [3] C. S. Wu *et al.*, Experimental Test of Parity Conservation in Beta Decay, *Phys. Rev.* **105** (1957) 1413.
- [4] R. P. Feynman, M. Gell-Mann, Theory of the Fermi Interaction, *Phys. Rev.* **109** (1958) 193.
- [5] T. Fazzini *et al.*, Electron Decay of the Pion, *Phys. Rev. Lett.* **1** (1958) 247.
- [6] S. Weinberg, A Model of Leptons, *Phys. Rev. Lett.* **19** (1967) 1264.
- [7] A. Salam, in: *Elementary Particle Theory*, Ed. N. Svartholm (Almqvist and Wiksell, Stockholm, 1968).
- [8] S. L. Glashow, Partial Symmetries of Weak Interactions, *Nucl. Phys.* **22** (1961) 579.
- [9] M. Gell-Mann, The Eightfold Way: A Theory of Strong Interaction Symmetry, Caltech Report CTSL-20 (1961).
- [10] M. Gell-Mann, A Schematic Model of Baryons and Mesons, *Phys. Lett.* **8** (1964) 214.
- [11] M. Breidenbach *et al.*, Observed Behaviour of Highly Inelastic Electron-Proton scattering, *Phys. Rev. Lett.* **23** (1969) 935.
- [12] D. J. Gross, F. Wilczek, Asymptotically Free Gauge Theories, *Phys. Rev.* **D8** (1973) 3633.
- [13] G. Arnison *et al.* (The UA1 Collaboration), Experimental Observation of Isolated Large Transverse Energy Electrons With Associated Missing Energy at  $\sqrt{s} = 540$  GeV, *Phys. Lett.* **B122** (1983) 103.
- [14] M. Banner *et al.* (The UA2 Collaboration), Observation of Single Isolated Electrons of High Transverse Momentum in Events with Missing Transverse Energy at the CERN  $p\bar{p}$  collider, *Phys. Lett.* **B122** (1983) 476.
- [15] J. Alitti *et al.* (The UA2 Collaboration), An Improved Determination of the Ratio of the  $W$  and  $Z$  Masses at the CERN  $p\bar{p}$  Collider, *Phys. Lett.* **B276** (1992) 354.
- [16] F. Abe *et al.* (The CDF Collaboration), A Measurement of the  $W$  Mass, *Phys. Rev. Lett.* **75** (1995) 11.

- [17] S. Abachi *et al.* (The D0 Collaboration), Measurement of the  $W$  Boson Mass, Phys. Rev. Lett. **77** (1996) 3309.
- [18] F. Boudjema and B. Mele, “Standard Model Processes” in “Physics at LEP II”, CERN report 96-01 eds G. Altarelli, T. Sjöstrand, F. Zwirner. vol. 1. 207-248 (1996).
- [19] R. Barate *et al.* (The ALEPH collaboration), Measurement of the  $W$  Mass and Width in  $e^+e^-$  collisions at 189 GeV, Eur. Phys. J. C **17** (2000) 241.
- [20] F. Halzen and A. Martin, Quarks and Leptons: An Introductory Course in Modern Particle Physics (John Wiley and Sons Inc, New York, 1984).
- [21] R. Barate *et al.* (The ALEPH collaboration), Measurement of the  $Z^0$  Resonance Parameter at LEP, Eur. Phys. J. **C14** (2000) 1.
- [22] R. Chierici, Measurement of  $W$ -Pair Production and Single- $W$  Pair Production at LEP, presented at the International Europhysics Conference on High Energy Physics, Budapest, July 12-18 (2001).
- [23] W. Beenakker and A. Denner, Standard Model Predictions for  $W$  Pair Production in Electron-Positron Collisions, Int. J. Mod. Phys. **A9** (1994) 4837.
- [24] T. Muta, R. Najima and S. Wakiazumi, Effects of the  $W$ -boson Width in  $e^+e^- \rightarrow W^+W^-$  Reactions, Mod. Phys. Lett. **A1** (1986) 203.
- [25] A. Beddall, Inclusive Production of the  $\omega(782)$  Vector Meson in Hadronic Decay of the  $Z$ , PhD thesis, Department of Physics, University of Sheffield (1995).
- [26] A. Blondel *et al.* (The LEP energy working group), Evaluation of the centre-of-mass energy above the  $W$ -pair Production Threshold, Eur. Phys. J. **C 11** (1999) 573.
- [27] C. Bowdery *et al.* (The ALEPH Collaboration), The 1995 ALEPH HANDBOOK, Vol. 1 and 2, CERN, Geneva, Switzerland, (1995 and 1997).
- [28] B. Rensch, Produktion der neutralen seltsamen Teilchen  $K_S^0$  und Lambda in hadronischen  $Z$ -Zerfällen am LEP-Speicherring, PhD thesis, Universität Heidelberg (1992).
- [29] D. Buskulic *et al.* (ALEPH Collaboration), Performance of the ALEPH Detector at LEP, Nucl. Instr. Meth. **A360** (1995) 481.
- [30] M. Skrzypek, S. Jadach, W. Placzek, and Z. Wąs, Monte Carlo program KORALW-1.02 for  $W$  pair production at LEP2/NLC energies with Yennie-Frautschi-Suura exponentiation, Comp. Phys. Commun. **94** (1996) 216.
- [31] MINAMI-TATEYA group. GRACE manual: Automatic Generation of Tree Amplitudes in Standard Models : Version 1.0 KEK report 92-19 (1993).
- [32] D. Yennie, S. Frautschi and H. Suura, The Infrared Divergence Phenomena and High-Energy Processes, Ann. Phys. **13** (1961) 379.
- [33] S. Jadach, G. Passarino and R. Pittau, Report of the working groups on Precision Calculation for LEP2 Physics, CERN 2000-009.

- [34] A. Denner, S. Dittmaier, M. Roth, and D. Wackerroth,  $O(\alpha)$  Corrections to  $e^+e^- \rightarrow W^+W^- \rightarrow 4f(+\gamma)$ : First Numerical Results from RacoonWW, Phys. Lett. **B475** (2000) 127.
- [35] S. Jadach, W. Placzek, M. Skrzypek, B. F. L. Ward, and Z. Wąs, Exact  $O(\alpha)$  Gauge Invariant YFS Exponentated Monte Carlo for (un)Stable  $W^+W^-$  Production at and Beyond LEP-2 Energies, Phys. Lett. **B417** (1998) 326; CERN-TH/1999-222, UTHEP-98-0502.
- [36] T. Sjöstrand. High-Energy Physics event generation with PYTHIA 5.7 and JETSET 7.4, Comp. Phys. Commun. **82** (1994) 74.
- [37] S. Jadach, B. F. L. Ward and Z. Wąs, The Monte Carlo program KORALZ, version 4.0, for the Lepton and Quark Production at LEP/SLC Energies, Comp. Phys. Commun. **79** (1994) 503-522.
- [38] D. Buskulic *et al.* (The ALEPH Collaboration), A Direct Measurement of the Invisible Width of the Z from Single Photon Counting, Phys. Lett. **313** (1993) 509.
- [39] R. Barate *et al.* (The ALEPH Collaboration), Studies of Quantum Chromodynamics with the ALEPH Detector, Phys. Rep. 294 (1998) 1.
- [40] G. Altarelli and G. Parisi, Asymptotic Freedom in Parton Language, Nucl. Phys. **B126** (1977) 298.
- [41] G. Marchesini *et al.*, HERWIG: A Monte Carlo Event Generator for Simulating Hadron Emission with Interfering Gluons Version 5.1, Comp. Phys. Comm. **67** (1992) 465.
- [42] L. Lönnblad, ARIADNE version 4: A Program for Simulation of QCD Cascades Implementing the Colour Dipole Model, Comp. Phys. Comm. **71** (1992) 15.
- [43] E. Barberio and Z. Wąs, PHOTOS: A Universal Monte Carlo for QED Radiative Corrections. Version 2.0, Comp. Phys. Comm. **79** (1994) 291.
- [44] GEANT, Detector and Simulation tool, CERN Program Library Long Writeup W5013, (CERN, Geneva, 1993).
- [45] "GALEPH user guide" ALEPH note 88-119 ed. F. Ranjard (1998).
- [46] R. L. Ford and W. R. Nelson, The EGS Code System - Version 3, Stanford Linear Accelerator Center, Report SLAC-210 (1978).
- [47] H. Fesefeldt, The E/H Ratio Energy Resolution of Hadron Calorimeters, PITHA 86/05, (1986) Nucl. Inst. Meth **A263**, (1988) 114.
- [48] E. Thomson, Measurement of the W Boson Mass from  $e^+e^- \rightarrow W^+W^- \rightarrow l\bar{\nu}q\bar{q}$  Events with the ALEPH Detector, PhD thesis, Department of Physics and Astronomy, University of Glasgow (1998).
- [49] W. Bartel *et al.* (The JADE collaboration), Experimental Studies on Multi-jet Production in  $e^+e^-$  Annihilation at PETRA Energies, Z. Phys. **C 33** (1986) 23.
- [50] Y.L. Dokshitzer, contribution to Workshop on Jets at LEP and HERA, Durham (1990); S. Catani *et al.*, New Clustering Algorithm for Multi-jet Cross-Sections in  $e^+e^-$  Annihilation, Phys. Lett. **B269** (1991) 432.

- [51] R. J. Cavanaugh and M. J. Corden, A Kinematic Fit to Semi-Leptonic WW Events without Jet Finding, ALEPH 97-087 PHYSIC 97-077 (1997).
- [52] V. Blobel, Formulae and Methods in Experimental data evolution, (1983) vol.3.
- [53] O. Buchmüller, Kinematische Rekonstruktion von WW-Ereignissen bei LEP2, PhD thesis, Universität Heidelberg (1999).
- [54] H. Albrecht, E. Blucher and J. Boucrot, ALPHA, ALEPH PHYSICS ANALYSIS PACKAGE, Versions > 122.
- [55] R. Cavanaugh, A Measurement of the  $W$  Boson Mass, PhD thesis, Florida State University (1999).
- [56] E. Lançon *et al.*  $W$  Mass Measurement in the semileptonic channel using a Monte Carlo Reweighting technique, ALEPH 97-073 PHYSIC 97-064 (1997).
- [57] D. Bardin *et al.*, GENTLE/4fan version 2.0: a Program for the Semi-analytic Calculation of predictions for the process  $e^+e^- \rightarrow 4f$ , DESY 96-223, hep-ph/9612409.
- [58] F. James. MINUIT, Function Minimization and Error Analysis, Reference Manual, Version 94.1 CERN Program Library Long Write-up D506. (CERN, Geneva, 1994).
- [59] E. Wannemacher, Bestimmung der Masse des  $W$ -Bosons aus dem rekonstruierten Massenspektrum, Diploma thesis (unpublished), Universität Heidelberg (1999).
- [60] O. Buchmüller *et al.*, Measurement of the  $W$ -Boson Mass in the Semileptonic Channel using a Multi-dimensional Reweighting Technique, ALEPH 99-107, PHYSICS 99-050 (1999).
- [61] C. Rittger, Bestimmung der  $W$ -Masse aus dem Leptonenergiespektrum mit dem Detektor ALEPH, Diploma thesis (unpublished), Universität Heidelberg (1999).
- [62] S. Dessagne, Détermination de la masse du boson  $W$  à LEP2 avec le détecteur ALEPH par l'étude du spectre d'énergie des leptons, PhD thesis, Université Blaise Pascal (2000).
- [63] B. Raeven, Measurement of the  $W$  mass and width of the  $W$  boson from  $e^+e^- \rightarrow W^+W^- \rightarrow (e/\mu)q\bar{q}$  events with the ALEPH detector, PhD thesis, Department of Physics and Astronomy, University of Glasgow (2000).
- [64] F. Ligabue, <http://alephwww.cern.ch/~ligabue/syst/syst.html>
- [65] Measurement of the  $W$  Mass and Width in  $e^+e^-$  Collisions at  $\sqrt{s}$  between 192 and 208 GeV, ALEPH 2001-021 (2001).
- [66] R. Assmann *et al.* (The LEP energy working group), Evaluation of the LEP Centre-of-mass Energy for Data taken in 1998, 99/01 (1999).
- [67] R. Assmann *et al.* (The LEP energy working group), Evaluation of the LEP Centre-of-mass Energy for Data taken in 1999, 00/01 (2000).
- [68] R. Assmann *et al.* (The LEP Energy Working group), Evaluation of the LEP Centre-of-mass Energy for Data taken in 2000, 01/01 (2001).

- [69] A. P. Chaoovsky, V. A. Khoze, Screened Coulomb Ansatz for the Nonfactorizable Radiative Corrections to the Off-Shell  $W^+W^-$  Production, *Eur. Phys. J.* **C9** (1999) 449.
- [70] H. Ruiz, Measurement of the mass and width of the W boson at LEP II, presented at the International Europhysics Conference on High Energy Physics, Budapest, July 12-18 (2001).
- [71] Delphi Collaboration, Measurement of the mass and width of the W boson in  $e^+e^-$  collision at LEP, DELPHI 2001-103 CONF 531 (2001).
- [72] L3 Collaboration, Preliminary Results on the Measurement of Mass and Width of the W boson at LEP, L3 Note 2637 (February 2001).
- [73] Opal Collaboration, Measurement of the Mass of the W Boson in  $e^+e^-$  Annihilations at 192-202 GeV, OPAL Physics Note PN422 (updated July 2000).
- [74] R. Barate *et al.* (The ALEPH collaboration), Observation of an excess in the search for the Standard Model Higgs boson at ALEPH, *Phys. Lett.* **B 495** (2000) 1.
- [75] S. Mele, Combined Fit to Electroweak Data and Constraints on Standard Model, presented at the International Europhysics Conference on High Energy Physics, Budapest, July 12-18 (2001).
- [76] [http://www-cdf.fnal.gov/physics/ewk/wmass\\_new.html](http://www-cdf.fnal.gov/physics/ewk/wmass_new.html)
- [77] A. Czarnecki and J. Kühn, Nonfactorizable QCD and Electroweak Corrections to the Hadronic Z Boson Decay Rate, *Phys. Rev. Lett.* **77** (1996) 3955.
- [78] R. Harlander, T. Seidensticker and M. Steinhauser, Complete Corrections of  $\mathcal{O}(\alpha\alpha_s)$  to the decay of the Z Boson into Bottom Quark, *Phys. Lett.* **B426** (1998) 125.

# Acknowledgement

It is now time to thank all the people who have supported me along these 3 and half years in Heidelberg or make the time here very pleasant.

Prof. E. E. Kluge took me under his supervision and simplified my life here a lot.

Prof. O. Nachtmann kindly took the role of the second corrector.

Prof. K. Tittel accepted me in the former IHEP institute.

Dr. C. Geweniger kindly answered all my question.

Prof. V. Hepp and Dr. H. Stenzel were always available to discuss physic issues.

Dr O. Buchmüller “you are a doktorand, you should know that”, you are missing, guy!

Dr S. Dhamotharan ”what you are doing is anyway trash!!!”

T. Golling? Well, maybe see you in Chicago.

Dr. K. Mahboubi “let us stop working? No, tomorrow morning” and for numerous discussion about a chip: the thesis is delivered before the chip!

Dr. T. Berndt “why don’t you install the new x+1’s software?” Useless

Dr. J. Stiewe “Errare humanum est.” Or how to interest poor young scientists to basically everything.

And finally, Rick after 8 o’clock “What??? Zidane plays in Real” ... and Real will win the champions leagues and France the next world cup....

or Dr. R. Cavanaugh before “I Did not make any progress, just getting crazy! no you did” thanks Rick for all your support, even 10000 km away.

Also all the members of the so-called “Kaffee Runde”, not for the coffee, but trying to explain me: Die Milch oder der Zucker? are the articles correct?

At CERN, I have been in contact with many people. The best working group that I have seen: “The ALEPH on-line” even if BBQ were too rare... And of course the W group:

Franco “sorry to disturb you with that”

Andrea Venturi “What are your plans??”

Kay (the first German guy who invited me in a house in Germany) “Essen? Cafe? Klar”

Jason “How can you survive without meat?”

Barbara R. “let’s have some fun...”

Christian “A la vie Marseillaise ....”

Patrice pour de nombreuses anecdotes....

Ann and Anne for a lot of tips...

Stephane and Renaud for a lot of e-mail exchange.

To finish this huge list, I would like to thank my parents and my girlfriend Anne for supporting me the last 3 years! It was not so easy.